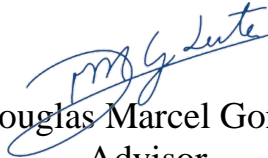


Thesis presented to the Instituto Tecnológico de Aeronáutica, in partial fulfillment of the requirements for the degree of Doctor of Science in the Program of Aeronautical and Mechanical Engineering, field of Materials, Manufacturing and Automation.

Isabela Machado Horta

**DEPOSITION AND CHARACTERIZATION OF THIN FILMS
AND HETEROSTRUCTURES OF GaN AND $\text{Al}_x\text{Ga}_{1-x}\text{N}$ USING
REACTIVE MAGNETRON SPUTTERING DEPOSITION**

Thesis approved in its final version the signatories below:



Prof. Dr. Douglas Marcel Gonçalves Leite
Advisor



Prof. Dr. André Luis de Jesus Pereira
Co-advisor

Prof. Dr. Emília Villani
Dean of Graduate Studies

Campo Montenegro
São José dos Campos, SP – Brazil
2023

Cataloging-in-Publication Data
Documentation and Information Division

Horta, Isabela Machado
Deposition and Characterization of Thin Films and Heterostructures of GaN and $Al_xGa_{1-x}N$ Using Reactive Magnetron Sputtering Deposition/ Isabela Machado Horta.
São José dos Campos, 2023.
157f.

Thesis of Doctor of Science – Course of Aeronautical and Mechanical Engineering. Area of Materials, Manufacturing and Automation – Instituto Tecnológico de Aeronáutica, 2023. Advisor: Prof. Dr. Douglas Marcel Gonçalves Leite.

1. Thin Film. 2. Reactive Magnetron Sputtering. 3. Semicondutor. I. Instituto Tecnológico de Aeronáutica. II. Title

BIBLIOGRAPHIC REFERENCE

HORTA, Isabela Machado. **Deposition and Characterization of Thin Films and Heterostructures of GaN and $Al_xGa_{1-x}N$ Using Reactive Magnetron Sputtering Deposition.** 2023. 157f. Thesis of Doctor of Science in Aeronautical and Mechanical Engineering– Instituto Tecnológico de Aeronáutica, São José dos Campos.

CESSION OF RIGHTS

AUTOR NAME: Isabela Machado Horta

PUBLICATION TITLE: Deposition and Characterization of Thin Films and Heterostructures of GaN and $Al_xGa_{1-x}N$ Using Reactive Magnetron Sputtering Deposition

PUBLICATION KIND/YEAR: Thesis/2023

It is granted to Instituto Tecnológico de Aeronáutica permission to reproduce copies of this thesis to only loan or sell copies for academic and scientific purposes. The author reserves other publication rights and no part of this thesis can be reproduced without his authorization.

Isabela Machado Horta
Praça Marechal Eduardo Gomes, 50
São José dos Campos – SP, Brazil

**DEPOSITION AND CHARACTERIZATION OF THIN FILMS
AND HETEROSTRUCTURES OF GaN AND $\text{Al}_x\text{Ga}_{1-x}\text{N}$ USING
REACTIVE MAGNETRON SPUTTERING DEPOSITION**

Isabela Machado Horta

Thesis Committee Composition:

Prof. Dr. Gilberto Petraconi Filho	Chairperson	- ITA
Prof. Dr. Douglas Marcel Gonçalves Leite	Advisor	- ITA
Prof. Dr. André Luis de Jesus Pereira	Co-advisor	- ITA
Dr. Thaís Larissa do Amaral Montanheiro		- ITA
Prof. Dr. Ziani de Souza Schiaber		- UFGD
Prof. Dr. Renata Antoun Simão		- UFRJ

ITA

To my family.

Acknowledgments

Em primeiro lugar, à minha família. Minha mãe, Célia, pelo carinho e prestígio que me levaram a chegar aqui. Seus ensinamentos me levaram a sempre buscar mais aprendizado e educação, tanto acadêmica quanto emocional. À minha irmã, Amanda, que fez por mim mais do que ela própria imagina ou entende e mais do que eu sou capaz de verbalizar. Também ao meu pai, Luiz Carlos que esteve sempre presente na minha jornada, fazendo parte de quem eu sou e vivendo em mim. Aos meus sobrinhos, Teodoro e Olga, que tão cedo me trouxeram alegrias sem fim.

Agradeço ao André pelo amor e pelo companheirismo todos os dias. Agradeço também aos meus amigos que estão todos dentro do meu coração. Aos amigos de fora do laboratório, Matheus Santos, Matheus Zeni, Marcos, Gabriela Ramalho, Maria Carolina, Hannah, Raissa, e Gabriela Romeiro. Aos amigos que compartilham e acompanharam minha jornada no LPP, Bárbara, Raissa, Vanessa, Letícia, Karla e Alan.

Agradeço imensamente ao meu orientador, professor Douglas, e meu coorientador, professor André, e a todos os alunos, professores e funcionários do Laboratório de Plasmas e Processos do ITA.

Por fim, agradeço ao CNPq e à CAPES pelo suporte financeiro a este projeto.

*“I am not what happened to me, I am what I
choose to become.”*

(C. G. Jung)

Abstract

This work reports on the deposition and characterization of different Al-content $\text{Al}_x\text{Ga}_{1-x}\text{N}$ thin films and subsequent $\text{GaN}/\text{Al}_x\text{Ga}_{1-x}\text{N}$ heterostructures using reactive magnetron sputtering deposition. Since achieving high-quality sputtered GaN still relies on the use of expensive substrates, high temperatures and intricate buffer layers, the use of AlGaN buffer has shown to enhance the quality of these films in a continuous process. Therefore, the main objective is to study the effect of the composition on the quality of the $\text{Al}_x\text{Ga}_{1-x}\text{N}$ films to determine the most suitable composition for the production of heterostructures using AlGaN as a buffer layer for GaN, in terms of *c*-axis orientation and crystalline structure, to make this material suitable for application in SAW devices. The $\text{Al}_x\text{Ga}_{1-x}\text{N}$ films were produced using different applied powers to the Al and Ga targets to vary the composition, with the Al content ranging from $0 \leq x \leq 0.47$. Additionally, different substrates were used for the films, including glass and different Si orientations. The other deposition parameters were fixed for all processes, such as pressure (5 mTorr), temperature (550 °C), argon and nitrogen flow (7 and 14 sccm, respectively), and substrate position (90 mm above the Ga target). From the $\text{Al}_x\text{Ga}_{1-x}\text{N}$ films, a set of different compositions and $\text{Al}_x\text{Ga}_{1-x}\text{N}$ layer numbers were selected to produce the heterostructures on glass and Si(100) substrates. This approach allowed for the creation of highly *c*-oriented GaN films with minimized strains, defects, and surface roughness. The samples were characterized using energy dispersive spectroscopy, optical profilometry, X-ray diffraction, UV-Vis spectrophotometry, Raman spectroscopy, and scanning electron microscopy. The results showed a strong correlation between the properties of the $\text{Al}_x\text{Ga}_{1-x}\text{N}$ films and the composition, as well as an influence of the thickness of the samples. All samples displayed a wurtzite structure with a *c*-axis preferred orientation, which is desirable as a buffer layer, and this orientation increased with higher Al content. The quality of the films, in general, was evaluated using a combination of results from the different techniques, demonstrating that the Al content plays different roles in terms of strains, crystalline quality, bandgap, refractive index, and Raman phonon modes. For the heterostructures, the presence of an Al-rich buffer layer led to a more strongly *c*-oriented GaN film, with no clear relation to the number or thickness of the buffer layer. Therefore, a high-Al content thin buffer layer successfully increased the quality of the GaN film. However, the use of multiple buffer layers with a compositional gradient further improved the surface of the GaN films without a clear improvement in the structural properties, but it also significantly increased the deposition time and the complexity of the process.

Figures

Figure 1: Number of publications on the topics “GaN” and “GaN+AlGaN” over the past 10 years (a) worldwide and (b) in Brazil.	21
Figure 2: (a) Crystalline structure of wurtzite GaN and (b) its unit cell. Adapted from (UDABE; BARAIA-ETXABURU; DIEZ, 2023).	24
Figure 3: Representation of X-Ray diffraction with the conditions for Bragg diffraction. Adapted from (MORAM; VICKERS, 2009).....	27
Figure 4: Powder diffraction patterns for (a) GaN and (b) AlN.....	28
Figure 5: Relationship between film thickness and FWHM for (a) sputtered AlN (DUQUENNE et al., 2008) and (b) MBE-grown GaN (SEON et al., 2000).	30
Figure 6: Schematic of the optical phonon modes observed in wurtzite structures.	32
Figure 7: Phonon frequencies in wurtzite $Al_xGa_{1-x}N$ alloys as a function of the Al content (DAVYDOV et al., 2002).....	34
Figure 8: Bandgap dependence on the lattice constant for III-nitrides (SCHUBERT, 2006)..	37
Figure 9: Surface morphology of MOCVD grown GaN films onto Si(111) with (a) no buffer layer, (b) 16 nm GaN buffer, (c) 33 nm GaN buffer, (d) 50 nm GaN buffer, (e) 29 nm AlN buffer, and (f) 44 nm AlN buffer (ARIFIN et al., 2022).	40
Figure 10: Basic system of a reactive magnetron sputtering deposition (NGARUIYA, 2004).	41
Figure 11: Representation of the deposition chamber, where <i>a</i> is the substrate holder with rotating and heating system, <i>b</i> is the gallium magnetron, <i>c</i> and <i>d</i> are the In and Al magnetrons, respectively, <i>e</i> is the nitrogen gas inlet pipe and <i>f</i> is the vacuum flange protection.	50
Figure 12: Heterostructures using a) one buffer layer with low Al content, b) one buffer layer rich in Al, c) two buffer layers and d) three buffer layers.	54
Figure 13: Correlation between the Al content on the $Al_xGa_{1-x}N/Si$ samples and the relative power applied to the Al target, highlighting the effects of fixed (a) Al-target DC power and (b) Ga-target RF power.	60
Figure 14: a) Different <i>x</i> values of the $Al_xGa_{1-x}N/glass$ samples calculated using XRD and EDS analyses and b) correlation of the % of Al obtained using EDS and XRD.	61
Figure 15: Effects of the power applied to the Al target and the Ga target on the deposition rate of the $Al_xGa_{1-x}N/Si$ samples.	62

- Figure 16: XRD results of the $\text{Al}_x\text{Ga}_{1-x}\text{N}$ samples on glass substrates. Dashed lines indicate the expected position for the $\text{Al}_x\text{Ga}_{1-x}\text{N}$ peaks, that goes from GaN ($x = 0$), in the lower angles, to AlN ($x = 1$), in the higher angles. 64
- Figure 17: Diffractograms of the $\text{Al}_x\text{Ga}_{1-x}\text{N}$ samples on glass substrate: (a) using 30 W on the Ga target with (b) a zoom-in of the (0002) region, (c) using 60 W on the Ga target with (d) a zoom-in of the (0002) region, and (e) using 90 W on the Ga target with (f) a zoom-in of the (0002) region. Dashed lines indicate the expected position for the AlGa_N diffraction peaks. 66
- Figure 18: Lattice parameters (a) a and (b) c of the $\text{Al}_x\text{Ga}_{1-x}\text{N}$ samples on glass substrates. The expected values for the unstrained GaN and AlN lattice parameters are indicated, as well as their linear relation. The error bar is not visible because it is smaller than the dots in the graph. 68
- Figure 19: (a) Peak position and (b) FWHM related to the (0002) plane of the $\text{Al}_x\text{Ga}_{1-x}\text{N}$ samples on glass substrate. The expected (0002) peak position for unstrained GaN and AlN are indicated, as well as their linear relation. The error bar is not visible because it is smaller than the dots in the graph. 70
- Figure 20: (0002) FWHM related to the thickness of the $\text{Al}_x\text{Ga}_{1-x}\text{N}$ films for glass substrates. The x values of the composition of the films are indicated as the label of each point. 71
- Figure 21: XRD results of the $\text{Al}_x\text{Ga}_{1-x}\text{N}$ samples on Si (100) A substrates. Dashed lines indicate the expected position for the $\text{Al}_x\text{Ga}_{1-x}\text{N}$ peaks, that goes from GaN ($x = 0$), in the lower angles, to AlN ($x = 1$), in the higher angles. 73
- Figure 22: XRD results of the $\text{Al}_x\text{Ga}_{1-x}\text{N}$ samples on Si (100) A substrates. Dashed lines indicate the expected position for the $\text{Al}_x\text{Ga}_{1-x}\text{N}$ peaks, that goes from GaN ($x = 0$), in the lower angles, to AlN ($x = 1$), in the higher angles. 74
- Figure 23: Diffractograms of the $\text{Al}_x\text{Ga}_{1-x}\text{N}$ samples on Si (100) A substrate: (a) using 30 W on the Ga target with (b) a zoom-in of the (0002) region, (c) using 60 W on the Ga target with (d) a zoom-in of the (0002) region, and (e) using 90 W on the Ga target with (f) a zoom-in of the (0002) region. Dashed lines indicate the expected position for the AlGa_N diffraction peaks. 75
- Figure 24: Diffractograms of the $\text{Al}_x\text{Ga}_{1-x}\text{N}$ samples on Si (100) A substrate: (a) using 30 W on the Ga target with (b) a zoom-in of the (0002) region, (c) using 60 W on the Ga target with (d) a zoom-in of the (0002) region, and (e) using 90 W on the Ga target with (f) a

- zoom-in of the (0002) region. Dashed lines indicate the expected position for the AlGa_xN diffraction peaks. 76
- Figure 25: Lattice parameters (a) a and (b) c of the Al _{x} Ga_{1- x} N samples on Si (100) A substrates. The expected values for the unstrained GaN and AlN lattice parameters are indicated, as well as their linear relation. The error bar is not visible because it is smaller than the dots in the graph..... 77
- Figure 26: Lattice parameters (a) a and (b) c of Al _{x} Ga_{1- x} N samples on Si (100) B substrates. The expected values for the unstrained GaN and AlN lattice parameters are indicated as well as their linear relation. The error bar is not visible because it is smaller than the dots in the graph..... 78
- Figure 27: (a) Peak position and (b) FWHM related to the (0002) plane of the Al _{x} Ga_{1- x} N samples on Si (100) A substrate. The expected (0002) peak positions for unstrained GaN and AlN are indicated, as well as their linear relation. The error bar is not visible because it is smaller than the dots in the graph. 79
- Figure 28: (a) Peak position and (b) FWHM related to the (0002) plane of the Al _{x} Ga_{1- x} N samples on Si (100) B substrate. The expected (0002) peak positions for unstrained GaN and AlN are indicated, as well as their linear relation. The error bar is not visible because it is smaller than the dots in the graph. 80
- Figure 29: (0002) FWHM related to the thickness of the Al _{x} Ga_{1- x} N films for the two Si(100) substrates. The x values of the composition of the films are indicated as the label of each point. 81
- Figure 30: XRD results of the Al _{x} Ga_{1- x} N samples on Si (110) substrates. Dashed lines indicate the expected position for the Al _{x} Ga_{1- x} N peaks, that goes from GaN ($x = 0$), in the lower angles, to AlN ($x = 1$), in the higher angles. 83
- Figure 31: Diffractograms of the Al _{x} Ga_{1- x} N samples on Si (110) substrate: (a) using 30 W on the Ga target with (b) a zoom-in of the (0002) region, (c) using 60 W on the Ga target with (d) a zoom-in of the (0002) region, and (e) using 90 W on the Ga target with (f) a zoom-in of the (0002) region. Dashed lines indicate the expected position for the AlGa _{x} N diffraction peaks. 85
- Figure 32: Lattice parameters (a) a and (b) c of the Al _{x} Ga_{1- x} N samples on Si (110) substrates. The expected values for the unstrained GaN and AlN lattice parameters are indicated, as well as their linear relation. The error bar is not visible because it is smaller than the dots in the graph..... 86

- Figure 33: (a) Peak position and (b) FWHM related to the (0002) plane of the $\text{Al}_x\text{Ga}_{1-x}\text{N}$ samples on Si (110) substrate. The expected (0002) peak positions for unstrained GaN and AlN are indicated, as well as their linear relation. The error bar is not visible because it is smaller than the dots in the graph. 88
- Figure 34: (0002) FWHM related to the thickness of the $\text{Al}_x\text{Ga}_{1-x}\text{N}$ films for the Si(110) substrate. The x values of the composition of the films are indicated as the label of each point. 89
- Figure 35: XRD results of the $\text{Al}_x\text{Ga}_{1-x}\text{N}$ samples on Si (111) substrates. Dashed lines indicate the expected position for the $\text{Al}_x\text{Ga}_{1-x}\text{N}$ peaks, that goes from GaN ($x = 0$), in the lower angles, to AlN ($x = 1$), in the higher angles. 91
- Figure 36: Diffractograms of the $\text{Al}_x\text{Ga}_{1-x}\text{N}$ samples on Si (111) substrate: (a) using 30 W on the Ga target with (b) a zoom-in of the (0002) region, (c) using 60 W on the Ga target with (d) a zoom-in of the (0002) region, and (e) using 90 W on the Ga target with (f) a zoom-in of the (0002) region. Dashed lines indicate the expected position for the AlGa_N diffraction peaks. 92
- Figure 37: Lattice parameters (a) a and (b) c for the $\text{Al}_x\text{Ga}_{1-x}\text{N}$ samples on Si (111) substrates. The expected values for the unstrained GaN and AlN lattice parameters are indicated, as well as their linear relation. The error bar is not visible because it is smaller than the dots in the graph. 93
- Figure 38: (a) Peak position and (b) FWHM related to the (0002) plane for the $\text{Al}_x\text{Ga}_{1-x}\text{N}$ samples on Si (111) substrate. The expected (0002) peak positions for unstrained GaN and AlN are indicated, as well as their linear relation. The error bar is not visible because it is smaller than the dots in the graph. 95
- Figure 39: (0002) FWHM related to the thickness of the $\text{Al}_x\text{Ga}_{1-x}\text{N}$ films for the Si(111) substrate. The x values of the composition of the films are indicated as the label of each point. 96
- Figure 40: Relative intensity between the (0002) and (1011) peaks for the different Si substrate samples. The error bar is not visible because it is smaller than the dots in the graph. . 98
- Figure 41: Relative intensity between the (0002) and (1011) peaks for the glass substrate samples. The error bar is not visible because it is smaller than the dots in the graph. . 99
- Figure 42: Degree of c -orientation (relative intensity of the (0002) peak) in relation to the thickness for (a) the Si substrates samples and (b) the glass substrate samples. The x values of the composition of the films are indicated as the label of each point. 100

Figure 43: UV-Vis transmission spectra of the $\text{Al}_x\text{Ga}_{1-x}\text{N}/\text{glass}$ samples with zoom-in of the absorption edge. *S_50_60, produced using 60 W on the Ga target. **S_100_90, produced using 90 W on the Ga target	102
Figure 44: UV-Vis transmission spectra of the $\text{Al}_x\text{Ga}_{1-x}\text{N}$ samples deposited using (a) 60 W, (b) 90 W, and (c) 30 W, on the RF supply for the Ga target.	103
Figure 45: Static refractive index as a function of Al content highlighting the different RF power used. The error bar is not visible because it is smaller than the dots in the graph.....	105
Figure 46: (a) Bandgap E_g of the $\text{Al}_x\text{Ga}_{1-x}\text{N}$ samples and its relation to the Al content highlighting the different RF power used and (b) the comparative with reference data (ANGERER et al., 1997; JIANG et al., 2001; KOIDE et al., 1987; LI et al., 2021; TAKEUCHI et al., 1997; TISCH et al., 2001; YUN et al., 2002). The error bar is not visible because it is smaller than the dots in the graph.....	106
Figure 47: Raman spectra of the $\text{Al}_x\text{Ga}_{1-x}\text{N}/\text{glass}$ samples and the glass substrate. Dashed lines indicate the expected positions for the E_2^{H} and $A_1(\text{LO})$ phonon modes for GaN.	107
Figure 48: Magnification of Raman spectra of pure GaN, AlGaN thin films, and glass substrate detailing the E_2 (high) and A_1 (LO) phonon modes for samples deposited using (a) 60 W, (b) 90 W, and (c) 30 W on the Ga-target RF-power supply.	108
Figure 49: E_2^{H} peak Raman shift of the $\text{Al}_x\text{Ga}_{1-x}\text{N}$ samples on glass substrates for the different RF power used on the Ga-target. The dashed pink line shows the expected position for the GaN-like E_2^{H} phonon mode of the AlGaN alloy. The error bar is not visible because it is smaller than the dots in the graph.	109
Figure 50: $A_1(\text{LO})$ peak Raman shift of the $\text{Al}_x\text{Ga}_{1-x}\text{N}$ samples on glass substrates for the different RF power used on the Ga-target. The dashed pink dashed line shows the expected position for the $A_1(\text{LO})$ phonon mode of the AlGaN alloy. The error bar is not visible because it is smaller than the dots in the graph.....	110
Figure 51: (a) X-Ray diffractogram of the GaN/Si(100) film without buffer layer and (b) zoom-in on the (0002) peak region.	111
Figure 52: (a) Diffractogram of different buffer layer thicknesses of three GaN/ $\text{Al}_{0.07}\text{Ga}_{0.93}\text{N}$ heterostructures and (b) zoom in on the region with the (0002) peak.	112
Figure 53: (a) Diffractogram of different buffer layer thicknesses of three GaN/ $\text{Al}_{0.37}\text{Ga}_{0.63}\text{N}$ heterostructures and (b) zoom in on the region with the (0002) peak.	113

Figure 54: (a) Diffractogram of different 250 nm buffer layer composition of two GaN/Al _x Ga _{1-x} N heterostructures and (b) zoom in on the region with the (0002) peak.	115
Figure 55: (a) Diffractogram of different buffer layer number of three heterostructures and (b) zoom in on the region with the (0002) peak.	116
Figure 56: UV-Vis transmission spectra of (a) all the GaN/Al _x Ga _{1-x} N samples, (b) the GaN/Al _{0.07} Ga _{0.93} N samples, (c) the GaN/Al _{0.37} Ga _{0.67} N samples, and (d) the multiple buffer samples.	118
Figure 57: Raman spectra of the GaN/Al _{0.07} Ga _{0.93} N samples.	120
Figure 58: Raman spectra of the GaN/Al _{0.37} Ga _{0.63} N samples.	121
Figure 59: Raman spectra of the GaN/Al _x Ga _{1-x} N samples with multiple AlGa _N layers.	122
Figure 60: Cross-sectional and surface FEG-SEM images of the GaN sample.	123
Figure 61: Cross-sectional and surface FEG-SEM images of the GaN/Al _{0.07} Ga _{0.93} N samples with an Al _{0.07} Ga _{0.93} N layer thickness of approximately: (a) and (b) 1 μm, (c) and (d) 800 nm, and (e) and (f) 250 nm.	124
Figure 62: Cross-sectional and surface FEG-SEM images of the GaN/Al _{0.37} Ga _{0.63} N samples with an Al _{0.37} Ga _{0.63} N layer thickness of approximately: (a) and (b) 250 nm, and (c) and (d) 166 nm.	125
Figure 63: : Cross-sectional and surface FEG-SEM images of the a) GaN/Al _{0.24} Ga _{0.76} N/Al _{0.37} Ga _{0.63} N and b) GaN/Al _{0.07} Ga _{0.63} N/Al _{0.24} Ga _{0.76} N/Al _{0.37} Ga _{0.63} N heterostructures.	127
Figure 64: Surface FEG-SEM images of (a) GaN without buffer layer, (b) GaN/Al _{0.07} Ga _{0.93} N heterostructure, (c) GaN/Al _{0.37} Ga _{0.63} N heterostructure, and (d) GaN/Al _{0.07} Ga _{0.63} N/Al _{0.24} Ga _{0.76} N/Al _{0.37} Ga _{0.63} N heterostructure.	128
Figure 65: (a) X-Ray diffractogram of the GaN/Si(100) film without buffer layer and (b) zoom-in on the (0002) peak region.	148
Figure 66: (a) Diffractogram of different buffer layer thicknesses of three GaN/Al _{0.07} Ga _{0.93} N heterostructures and (b) zoom in on the region with the (0002) peak.	148
Figure 67: (a) Diffractogram of different buffer layer thicknesses of three GaN/Al _{0.37} Ga _{0.63} N heterostructures and (b) zoom in on the region with the (0002) peak.	149
Figure 68: (a) Diffractogram of different buffer layer number of three heterostructures and (b) zoom in on the region with the (0002) peak.	149

Figure 69: Transmittance spectrum of the GaN/Al _{0.07} Ga _{0.93} N heterostructure with a 250 nm AlGa _N buffer layer thickness (sample H_A_37).	150
Figure 70: Transmittance spectrum of the GaN/Al _{0.07} Ga _{0.93} N heterostructure with an 800 nm AlGa _N buffer layer thickness (sample H_A_120).	151
Figure 71: Transmittance spectrum of the GaN/Al _{0.07} Ga _{0.93} N heterostructure with a 1 μm AlGa _N buffer layer thickness (sample H_A_150).	151
Figure 72: Transmittance spectrum of the GaN/Al _{0.37} Ga _{0.63} N heterostructure with a 166 nm AlGa _N buffer layer thickness (sample H_B_120).....	152
Figure 73: Transmittance spectrum of the GaN/Al _{0.37} Ga _{0.63} N heterostructure with a 250 nm AlGa _N buffer layer thickness (sample H_B_180).....	152
Figure 74: Transmittance spectrum of the GaN/Al _{0.24} Ga _{0.76} N/Al _{0.37} Ga _{0.63} N heterostructure (sample H_C_120).....	153
Figure 75: Transmittance spectrum of the GaN/Al _{0.07} Ga _{0.93} N/Al _{0.24} Ga _{0.76} N/Al _{0.37} Ga _{0.63} N heterostructure (sample H_D_120).....	153
Figure 76: Surface of the GaN/Al _{0.07} Ga _{0.93} N heterostructure with a 1 μm AlGa _N buffer layer thickness (sample H_A_150).err	154
Figure 77: Surface of the GaN/Al _{0.37} Ga _{0.63} N heterostructure with a 166 nm AlGa _N buffer layer thickness (sample H_B_120).....	155
Figure 78: Surface of the GaN/Al _{0.07} Ga _{0.93} N heterostructure with an 800 nm AlGa _N buffer layer thickness (sample H_A_120).....	156
Figure 79: Surface of the GaN/Al _{0.24} Ga _{0.76} N/Al _{0.37} Ga _{0.63} N heterostructure with a total of 280 nm AlGa _N buffer layer thickness (sample H_C_120).	157

Tables

Table 1: Typical phonon Raman frequencies for wurtzite GaN and AlN films at room temperature (HARIMA, 2002).	33
Table 2: Deposition parameters for the initial exploratory study samples.	51
Table 3: Fixed deposition parameters used for all $\text{Al}_x\text{Ga}_{1-x}\text{N}$ samples.	52
Table 4: Identification of the $\text{Al}_x\text{Ga}_{1-x}\text{N}$ samples and the respective Ga and Al power used during deposition.	53
Table 5: Al content for the initial $\text{Al}_x\text{Ga}_{1-x}\text{N}$ samples obtained using EDS analyses.	58
Table 6: Al content in $\text{Al}_x\text{Ga}_{1-x}\text{N}$ samples with Si and glass substrates measured using EDS.	59
Table 7: Thickness measured using profilometry and UV-Vis spectroscopy and the respective deposition rates for the samples produced with different Ga and Al target power. Samples are ordered as they were produced.	63
Table 8: Crystallite size of the $\text{Al}_x\text{Ga}_{1-x}\text{N}$ /glass samples.	69
Table 9: In-plane and out-of-plane strains of the $\text{Al}_x\text{Ga}_{1-x}\text{N}$ /glass samples.	72
Table 10: Crystallite size of the $\text{Al}_x\text{Ga}_{1-x}\text{N}$ /Si (100) samples	79
Table 11: In-plane and out-of-plane strains of the $\text{Al}_x\text{Ga}_{1-x}\text{N}$ /Si (100) samples	82
Table 12: Crystallite size of the $\text{Al}_x\text{Ga}_{1-x}\text{N}$ /Si (110) samples.	87
Table 13: In-plane and out-of-plane strains of the $\text{Al}_x\text{Ga}_{1-x}\text{N}$ /Si (110) samples.	90
Table 14: Crystallite size of the $\text{Al}_x\text{Ga}_{1-x}\text{N}$ /Si (111) samples.	94
Table 15: In-plane and out-of-plane strains of the $\text{Al}_x\text{Ga}_{1-x}\text{N}$ /Si (111) samples.	97
Table 16: Calculations from the UV-Vis data for the $\text{Al}_x\text{Ga}_{1-x}\text{N}$ samples.	104
Table 17: Fitting results of the (0002) peak position and FWHM of the GaN/ $\text{Al}_{0.07}\text{Ga}_{0.93}\text{N}$ heterostructures.	112
Table 18: Fitting results of the (0002) peak position and FWHM of the GaN/ $\text{Al}_{0.37}\text{Ga}_{0.63}\text{N}$ heterostructures.	114
Table 19: Fitting results of the (0002) peak position and FWHM of the GaN/ $\text{Al}_x\text{Ga}_{1-x}\text{N}$ heterostructures with 250 nm buffer layer.	115
Table 20: Fitting results of the GaN (0002) peak position and FWHM of the heterostructures with different number of buffer layers.	117

List of Symbols and Abbreviations

AFM	Atomic force microscopy
ALD	Atomic layer deposition
CMOS	Complementary metal-oxide semiconductor
CVD	Chemical vapor deposition
D	Crystallite size
$d_{(hkl)}$	Interplanar spacing
DC	Direct current
EDS	Energy dispersive spectroscopy
FEG	Field emission gun
FTIR	Fourier transform infrared spectroscopy
FWHM	Full width at half maximum
HIPIMS	High power impulse magnetron sputtering
K	Shape factor
LED	Light-emitting diode
MBE	Molecular beam epitaxy
m_e	Electron mass
MEMS	Microelectromechanical systems
MOCVD	Metalorganic chemical vapor deposition
MOVPE	Metalorganic vapor phase epitaxy
N	Volumetric density of charges
n	Static refractive index
PLD	Pulsed laser deposition
PVD	Physical vapor deposition
q_e	Electron charge
RF	Radiofrequency
RMS	Root-mean-square
SAW	Surface acoustic wave
SEM	Scanning electron microscopy
TEM	Transmission electron microscopy

UV	Ultraviolet
XPS	X-ray photoelectron spectroscopy
XRD	X-Ray diffractometry
β	FWHM
ε	Dielectric constant
ε_0	Permittivity of vacuum
ε_{xx}	In-plane strain
ε_{zz}	Out-of-plane strain
λ	Wavelength
ω	Frequency
ω_0	Resonant frequency of an electron

Summary

1	INTRODUCTION	20
1.1	Problem definition and motivation	20
1.2	Research objectives.....	23
2	LITERATURE REVIEW	24
2.1	AlGaN and GaN thin films and heterostructures.....	24
	2.1.1 X-Ray diffraction.....	27
	2.1.2 Raman spectroscopy	30
	2.1.3 Optical properties	35
	2.1.4 Surface morphology	38
2.2	Reactive magnetron sputtering	40
	2.2.1 III nitrides studies	45
3	EXPERIMENTAL PROCEDURE	49
3.1	Sputtering system	49
3.2	Initial exploratory study	50
3.3	AlGaN deposition.....	51
3.4	Heterostructures deposition.....	53
3.5	Profilometry	55
3.6	Energy dispersive spectroscopy.....	55
3.7	X-Ray diffraction crystallography	56
3.8	UV-Vis spectrophotometry	56
3.9	Raman spectroscopy.....	56
3.10	Scanning electron microscopy	57
4	RESULTS AND DISCUSSION.....	58
4.1	Initial exploratory study	58
4.2	AlGaN films.....	58
	4.2.1 AlGaN composition and thickness	58
	4.2.2 X-Ray diffraction.....	64
	4.2.2.1 Glass substrate.....	64
	4.2.2.2 Si (100) substrates	73

4.2.2.3	Si (110) substrates	83
4.2.2.4	Si (111) substrates	90
4.2.2.5	Al _x Ga _{1-x} N samples summarization.....	97
4.2.3	UV-Vis analyses	101
4.2.4	Raman spectroscopy	106
4.3	GaN/AlGaN heterostructures	110
4.3.1	X-Ray diffraction.....	110
4.3.1.1	Buffer layer thickness	111
4.3.1.2	Buffer layer composition	114
4.3.1.3	Buffer layer number and compositional gradient	116
4.3.2	UV-Vis analyses	117
4.3.3	Raman spectroscopy	119
4.3.4	Scanning electron microscopy	122
5	CONCLUSIONS.....	129
6	PUBLISHED WORKS.....	132
7	RECOMMENDATIONS	133
8	REFERENCES	134
APPENDIX A – XRD OF THE GAN/ALGAN HETEROSTRUCTURES ON GLASS SUBSTRATES		148
APPENDIX B – UV-VIS TRANSMITTANCE SPECTRA OF THE GAN/ALGAN HETEROSTRUCTURES		150
APPENDIX C – FEG-SEM IMAGES SHOWCASING THE SURFACE OF THE GAN/ALGAN HETEROSTRUCTURES.....		154

1 Introduction

1.1 Problem definition and motivation

Gallium nitride (GaN) and aluminum nitride (AlN) are two wide-bandgap semiconductors that exhibit a range of unique physical and electronic properties, and are highly attractive materials for applications in transistors, light-emitting diodes (LEDs), and other optoelectronic devices due to their exceptional optical, electronic, and structural properties. These properties include their large and adjustable bandgap (ranging from 3.4 eV for GaN to 6.2 eV for AlN) and piezoelectric characteristics (LESZCZYNSKI et al., 1996; RODRÍGUEZ-MADRID et al., 2012; TIGLI; ZAGHLOUL, 2010).

GaN is known for its high electron mobility, which allows for the development of high-power devices that operate at high frequencies. Its wide bandgap and high thermal conductivity make it an ideal material for high-temperature applications. Additionally, GaN is resistant to radiation damage, making it suitable for use in space and nuclear applications. GaN is also optically transparent, making it a promising candidate for optoelectronic devices such as LEDs and laser diodes (WU et al., 2023).

AlN shares many of the same properties as GaN, including a wide bandgap, high thermal conductivity, and resistance to radiation damage. AlN is also highly piezoelectric, meaning it can convert mechanical energy into electrical energy and vice versa. This property makes AlN an excellent material for use in surface acoustic wave (SAW) devices, which are used in wireless communication systems. AlN-based SAW devices are highly efficient and can operate at high frequencies, making them suitable for use in mobile devices, radar systems, and other applications (RODRÍGUEZ-MADRID et al., 2012).

Both GaN and AlN have gained significant attention in recent years due to their unique properties and potential for use in various applications. Research on GaN and AlGaN topics has been growing over the past 10 years, but it is still not extensively explored by Brazilian researchers Figure 1. Ongoing research is focused on developing new materials and device architectures that leverage the properties of these two semiconductors to enable the next generation of high-performance electronics and optoelectronics.

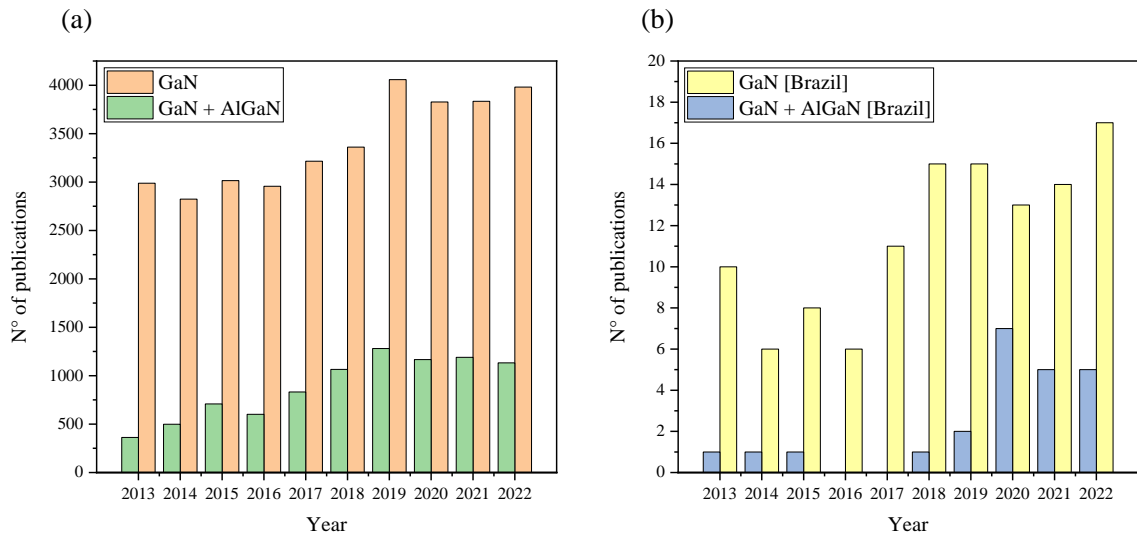


Figure 1: Number of publications on the topics “GaN” and “GaN+AlGaN” over the past 10 years (a) worldwide and (b) in Brazil. Obtained from SCOPUS database.

Traditionally, these thin films are produced using expensive techniques such as metalorganic chemical vapor deposition (MOCVD), metalorganic vapor phase epitaxy (MOVPE), or molecular beam epitaxy (MBE), which require high temperatures (JUNAID et al., 2018; LU et al., 2004; NI et al., 2015). However, magnetron sputtering deposition is a well-established process that can produce high-quality thin films of III-nitrides, such as AlN and GaN, at a lower cost (SCHIABER et al., 2013; SHIGEKAWA et al., 2007; SIGNORE et al., 2013). This technique is compatible with various materials and sizes and can operate at low temperatures.

SAW devices are widely used in various electronic applications such as communication systems, sensors, and filters. These devices rely on the propagation of surface acoustic waves through a piezoelectric material, which converts electrical signals into mechanical vibrations and vice versa. Gallium nitride and aluminum nitride are two materials that have gained significant attention in the development of SAW devices (RODRÍGUEZ-MADRID et al., 2012).

GaN has excellent piezoelectric properties, which make it suitable for SAW device applications. Its high electron mobility and good thermal conductivity also make it a promising candidate for high-frequency and high-power SAW devices. Moreover, GaN has a wide bandgap, which allows for the fabrication of high-temperature and high-power devices.

AlN, on the other hand, has a higher piezoelectric coefficient than GaN, making it an excellent material for SAW devices. Its high acoustic velocity and high acoustic impedance also make it a suitable candidate for SAW applications. In addition, AlN has a low temperature coefficient of frequency, which means that its resonant frequency remains stable over a wide temperature range (RODRÍGUEZ-MADRID et al., 2012).

Both GaN and AlN have been extensively studied for SAW device applications, and several studies have demonstrated their potential for high-performance and high-frequency SAW devices. In particular, the use of GaN/AlN heterostructures has been shown to improve the performance of SAW devices, as it allows for the design of more complex device structures and enhances the piezoelectric properties of the materials (BARTOLI et al., 2018; MANDAL; BANERJEE, 2022).

In conclusion, GaN and AlN are two promising materials for the development of high-performance SAW devices. Their excellent piezoelectric properties, high electron mobility, and good thermal conductivity make them attractive candidates for high-frequency and high-power applications. Further research is needed to optimize their performance and reduce their cost, which will pave the way for the widespread use of GaN and AlN in SAW devices. While AlN thin films have been produced with reactive magnetron sputtering deposition for SAW devices, there are few recent reports on AlGa_xN thin films and none on GaN/AlGa_xN heterostructures using this deposition technique (RODRÍGUEZ-MADRID et al., 2012; TIGLI; ZAGHLOUL, 2010). Therefore, this study focuses on filling this gap in the state-of-the-art of III-nitrides.

Furthermore, SAW sensors have promising applications in the biomedical field, such as real-time protein or antigen analysis, enabling rapid and accurate detection of bacteria or viruses (BACA et al., 2015; JIANG et al., 2015; TIGLI; ZAGHLOUL, 2010).

The challenges and difficulties previously mentioned underscore the significance of investigating the deposition and characterization of thin films and heterostructures of GaN and Al_xGa_{1-x}N using reactive magnetron sputtering. In this context, a heterostructure is defined as a multiple layer thin film, consisting of a layer of interest (the GaN layer) and one or more buffer layers (the Al_xGa_{1-x}N layers). Specifically, the enhancement of the GaN layer through the use of an AlGa_xN buffer is of special interest. The study of these thin films is concentrated on properties that make them suitable for application in SAW sensors, which is of great interest to the aerospace and biomedical industries.

1.2 Research objectives

The main objective of this research is to produce and characterize the different properties of $\text{Al}_x\text{Ga}_{1-x}\text{N}$ thin films and heterostructures with GaN using reactive magnetron sputtering deposition technique. To achieve this goal, the following specific objectives are outlined:

- i. Deposit $\text{Al}_x\text{Ga}_{1-x}\text{N}$ films on glass substrates;
- ii. Deposit $\text{Al}_x\text{Ga}_{1-x}\text{N}$ films on Si substrates with different crystalline orientations, namely (100), (110) and (111);
- iii. Study the influence of the Al content on the optical, vibrational, and crystalline properties of the $\text{Al}_x\text{Ga}_{1-x}\text{N}$ films;
- iv. Compare the influence of the substrate on the different studied properties of the films;
- v. Optimize the *c*-axis orientation and crystalline quality of the $\text{Al}_x\text{Ga}_{1-x}\text{N}$ films according to Al content;
- vi. Deposit GaN/ $\text{Al}_x\text{Ga}_{1-x}\text{N}$ heterostructures in different substrates (glass and Si);
- vii. Characterize the different heterostructures in terms of crystalline quality, optical and vibrational properties, and surface morphology;
- viii. Understand the effect of the different AlGaN buffer layer on the GaN film.

2 Literature Review

The following sections will briefly discuss up-to-date information surrounding III-nitrides properties and magnetron sputtering deposition process, enough to support the discussed results.

2.1 AlGaN and GaN thin films and heterostructures

GaN, AlN and AlGaN are often referred as group III nitrides, composed of an element from group III (Ga, Al, In, B, etc.) and nitrogen, forming such materials. They are highly attractive semiconductor materials that exists in wurtzite, zinc-blende, or rock-salt structures. Of these, the wurtzite structure is more stable and easier to synthesize, and possesses a number of remarkable properties. The wurtzite structure is a hexagonal structure (Figure 2a), with a unit cell as shown in Figure 2b.

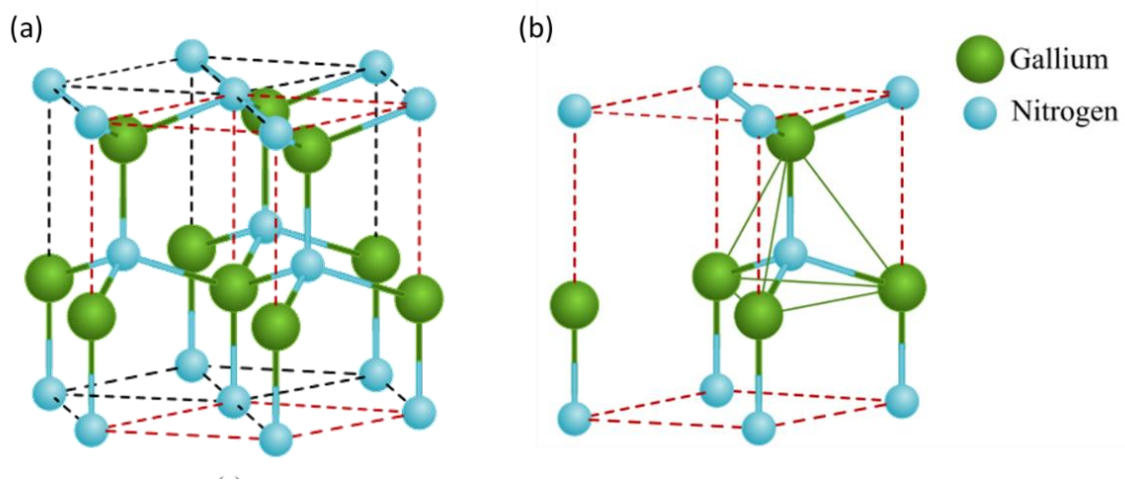


Figure 2: (a) Crystalline structure of wurtzite GaN and (b) its unit cell. Adapted from (UDABE; BARAIA-ETXABURU; DIEZ, 2023).

One of GaN most notable features is its wide and direct bandgap of 3.4 eV. GaN also exhibits high thermal conductivity ($\sim 130 \text{ W}\cdot\text{m}^{-1}\text{K}^{-1}$), good chemical stability, and thermal resistance. Furthermore, it has a refractive index of 2.33 (at 1 eV) and is piezoelectric, which makes it ideal for various optoelectronic devices. In addition, GaN has thermal expansion coefficients of $\Delta a/a$ and $\Delta c/c$ of 5.59 and 3.17, respectively. Taken together, these properties

make GaN a versatile and highly desirable material for a wide range of applications in the field of electronics and optoelectronics (HARIMA, 2002; MEDJDOUB; INIEWSKI, 2017).

AlN is a promising material for a wide range of applications due to its unique properties. AlN thin films have been widely investigated using various deposition techniques such as sputtering, pulsed laser deposition (PLD), atomic layer deposition (ALD), MOCVD and MBE. In addition to its excellent chemical stability and high melting point, AlN exhibits a high thermal conductivity, making it a suitable material for heat management applications. AlN also has a direct and wide bandgap of 6.2 eV on the hexagonal (wurtzite) structure, making it useful for high-power electronic devices and UV optoelectronics. AlN's high acoustic velocity of 6,000 – 8,000 m.s⁻¹ also makes it an attractive material for surface acoustic wave (SAW) devices. AlN's thermal expansion coefficients $\Delta a/a$ and $\Delta c/c$ of 4.2 and 5.3, respectively, and its refractive index of 2.15 (at 3 eV) on the wurtzite structure further enhance its properties for various applications (GILLAN, 2013; HARIMA, 2002; PANDEY et al., 2018).

Gallium nitride (GaN) thin films have been studied using several techniques, such as chemical vapor deposition (CVD) and MBE. Sputtering has also been explored for this material, using numerous different substrates such as silicon, glass, sapphire, silicon carbide, and various buffer layers including gallium nitride and aluminum nitride. Silicon substrates are more cost-effective and commonly used for GaN thin films. Monocrystalline Si wafers are well-known for their ease of production and allow for easy integration of GaN films into CMOS (complementary metal-oxide semiconductor) technology using Si (100) substrates. However, a high density of defects in the GaN film can occur due to the lattice mismatch (17 %) and thermal expansion coefficient differences between these two materials. The density of thread dislocations in III-nitride films can vary from 10⁶ to 10⁸ cm⁻¹, due to the mismatches between the film and substrates. Many researchers adopt buffer layers as a step to overcome this problem, which as a thin layer separating the main functional film from the substrate to enhance the growth of the film, adhesion, minimize lattice mismatch, help tailor the properties of the film, or improve the substrate surface properties (MEDJDOUB; INIEWSKI, 2017; XU et al., 2021; ZHAO et al., 2018).

Related to the discussion about substrates for III-nitride growth, as stated before, Si is a cheap option, but it can induce many defects in the films, while SiC can be an option for higher performance due to the low density of defects, but at a high cost. Another possibility to

overcome the defects in the films is the use of GaN bulk substrates, which have been developed but are also costly (LIU; EDGAR, 2002). Therefore, the production of III-nitride devices is limited by the substrate options available. Studies on III-nitride nanowire growth on quartz/silica glass substrates attempt to offer this substrate as an option. They have a very low cost, can be produced in many sizes and shapes, can withstand temperatures up to 1 000 °C, and show excellent optical properties such as visible and ultraviolet (UV)-region transparency (ZHAO et al., 2018).

The different Si wafer orientations are used for the deposition of GaN, AlN, and AlGaN films for various reasons. Si (111) is mainly used for epitaxial growth and high quality due to its lattice parameters and surface inducing a more *c*-oriented hexagonal film. Si (100) and Si (110) are more challenging for (0002) oriented films but are desired for microelectromechanical systems (MEMS), CMOS, and SAW devices (DADGAR et al., 2007; HAN et al., 2016; LIU; EDGAR, 2002).

Aluminum nitride and aluminum gallium nitride (AlGaN) are materials that can be used as buffer layers for GaN films on Si substrates to reduce the lattice and thermal coefficient mismatches. Recently, a study discussed the production of a high-quality and crack free epitaxial 2 μm GaN film grown on Si substrate using the MOCVD process. The study used a 6-inch (approximately 15.24 cm) Si (111) substrate with four buffer layers: ~200 nm high temperature AlN (HT-AlN), ~200 nm Al_{0.75}Ga_{0.25}N, ~250 nm Al_{0.5}Ga_{0.5}N, and ~300 nm Al_{0.25}Ga_{0.75}N. Together with nitrogen flow and growth temperature, the buffer layers had a significant influence on the quality of the GaN film by providing the necessary gradual increase in mismatch (XU et al., 2021).

Using a compositional gradient of AlGaN as buffer layer can induce the growth of high quality and crack-free GaN on Si substrates, and this topic has been covered using MOCVD (GHOSH et al., 2023). In the study, the authors explored several conditions for the AlGaN buffer layer, such as compositions, thickness of the individual layers, total thickness, and number of layers. The samples were studied in terms of stress and the authors concluded that increasing the number of steps without changing the total thickness of the sample (i.e., each individual layer becomes thinner so that are more layers in the same total thickness) does not improve the GaN final layer in terms of both mean-stress and crystalline quality. However, keeping the individual layers thicknesses and increasing total thickness by adding more steps

can improve the quality of the GaN layer, and so the authors concluded that the buffer thickness individually does not affect the quality of the GaN. By this, thinner layers are optimal for material consumption and process time, and a single thin AlGaIn layer can already provide a crack-free GaN heterostructure by producing enough variation in the composition.

2.1.1 X-Ray diffraction

X-Ray diffraction is a technique which consists in examining a sample by focusing X-Ray radiation on the surface of the sample, with a wavelength in the order of the crystal lattice space. The scattering of the radiation follows Bragg's law, in which constructive interference occurs when the path difference (AB), which is proportional to λ , equals $2d \sin \theta$ (Figure 3) (MORAM; VICKERS, 2009).

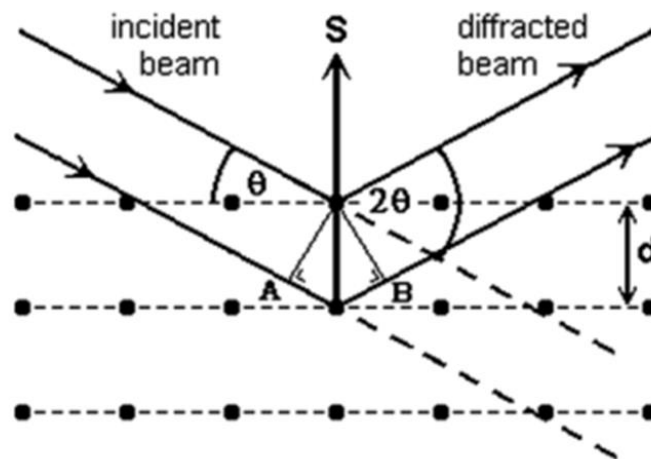


Figure 3: Representation of X-Ray diffraction with the conditions for Bragg diffraction.

Adapted from (MORAM; VICKERS, 2009).

In this technique, the X-Ray radiation interacts with the crystal lattice, resulting in diffraction patterns that provide valuable information about the material's atomic arrangement. By measuring the angles (θ) at which constructive interference occurs, one can determine the spacing (d) between the crystal planes, allowing for the identification of the sample's crystalline structure and orientation.

Thin films can be arranged as amorphous or crystalline structures. The crystalline structure consists of grains that can be oriented randomly oriented or exhibit some preferred orientation known as texture. In the case of high texture, the diffractogram obtained using an

ordinary θ - 2θ configuration may display only reflections from one family of planes, resulting in a pattern resembling that of a single crystal with broader peaks (CAPPuccio; TERRANOVA, 1996).

The powder diffraction pattern provides information about a materials crystalline structure in terms of randomly oriented grains. To identify a material or characterize its orientation and strains, the samples diffractogram can be compared to the powder diffraction pattern. Figure 4 provides the powder diffraction pattern for GaN and AlN (SCHULZ; THIEMANN, 1977).

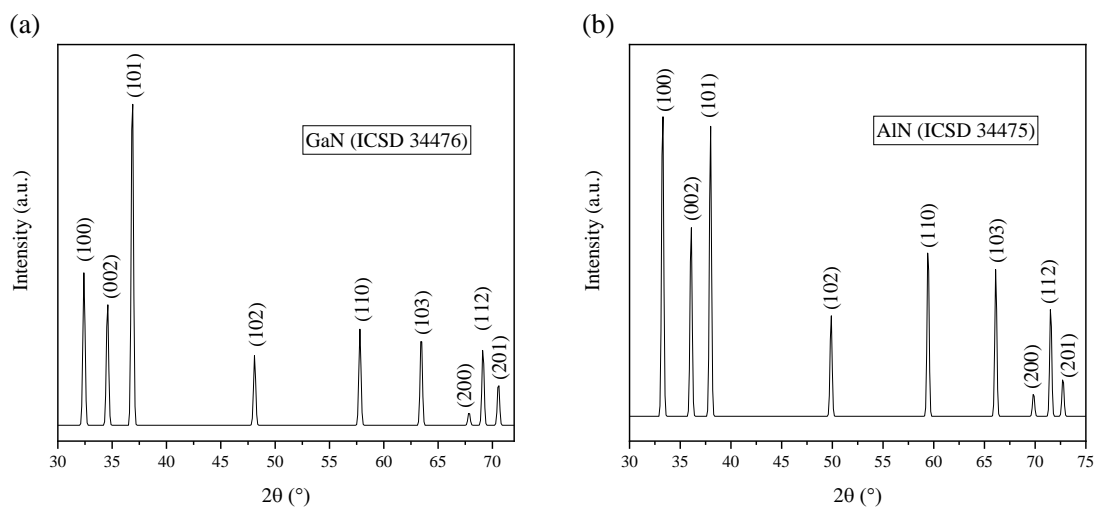


Figure 4: Powder diffraction patterns for (a) GaN and (b) AlN. Constructed using the data from (SCHULZ; THIEMANN, 1977)

Aluminum nitride thin films have been successfully sputtered onto Si substrates by several different studies. Although the sputtering deposition of AlN is well-known, the topic is still quite relevant, with recent studies on different properties, substrates, and deposition parameters. Focusing on structural properties, *c*-axis-oriented wurtzite AlN thin films have been reported by many researchers. The preferred crystallographic orientation on nanostructured thin films is common and usually depends on the substrate. The X-ray diffraction (XRD) pattern shows this preferred orientation by means of a high-intensity peak when compared to others (PANDEY et al., 2021).

A study conducted in 2018 investigated the direct current (DC) reactive sputtering deposition of AlN on Si (100) and Si (110) substrates, which are less commonly used for

hexagonal growth compared to the more established Si (111) substrate. The study successfully produced *c*-oriented films, with the XRD patterns for samples on both substrates showing an intense (0002) peak in comparison to the (100) peaks, indicating a preferred orientation on the hexagonal *c*-axis. The authors made this assumption by comparing the samples' diffractograms to corresponding diffraction data and calculated the texture coefficient of the films along the (0002) direction, obtaining values of 3.1 and 2.8 for Si (100) and Si (110), respectively. The authors also estimated the average crystallite size using the Scherrer equation as approximately 20-30 nm and 30-40 nm for Si (100) and Si (110), respectively. To determine the crystalline quality and texture for both samples, through the full width at half maximum (FWHM) of the peaks on rocking curve analyses were used. The authors found that the film on the Si (100) substrate exhibited better crystalline quality (PANDEY et al., 2018).

The growth of highly *c*-oriented hexagonal AlN thin films using sputtering deposition is not a recent achievement. In 2015, a study using unbalanced magnetron sputtering achieved highly *c*-axis oriented films with an XRD pattern with a sharp and strong (0002) peak, with a high relative intensity between the (0002) and the (100) peak. Rocking curve analyses showed a 4.0° for the sample, confirming its crystalline quality (KE et al., 2015). A study from 2014 using high power impulse magnetron sputtering (HIPIMS) observed the effect of several deposition parameters on the AlN film properties. The authors also observed an increase in the (0002) peak intensity with a simultaneous decrease in the (100) peak (CHANG et al., 2014).

ZHANG et al., 2005, compared AlN thin films sputtered on Si (100) and Si (111) substrates. The films on Si (111) substrates showed a more controlled (0002) preferred *c*-axis orientation due to the match in lattice parameters between the substrate and the film. The FWHM for the (0002) peak of the AlN films was also smaller on Si (111), indicating samples with fewer strains and defects.

Several studies have investigated the influence of film thickness on FWHM of diffraction peaks and found a strong correlation. Generally, there is a decrease in FWHM with an increase in film thickness, up to a certain level, as exemplified in Figure 5 (DUQUENNE et al., 2008; LEE; JOO; KIM, 2014; RODRÍGUEZ-MADRID et al., 2012; SEON et al., 2000; SUN et al., 2016). Specifically on sputtered AlN films, which is relevant to the samples in this work, DUQUENNE et al., 2008 demonstrated a strong relationship between thickness and the (0002) AlN diffraction peak, up to approximately 1.5 \AA Figure 5a. The authors correlated this

behavior with the randomly oriented crystals found at the interface between the film and substrate, which become more aligned and straight as growth continues. A study on GaN thin films also showed a similar behavior, with good agreement on the thickness around 1.5 μm where the FWHM begins to stabilize (Figure 5b) (SEON et al., 2000). The authors attributed this behavior to the three-dimensional growth observed at the start of the film.

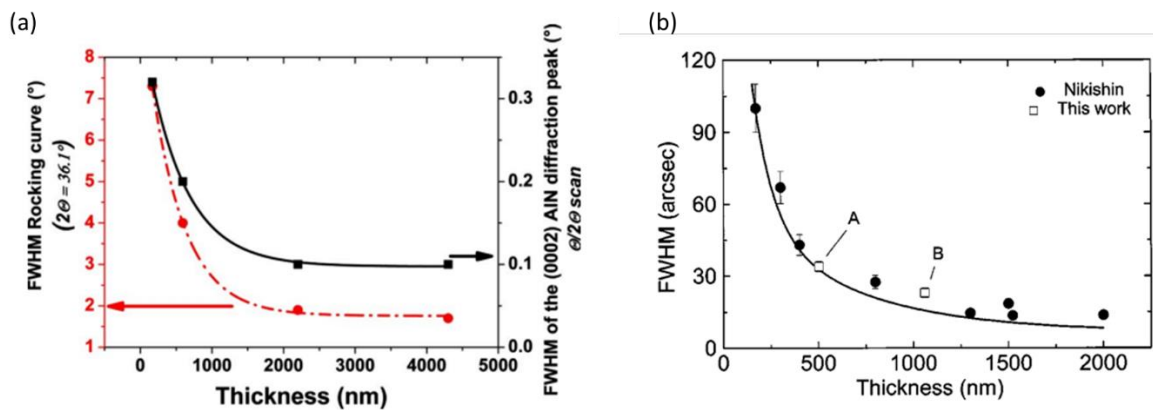


Figure 5: Relationship between film thickness and FWHM for (a) sputtered AlN (DUQUENNE et al., 2008) and (b) MBE-grown GaN (SEON et al., 2000).

An XRD analysis of $\text{Al}_x\text{Ga}_{1-x}\text{N}$ epitaxial layers with various Al contents (x) on sapphire substrates, produced using the MOCVD technique, showed pronounced (0002) peaks for the $\text{Al}_x\text{Ga}_{1-x}\text{N}$, which shifted with the value of x . The lattice parameter c , calculated from the (0002) peak position, decreased with the Al content in the samples. The FWHM of the (0002) peak became wider as the Al content increased in the different samples, which was attributed to an increase in the tilting component of the misorientation (WANG et al., 2017).

2.1.2 Raman spectroscopy

Raman spectroscopy is a powerful tool for characterizing the structural and vibrational properties of materials, including wide-bandgap semiconductors such as gallium nitride (GaN) and aluminum nitride (AlN). It arises from the inelastic scattering of light by lattice vibrations, or phonons, in a material. When an incident monochromatic light hits a material, it undergoes effects of absorption and transmission, and a small part is scattered in all directions. Raman scattering is a phenomenon in which a small part of the incident energy shows a different

frequency when it scatters. The resulting Raman spectrum provides information on the phonon modes, crystalline structure, and defects present in the material.

Crystalline materials can exhibit various defects and modifications due to crystal growth or mechanical works, such as microstructure changes, residual stresses, lattice deformations, and phase transformations. These modifications can be characterized using Raman spectroscopy, which is an easy-to-access and non-destructive technique that requires no sample preparation. The position, dislocation, FWHM, and intensity of the peaks provide information about the sample. (XU et al., 2018).

In the case of GaN and AlN, Raman spectroscopy is particularly useful for studying their vibrational properties. When the monochromatic light interacts with an electron from the sample on an electronic state E, it absorbs energy going into a virtual, non-stable, electronic state. Once this electron releases the absorbed energy, it returns to an electronic state that could be different than the original one, being more or less energetic. In such cases, Raman scattering occurs.

In GaN and AlN, Raman spectroscopy is commonly used to investigate the E_2^H phonon mode, which arises from the stretching vibration of the N atoms along the *c*-axis of the wurtzite crystal structure. This mode is particularly sensitive to strain and defects in the material, and its frequency and intensity can be used to extract information on the crystalline quality and strain state of the material. For example, a redshift in the E_2^H mode frequency is often observed in strained GaN films grown on lattice-mismatched substrates. The frequency of this mode is also sensitive to the Al content in $Al_xGa_{1-x}N$ alloys, and can be used to determine the composition of the material.

For hexagonal structures, eight phonon modes are predicted, and among them, six are optical modes, and the atomic displacement is shown in Figure 6. In wurtzite structures of III-nitrides such as GaN and AlGa_xN, the two B_1 modes are silent, and the A_1 , E_2 , and E_1 optical phonon modes are usually observed depending on the polarization geometry.

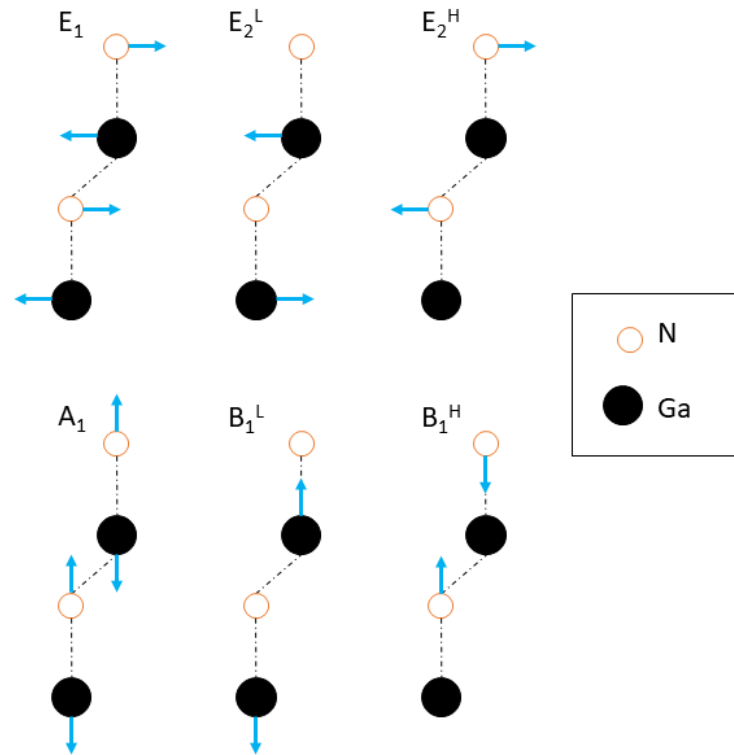


Figure 6: Schematic of the optical phonon modes observed in wurtzite structures. Elaborated by the author.

The $A_1(\text{LO})$ phonon mode is typically observed at 734 cm^{-1} for GaN and 890 cm^{-1} for AlN on the Raman spectra. For AlGaN compounds, this phonon mode shifts greatly with composition. The E_2^H mode, with a higher frequency and strongest signal, is the most commonly observed from the two E_2 phonon peaks that are active on Raman spectroscopy analyses for hexagonal III-nitrides. The E_2^H typical position is at 567.7 cm^{-1} and 657.4 cm^{-1} for GaN and AlN, respectively, and the peak position is also expected to shift with the Al content. The E_1 transverse optical mode is expected at 558.8 cm^{-1} and 670.8 cm^{-1} for GaN and AlN, respectively, and it can be mixed with the E_2^H mode when their width is too large. The typical phonon frequencies for GaN and AlN films are depicted in Table 1 (HARIMA, 2002).

Table 1: Typical phonon Raman frequencies for wurtzite GaN and AlN films at room temperature (HARIMA, 2002).

Phonon mode	AlN (cm^{-1})	GaN (cm^{-1})
E_2^L	248.6	144
$A_1(\text{TO})$	611	531.8
$E_1(\text{TO})$	670.8	558.8
E_2^H	657.4	567.6
$A_1(\text{LO})$	890	734
$E_1(\text{LO})$	912	741

The behavior of the peak positions with the composition of wurtzite $\text{Al}_x\text{Ga}_{1-x}\text{N}$ samples differs from one phonon mode to another. The $A_1(\text{LO})$ and $E_1(\text{LO})$ modes shift to higher energies with increasing Al content. The $A_1(\text{TO})$, $E_1(\text{TO})$, and E_2 modes behave as two-mode, with paths starting from $x = 0$ (GaN-like) and $x = 1$ (AlN-like), as depicted in Figure 7.

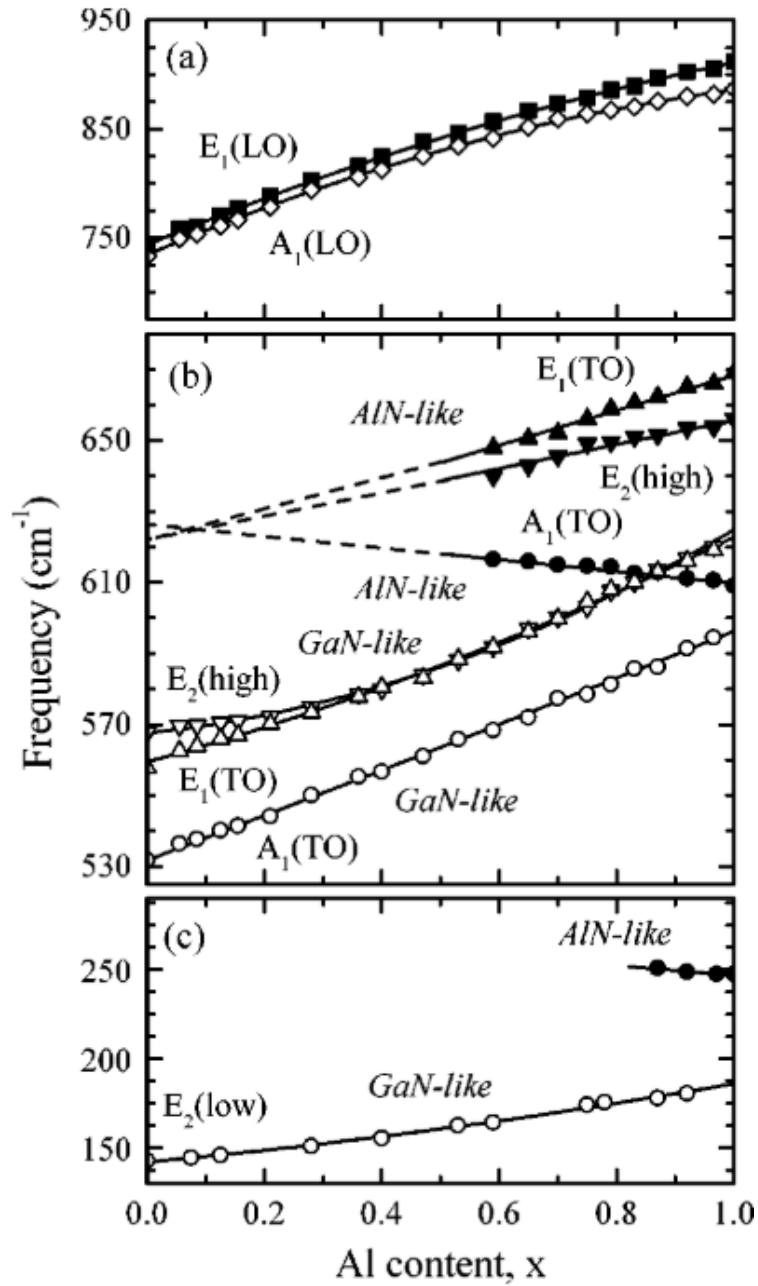


Figure 7: Phonon frequencies in wurtzite $\text{Al}_x\text{Ga}_{1-x}\text{N}$ alloys as a function of the Al content (DAVYDOV et al., 2002).

A function to approximate the position for the wurtzite $\text{Al}_x\text{Ga}_{1-x}\text{N}$ peaks was proposed by Davydov *et al.* considering a bowing of the curves (DAVYDOV et al., 2002). For the $A_1(\text{LO})$, $E_1(\text{LO})$, $A_1(\text{GaN-like TO})$ and $E_2^{\perp}(\text{GaN-like})$ peaks, the proposed equations were:

$$A_1(\text{LO}) = 734 + 153(x) + 75(x)(1-x) \quad \text{Equation 1}$$

$$E_1(\text{LO}) = 742 + 170(x) + 65(x)(1-x) \quad \text{Equation 2}$$

$$A_1(\text{GaN-like TO}) = 531.8 + 64.5(x) - 1.9(x)(1-x) \quad \text{Equation 3}$$

$$E_2^L(\text{GaN-like}) = 142.8 + 43.5(x) - 14.5(x)(1-x) \quad \text{Equation 4}$$

where x is the Al molar fraction.

However, the E_2^H peak shows much more complicated behavior for $\text{Al}_x\text{Ga}_{1-x}\text{N}$ alloys. Firstly, the changes in the spectra observed are different for different composition ranges. From a certain composition ($x = 0.28$), the E_2^H and $E_1(\text{TO})$ phonon modes start to mix and are impossible to distinguish, up to $x = 0.7$. Also, for compositions $x > 0.36$, there is a shoulder on the peak at a higher frequency. After $x = 0.7$, the two modes are again distinguished (DAVYDOV et al., 2002). This creates much-complicated analyses for the position of the peaks and how to determine the quality of the sample. Broadening of the peaks would also highly influence the observed spectra and analyses. A study of $\text{Al}_x\text{Ga}_{1-x}\text{N}$ thin films on sapphire substrates with an AlN buffer layer shows Raman spectra for different values of x , with clear shifting of the E_2^H and $A_1(\text{LO})$ peaks to higher values of wavenumber as the Al content increases (FENG et al., 2019).

In summary, Raman spectroscopy is a powerful tool for characterizing the structural and vibrational properties of GaN and AlN materials. The information obtained from Raman spectra can provide insights into the crystalline quality, strain state, and composition of these materials, and can help guide the optimization of their growth and processing for various applications.

2.1.3 Optical properties

GaN and AlN are two important wide bandgap semiconductors that have gained significant attention due to their unique optical properties. GaN has a direct bandgap of 3.4 eV and AlN has a direct bandgap of 6.2 eV, making them ideal materials for applications in optoelectronics and high-power electronics. The bandgap is the range of forbidden energy states and is the gap between the valence and conduction band of a solid material. For semiconductor materials, the charge carriers can overcome the energy gap when excited, allowing for specific properties for this type of material and its application in transistors, LEDs, etc. Wide bandgap semiconductors are those whose bandgap is larger than most conventional ones, which includes

GaN and AlN. They usually show more capability for working in high-temperature and power environments.

The theoretical bandgap for $\text{Al}_x\text{Ga}_{1-x}\text{N}$ thin films can vary from 3.42 eV (GaN) to 6.2 eV (AlN), in the UV range. This variation is non-linear with the Al content in the alloy, as described by the following equation (PANTHA; LIN; JIANG, 2012):

$$E_g = (1-x)E_{g(\text{GaN})} + (x)E_{g(\text{AlN})} - b(x)(1-x) \quad \text{Equation 5}$$

where x is the Al molar fraction.

Values for the bowing parameter b can be positive (upward) or negative (downward), with reported values ranging from -0.88 eV to +2.6 eV, as stated in a 2002 review study (YUN et al., 2002), and a more recent, narrower range of 0.6 to 1.3 eV was reported (PANTHA; LIN; JIANG, 2012). This wide range can be attributed to the use of different processes for the deposition of thin films, resulting in varying quality of the samples, and different ranges of x used in the studies (PANTHA; LIN; JIANG, 2012).

The bandgap also has a relation to the lattice parameter a for AlGaN alloys, as well as III-nitrides in general, as shown in Figure 8 (SCHUBERT, 2006). This lattice parameter changes with the Al content in the films, resulting in changes in the bandgap.

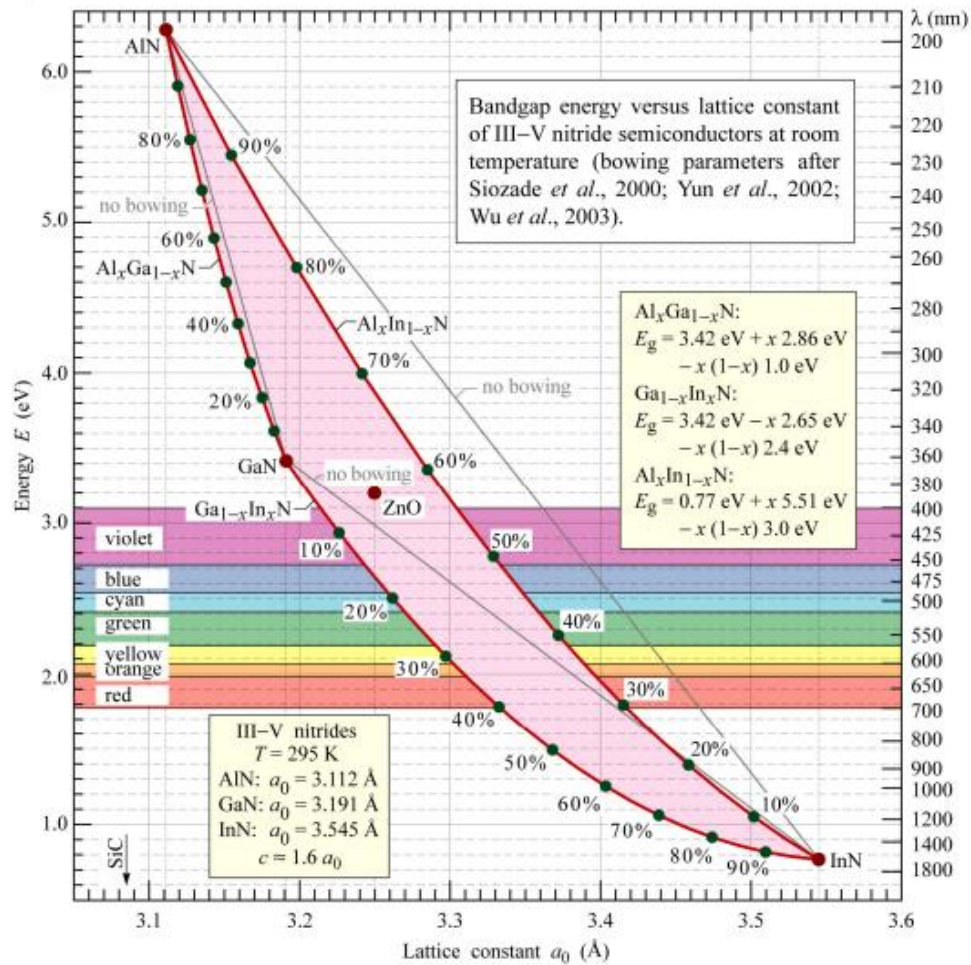


Figure 8: Bandgap dependence on the lattice constant for III-nitrides (SCHUBERT, 2006).

The refractive index n can be described by the following equation (FEYNMAN; LEIGHTON; SANDS, 2011):

$$n = 1 + \frac{Nq_e^2}{2\epsilon_0 m_e (\omega_0^2 - \omega^2)} \quad \text{Equation 6}$$

where N is the volumetric density of charges, q_e is the electron charge, ϵ_0 is the permittivity of vacuum, m_e is the electron mass, ω_0 is the resonant frequency of an electron bound in an atom and ω is the frequency of the radiation.

The equation provides an initial notion about the different aspects of a material that can affect the refractive index. Indeed, different materials with the same composition might show different experimental values of n , which could be explained by the fact that different processes

for material production can lead to different qualities and densities of defects (vacancies, dopants, impurities, etc.).

The presence of point defects in a material (such as vacancies and substitutes) can influence in the optical properties. The static refractive index (n) and static dielectric constant (ϵ) of a material can increase in the presence of the defects, and are related by $\epsilon = n^2$. This would also lead to lower values of the bandgap when compared to perfect structures (TIAN et al., 2020). The point defects in $\text{Al}_x\text{Ga}_{1-x}\text{N}$ were shown to originate from cation vacancies or related complexes and highly increase with the Al content in the alloy (HENRY et al., 2012).

Optical transmittance shows that AlN films are transparent in the visible and infrared regions. Studies have shown values of 73.6 to 82.5 % transmittance in the visible range (400 – 700 nm). Absorption edges are at approximately 300 nm (CHANG et al., 2014). $\text{Al}_x\text{Ga}_{1-x}\text{N}$ epitaxial layers produced on *c*-plane sapphire substrates using MOCVD showed optical transmittance above 90 % in the visible range (400 – 800 nm) (WANG et al., 2017).

2.1.4 Surface morphology

The application of GaN films in high-power, high-temperature electronics, optoelectronics, and sensors requires specific surface characteristics to ensure proper functionality and optimal performance. Therefore, it is important to characterize the surface of these films to determine their suitability for various applications. Surface morphology, including roughness, defects, and crystal structure, plays a significant role in the optical and electronic properties of the film, ultimately affecting the performance of the devices in which it is utilized. Generally, a smooth surface is highly desirable for GaN films used in optoelectronic, power electronic, and high-frequency devices. Understandably, different methods of producing GaN films can result in varying surface morphologies and qualities. Techniques such as MOCVD and MBE offer superior control over film deposition and are known to produce higher-quality films with smoother surfaces (BHAT et al., 2023).

Various techniques can be employed to characterize the surface of thin films, depending on the desired level of information and precision. Scanning electron microscopy (SEM) provides high-resolution images that reveal details about the morphology, including size, shape and distribution of features. This technique allows the analysis of large areas at different magnifications to characterize film texture and detect the presence of defects or contaminants.

When combined with energy dispersive spectroscopy (EDS), SEM can also provide information about the surface composition (MIN, 2022b).

Atomic force microscopy (AFM) is another powerful tool for investigating surface morphology, enabling the acquisition of high-resolution topographic images at the nanoscale. AFM can measure parameters such as surface roughness, height variations and features like grains, steps, and defects (MIN, 2022a). Other techniques offer information about the film's surface in more indirect forms. For instance, X-ray photoelectron spectroscopy (XPS) analyzes the chemical composition of the film's surface by measuring binding energies, while ellipsometry can assess surface roughness by measuring changes in the polarization of reflected light.

The morphology of GaN films deposited onto Si (111) substrates changes with the addition of buffer layers (ARIFIN et al., 2022). In the study, the authors used SEM to investigate the surface of GaN films without buffer layer and using GaN and AlN buffer layer deposited using MOCVD. The GaN without buffer layer shows a morphology of hexagonal islands with visible separation, that indicates a three-dimensional growth without uniformity that partially covers the substrate (Figure 9a). This growth was associated to the lattice mismatch and the divergence in interfacial energy between the GaN and the substrate, indicating that an improvement could be achieved using buffer layer. The introduction of a buffer layer (GaN or AlN) created homogeneous grains, consequence of reducing the interfacial energy between substrate and the GaN film (Figure 9b to f).

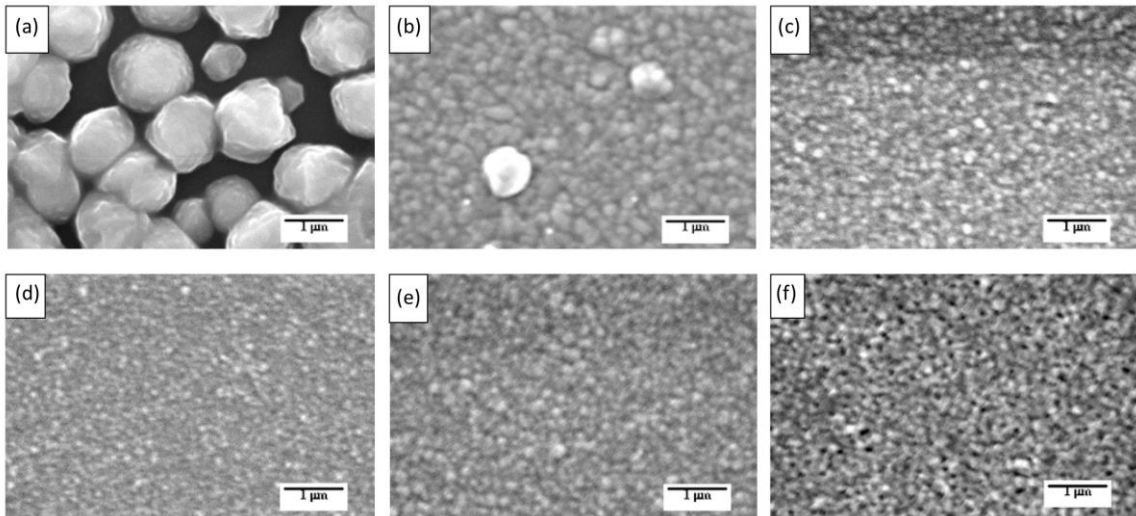


Figure 9: Surface morphology of MOCVD grown GaN films onto Si(111) with (a) no buffer layer, (b) 16 nm GaN buffer, (c) 33 nm GaN buffer, (d) 50 nm GaN buffer, (e) 29 nm AlN buffer, and (f) 44 nm AlN buffer (ARIFIN et al., 2022).

The same behavior was observed for GaN films grown by PLD on sapphire substrates when using AlN buffer layers (YANG et al., 2015). The surface was studied using both SEM and AFM techniques to observe the surface morphology and obtain roughness parameters, respectively. In their study, the authors observed that the GaN film without a buffer layer exhibited a surface with hillocks and islands and a surface root-mean-square (RMS) roughness of 11.5 nm. However, with the introduction of a thin AlN buffer layer (30 nm), the surface RMS roughness reduced to 4.0 nm, and with a thicker AlN layer (150 nm), it was further reduced to 2.1 nm. The addition of the AlN layers visibly improved the morphology of the GaN films, as observed by SEM images, and the increase in the AlN thickness proved to be valuable in achieving this improvement.

2.2 Reactive magnetron sputtering

Sputtering deposition is a physical vapor deposition (PVD) technique used to produce thin films. It is capable of generating uniform films with great thickness control and a good adhesion to the substrate, in addition to allowing reproducibility of results with good process stability. Succinctly, the process consists of generating plasma that interacts with the surface of a target material to eject atoms or molecules from its surface that may further get deposited on

the surface of a substrate. The plasma, usually composed of an inert gas such as argon, gets its ions accelerated by an electric field and they collide against the surface of the target with high energy and momentum. With enough energy to surpass the binding energy of the atoms on the surface of the target on the collision, these atoms get ejected, and the process is known as sputtering (illustrated in Figure 10). The ejected particles can condense on the surface of a substrate material, producing a thin film (ROSSNAGEL, 1999).

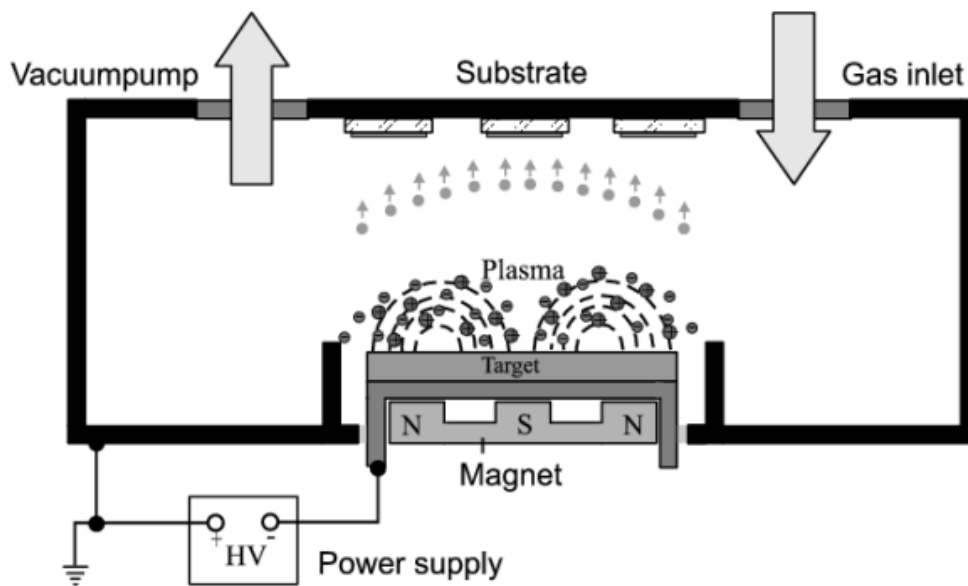


Figure 10: Basic system of a reactive magnetron sputtering deposition (NGARUIYA, 2004).

Recent developments in the sputtering deposition process have allowed this technique to standard for a wide range of industrial applications. Regarding the magnetron sputtering technique, permanent magnets are located under the surface of the target, which helps to increase the efficiency of the process and reduce the minimum pressure limit. Apart from this, reactive gases can be mixed in the plasma to participate in the final composition of the film – in the particular case of GaN being produced using a pure Ga target and a plasma with N_2 – and it is denominated reactive sputtering. When using multiple targets, alloys such as AlGaIn can be produced with controlled composition according to the power applied to each target. Magnetron sputtering technique is used in industrial processes, especially for layers on glass

materials due to high deposition rates, wide temperature ranges, parameters variation, and scaling (KE et al., 2015; KELLY; ARNELL, 2000).

Dual magnetron sputtering, in conjunction with co-sputtering, presents a versatile approach to depositing alloy materials without the necessity of fabricating a dedicated alloy target. This technique involves utilizing two separate targets, each composed of the desired elemental constituents of the alloy. Through the precise control of the power applied to each target, it becomes feasible to tune the composition of the deposited film in real-time, allowing for the tailoring of material properties to specific requirements. This method is particularly significant in applications where achieving specific alloy ratios or gradients is vital. Managing the deposition rate and composition in dual-target reactive co-sputtering is paramount for ensuring consistent and accurate alloy formation. By controlling the power distribution and adjusting process parameters, such as gas flow rates and working pressures, the resultant film's properties can be optimized to meet the desired specifications (SPROUL; CHRISTIE; CARTER, 2005).

The properties of films produced using sputtering deposition are influenced by parameters such as substrate temperature and orientation, plasma discharge power, deposition time, working pressure, distance between the substrate and target, chamber geometry, substrate rotation, and others. The plasma supply power is known to significantly affect the deposition rate and also impact the film's uniformity, surface quality, and its adhesion to the substrate. The deposition time, in accordance with the deposition rate, will impact the sample's thickness, which is correlated with the film properties such as surface roughness, grain sizes, and adhesion (MANDAL; SINGH; ROY, 2021).

When considering the substrate, temperature becomes crucial for achieving optimal film crystallinity, and requires careful examination specific to the deposited material. This temperature can impact the occurrence of defects and cracks on the films, as well as the adhesion, which is also influenced by the differing thermal expansion coefficients of the film and substrate materials. The selection and orientation of the substrate holds great significance in achieving textured films with preferred orientations, and minimizing lattice mismatch to produce high-quality films with minimal residual stresses and defects. The substrate-to-target distance plays a role in affecting the deposition rate and the distribution of grain sizes.

Increasing this distance has also been associated with improved optical quality in semiconductor materials (MANDAL; SINGH; ROY, 2020, 2021; OLIVEIRA et al., 2022).

The gas flow and concentration of reactive gas can also exert an influence on film properties, particularly concerning crystalline quality, and necessitate consideration in line with the specific material under production (SPROUL; CHRISTIE; CARTER, 2005). Studies have indicated that rich N₂ environments during reactive deposition of III-nitrides yields favorable effects on the film's properties (FURQAN; HO; KWOK, 2021; JUNAID et al., 2018; OLIVEIRA et al., 2022). The working pressure is systematically examined for varying film materials as well as the reactive and inert gases utilized. It has been demonstrated that working pressure impacts the deposition rate (and film thickness), crystalline quality, optical properties, concentration of defects, and more. This parameter typically interacts with other deposition variables, determining the appropriate pressure to customize the desired film properties (JANG; AHN; HWANG, 2022; LIM et al., 2020; SON et al., 2020).

Target poisoning is a common issue in magnetron sputtering, especially when using liquid targets and reactive gases, where compounds form on the target surface, hindering the sputtering process. During sputtering, atoms ejected from the target can re-deposit onto its surface, forming a layer. Reactive gases, like nitrogen, can interact with the target material, forming compounds with a different composition. Contaminants in the sputtering chamber, such as oxygen or iron, can also contribute to the re-deposition of unwanted compounds (GUDMUNDSSON, 2020; SPROUL; CHRISTIE; CARTER, 2005).

The operation of the reactive magnetron sputtering process is highly susceptible to the hysteresis phenomenon, which entails a non-linear relationship between process parameters and material properties during film growth and target etching. This phenomenon can lead to undesired process conditions, affecting the long-term stability of the system and the material production. The primary cause of this hysteresis is target poisoning. This phenomenon makes optimizing deposition parameters for achieving specific film properties challenging and is directly linked to achieving reproducible and tailored thin film properties in reactive sputtering processes. To counteract this challenge, one should meticulously analyze the results and systematically study the desired film material (STRIJCKMANS; SCHELFHOUT; DEPLA, 2018).

The buildup of material from target poisoning can negatively affect the sputtering process, leading to decreased film quality, altered film composition, and reduced deposition rate. As the unwanted material accumulates on the target surface, the effective sputtering area reduces, resulting in fewer sputtered atoms and a decreased deposition rate. Material with a different composition on the target surface can change the composition of the sputtered film, leading to films with undesired properties (SPROUL; CHRISTIE; CARTER, 2005).

This phenomenon can occur in both DC and RF plasmas. However, RF plasma sources reduce the risk of target poisoning, due to their high efficiency of ionization and the energy provided to the process, which minimizes the chances of depositing material on the target surface. This extends the target's life and ensures consistent film quality (SPROUL; CHRISTIE; CARTER, 2005).

Various methods can reduce the effects of target poisoning, such as tuning the sputtering rate and power supplied to the plasma, etch-cleaning the target (in-situ plasma cleaning) before deposition; selecting a less susceptible target material, applying substrate bias to increase bombardment on the substrate surface, instead of the target; and increasing the target-to-substrate distance (SAFI, 2000; SCHILLER; BEISTER; SIEBER, 1984).

The use of RF plasma sources in magnetron sputtering enhances efficiency, deposition rate, and film quality. RF plasma, creating a higher-density plasma with ions and electrons compared to DC plasma. This process can be conducted at lower working pressures than DC sputtering (GUDMUNDSSON, 2020). RF plasma sources. The RF plasma sources offer several advantages, such as efficient ionization the gas, leading to higher ion concentration, that enhances the sputtering yield, resulting in higher deposition rates and reduced processing times. The increased also improves film adhesion, reduces defects and enhances film density, resulting in higher-quality films compared to those produced using DC magnetron sputtering (DEPLA; MAHIEU; DE GRUYSE, 2009; SPROUL; CHRISTIE; CARTER, 2005).

If the target is an insulating material or develops an insulating compound on its surface, it can charge up, and cause an arc to occur if it reaches breakdown voltage. Arc formation is undesirable as it results in splashing and droplets being ejected from the target surface, negatively affecting the film's quality. RF plasma is usually implemented to mitigate this problem (GUDMUNDSSON, 2020; SPROUL; CHRISTIE; CARTER, 2005).

2.2.1 III nitrides studies

Several studies have addressed the use of magnetron sputtering for GaN and AlN thin films, with recent research focusing on the influence of deposition parameters on film quality. Epitaxy of GaN thin films and nanorods, as well as multiple reviews on the subject, have been explored in this context. Hence, magnetron sputtering is a well-established process for the production of III-nitrides (GUO; NISHIO; OGAWA, 2000; LI et al., 2022; PRABASWARA et al., 2020).

Working with liquid Ga as a target material presents a challenging aspect. While alternative solid target sources exist, the utilization of pure Ga as a target often holds advantages due to its high deposition rate, erosion avoidance, and the ability to control film composition. This becomes particularly significant when employing co-sputtering for alloys formation and film doping. However, considering that pure Ga possesses a low melting point of 29 °C and remains in liquid state during the deposition process, the design of the deposition system and container becomes critical. The liquid target must be stable, devoid of air pockets, and securely contained to prevent spillage during deposition. The choice of material to encase the liquid is also crucial due to pure Ga's low wettability. Overcoming the formation of a native oxide layer on Ga target's surface, resulting from its reactivity with oxygen, adds to the challenges associated with using a liquid target. To address these difficulties, the careful selection of deposition parameters, cooling systems and geometric configurations becomes indispensable (PRABASWARA et al., 2020).

A study on the growth of GaN on Si (111) using magnetron sputtering showed the effects of several parameters, including the sputtered gas ratio, chamber pressure, and sputtering power on the quality of the films (FURQAN; HO; KWOK, 2021). The samples were studied by means of XRD, micro-photoluminescence, and Raman spectroscopy to optimize the parameters for obtaining a film with high quality. The study concluded that the best parameters were a N₂/Ar gas ratio of 41:9 (an atmosphere rich in N₂), 7.5 mTorr (the lowest pressure used), 70 W for the sputtering power (compared to the tested 25, 55, 90, and 110 W), and a temperature of 450 °C (the highest tested).

The study of GaN thin films on different substrates – glass and different Si orientations (100), (110) and (111) – showed the effects of working pressure and RF power on the quality

of the films, by means of XRD, Raman spectroscopy, spectroscopic ellipsometry, SEM, and AFM characterizations (OLIVEIRA et al., 2022). The study concluded that the lowest tested pressure (3 mTorr) was the more adequate, along with a sputtering power of 60 W.

The growth of epitaxial GaN using magnetron sputtering has been reported by multiple authors using either DC or RF sources. However, this was achieved using sapphire substrates and high temperatures (from 700 to 1 050 °C) (PRABASWARA et al., 2020).

AlN thin films are well-established when deposited using magnetron sputtering, with several studies covering their processing on different substrates, including various Si orientations and glass (CHENG et al., 2003; DUQUENNE et al., 2008; KE et al., 2015; LI et al., 2019; PANDEY et al., 2018; TAKEUCHI; OHTSUKA; FUKUYAMA, 2015; ZHANG et al., 2005). Different film properties, such as the induced preferred orientation along the *c*-axis, crystalline quality, strains, and optical properties, as discussed previously, have been shown to depend on deposition parameters such as discharge power, pressure, substrate temperature, and gas flow (IQBAL; MOHD-YASIN, 2018). These correlations will be discussed in the following paragraphs.

In a study conducted in 1998, structural properties of AlN films produced using PLD and sputtering were compared (JAGANNADHAM et al., 1998). The films were deposited onto Si(111) substrates at varying substrate temperatures and characterized using several techniques including XRD, transmission electron microscopy (TEM), Raman and Fourier transform infrared spectroscopy (FTIR), and scratch tests. The intensity and FWHM of the XRD peaks, along with the crystallite sizes of the films produced by both PLD and sputtering were comparable. Both techniques resulted in films containing a fraction of the amorphous phase, as observed through Raman spectroscopy. The authors also concluded that an increase in thickness (for temperatures below 800 °C) led to increased compressive stresses in the films. These stresses can arise from different factors, such as defects (vacancies, dislocations, grain boundaries, impurities) generating intrinsic stresses, lattice mismatch between the film and substrate, and thermal stress due to differing thermal expansion coefficients. The sputtered films exhibited poorer adhesion to the substrate compared to the PLD film but displayed lower stresses, lower oxygen impurity, and comparable crystalline quality. Therefore, sputtering was shown to be a favorable technique for producing large-area AlN films on Si substrates.

The effect of nitrogen concentration on the properties of low-temperature sputtered AlN films was demonstrated in terms of preferred orientation and morphology using XRD and field emission SEM (CHENG et al., 2003). Results indicated that at low nitrogen concentrations (25 % and 50 %), the films exhibited a (100) preferred orientation, transitioning to a mixture of (100), (101), and (002) preferred orientations as the nitrogen concentration increased to 75 %, At 100 % nitrogen concentration, the films predominantly exhibited a (002) preferred orientation. The presence of a strong and intense Raman E_2^H peak was correlated with films showing a higher degree of (002) orientation. These films displayed an increase in the shift position as N_2 concentration increased, indicating residual stresses. The presence of argon inert gas during deposition was also found to be important for the deposition rate, which decreased in the 100 % N_2 atmosphere film.

Epitaxial AlN films were successfully deposited onto AlGaIn/GaN/sapphire structures using DC magnetron sputtering at low temperatures (< 250 °C) (DUQUENNE et al., 2008). The authors demonstrated the feasibility of depositing epitaxial AlN through sputtering without requiring high temperatures or monocrystalline substrates. However, to achieve high-quality films, the authors utilized MOCVD-grown AlGaIn/GaN layers on sapphire as a substrate for the AlN films. While MOCVD is a more expensive and intricate process compared to sputtering and involves higher temperatures, and sapphire substrates are significantly more expensive than monocrystalline Si substrates, the authors optimized deposition parameters to achieve highly *c*-oriented films even under less favorable epitaxial growth conditions (i.e., low temperatures). The use of an AlGaIn layer was found to play a crucial role in this achievement.

The sputtering power has an effect on AlN films. The surface characteristics, residual stress, and crystal quality of pulsed DC reactive sputtered AlN films were studied, and the authors found that although all deposition powers generated *c*-axis oriented AlN, increasing DC power led to rough and damaged surfaces within the studied range (200 to 1 000 W). (TAKEUCHI; OHTSUKA; FUKUYAMA, 2015). On Si substrates, the discharge power of RF magnetron sputtering was found to influence the preferred orientation and stresses in the films. However, for Si(100), however, the lattice mismatch between the substrate and AlN contributed more to the strains than the sputtering power did (ZHANG et al., 2005).

The deposition pressure in the sputtering process is also a crucial parameter when considering the production of high-quality AlN films, and it was found to influence the

structural and optical properties of AlN deposited on Si(100) (LI et al., 2019). As the deposition pressure decreased within the studied range (0.12 – 0.5 Pa), the deposition rate increased, and the films exhibited a more *c*-axis preferred orientation. The FWHM was smaller for the low-pressure samples, indicating better crystalline quality. Surface roughness measured using AFM was also lower for the low-pressure samples. This indicates an advantage in producing AlN films through sputtering deposition using low pressure. However, the residual stresses in the films decreased with increasing pressure, highlighting the need to carefully select the deposition parameters according to the desired film properties.

3 Experimental procedure

3.1 Sputtering system

All depositions were carried out in a III-nitrides (AlN, GaN and InN) dedicated sputtering system at the Plasma and Processes Laboratory of the Aeronautics Institute of Technology (ITA). A description of the system can also be found in the work by OLIVEIRA et al., 2022, where it was specifically used for GaN samples with different parameters.

The deposition chamber is made of 304 stainless steel (KJ Lesker, P/N SP1800S-316LN-EP), as shown in Figure 11, and is equipped with a mechanical vacuum pump and a turbo molecular pump system (NEXT 400 Edwards) that can achieve pressures lower than 1×10^{-6} Torr at room temperature.

A 4-inch magnetron (P/N TM4AS10PXF) is used for the liquid Ga target (99.999 % purity) and is located on the lower part of the chamber. A pair of supports for Al and In targets are on the side, radially directed to the center of the chamber, where the substrate holder is located. The 1-inch Al target (99.9995 % purity) was installed on the right side. The power supply is a DC supply (controlled by either power or current), which is connected to the Al target, and a radiofrequency (RF) power supply (13.56 MHz) which is connected to the Ga target.

For gas flow, argon and nitrogen are independently supplied to the system, with exclusive controlling gates to the lines. They are precisely controlled by mass flows. The N₂ gas injection is directed towards the substrate, while the Ar is directed towards the Ga target by an injection ring, which avoids target poisoning and allows for lower pressures to sustain the plasma (DEPLA; DE GRUYSE, 2004).

The substrate holder is a horseshoe-like steel holder that can accommodate a stainless-steel disc measuring 101 mm in diameter, featuring six holes of 15 mm in diameter. This design enables the simultaneous deposition of six different samples with diverse substrates. The holder is positioned on a rotating platform equipped with a heating system. This heating system incorporates an infrared lamp capable of reaching temperatures up to 650 °C, and its temperature is calibrated using an optical pyrometer. Moreover, the rotation systems can operate at speed ranging from 1 to 40 rpm, and the z-axis is adjustable with a range of 100 mm.

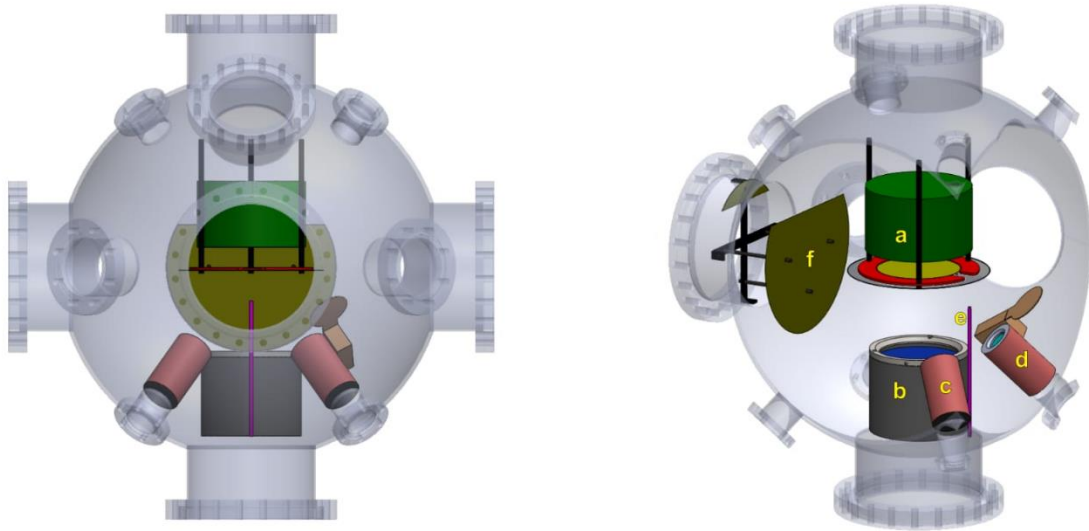


Figure 11: Representation of the deposition chamber, where *a* is the substrate holder with rotating and heating system, *b* is the gallium magnetron, *c* and *d* are the In and Al magnetrons, respectively, *e* is the nitrogen gas inlet pipe and *f* is the vacuum flange protection.

3.2 Initial exploratory study

Before systematic studying and characterizing the $\text{Al}_x\text{Ga}_{1-x}\text{N}$ samples, an exploratory study was conducted to determine the approximate composition of the alloy based on the power applied to the Al target, as this was the first deposition using Al in the sputtering system.

Three depositions were carried out using 10 W, 50 W, and 200 W, named as samples T_10, T_50, and T_200, respectively. The deposition parameters are presented in Table 2. All samples were produced using a distance of 90 mm between the Ga target and the substrate, which is the most downward position feasible for the substrate holder, considering the angling of the Al target and previous studies on Ga samples (OLIVEIRA et al., 2022). The Ga target RF power was maintained at 60 W, and the substrate rotation at 6 RPM, in accordance with the prior optimization of GaN samples generated using the same deposition system (OLIVEIRA et al., 2022). The Ar: N_2 ratio and temperature were varied on the samples to better understand how they affect the plasma stability for the deposition. The lowest pressure sustained in which the plasma was sustained was 5×10^{-3} Torr, and the Ar: N_2 ratio was changed for the first two samples to determine the possibility of sustaining the plasma at lower pressures, but without success. Thus, 5×10^{-3} Torr was the chosen pressure for the succeeding $\text{Al}_x\text{Ga}_{1-x}\text{N}$ samples.

Table 2: Deposition parameters for the initial exploratory study samples.

Sample	Al target power (W)	Temperature (°C)	Ar:N₂ ratio	Deposition time (min)
T_50 ^a	50	550	15:15	120
T_10 ^a	10	550	15:15	120
T_200	200	250	7:14	60

^aVariation of parameters on the initial time of the deposition to better adjust the plasma stability.

The substrates used for these samples varied without specificity. Only Si (100) substrates were used for sample T_50, while Si (100) and Si (110) were used for sample T_10. Sample T_200 was deposited on Si (100), Si (110), Si (111), and glass substrates.

The samples were analyzed using EDS to determine the Al content in the alloy. For each sample, three different regions were measured using a map configuration for accuracy purposes. Based on the results and the factorial design, the power for the Al and the Ga targets were selected, varying from 50 to 100 W and from 30 to 90 W, respectively.

3.3 AlGa_xN deposition

Based on the initial exploratory study and optimization of GaN samples produced using the same sputtering system, Al_xGa_{1-x}N samples were produced by varying the Al power and Ga power while keeping all other deposition parameters fixed. This decision was made to study the effect of composition on the different sample characteristics. Partial results were already published (HORTA et al., 2023).

The fixed parameters for the Al_xGa_{1-x}N samples are shown on Table 3. The power applied to the Ga and Al targets varied as previously determined. Prior to deposition, the Si substrates were cleaned in an ultrasound routine with industrial detergent, deionized water and isopropyl alcohol, in order, and etched in an HF solution (20 %) to remove oxides from the surface. The glass substrates were cleaned using the ultrasound routine.

Table 3: Fixed deposition parameters used for all $\text{Al}_x\text{Ga}_{1-x}\text{N}$ samples.

Deposition parameter	Fixed value
Temperature ($^{\circ}\text{C}$)	550
Ar:N ₂ ratio	7:14
Pressure (Torr)	5×10^{-3}
Substrate rotation (rpm)	6
Ga target-to-substrate distance (mm)	90
Deposition time (min)	120

The Ga target powers were selected as 30, 60, and 90 W, and the Al target powers were 50, 75, and 100 W. In addition, a sample was produced using only the Ga target at 60 W to produce a film with 0 % Al (GaN) to understand the effect of Al on the films in relation to a pure GaN sample. Table 4 shows the powers used on each target for each deposition. The label of the samples (S_X_Y) is related to the deposition parameters: the first number (X) is related to the power applied to the Al target, and the second number (Y) is related to the power applied to the Ga target.

Table 4: Identification of the $\text{Al}_x\text{Ga}_{1-x}\text{N}$ samples and the respective Ga and Al power used during deposition.

Sample	Al target power (W)	Ga target power (W)
S_100_60	100	60
S_50_60	50	60
S_75_60	75	60
S_0_60	0	60
S_50_30	50	30
S_100_90	100	90
S_50_90	50	90
S_100_30	100	30
S_75_30	75	30
S_75_90	75	90

All depositions were carried out using five (5) different substrates simultaneously: single-side polished silicon (100), double-side polished silicon (100) (addressed as Si (100) A and Si (100) B, respectively), silicon (110), silicon (111), and glass.

The silicon substrate samples were characterized using EDS, profilometry, and XRD. The glass substrates were characterized using EDS, XRD, Raman spectroscopy, and ultraviolet-visible (UV-Vis) spectrophotometry.

3.4 Heterostructures deposition

Following the study of the $\text{Al}_x\text{Ga}_{1-x}\text{N}$ films and their characterization, the composition of the AlGa_N layers in the heterostructures was selected based on *c*-axis preferred orientation, crystallite size, and minimization of defects observed in the optical properties. Different heterostructures were produced with varying composition, thickness, and number of $\text{Al}_x\text{Ga}_{1-x}\text{N}$ layers, as illustrated in Figure 12. The deposition time was calculated to obtain the desired thickness based on the deposition rate estimated from the $\text{Al}_x\text{Ga}_{1-x}\text{N}$ films, which will be discussed on Section 4.2.

The Si and glass substrates were cleaned using piranha etch, a mixture of 3 parts of concentrated H_2SO_4 and 1 part of 30 wt. % H_2O_2 as a standard procedure to remove organic residues. This routine was selected to improve the cleaning of substrates from the AlGa_xN films, as it is a well-established procedure for Si wafers in the semiconductor industry (DU; ZHAO; LI, 2023; MODUTEK, 2023; SCHMIDT, 2022).

A total of seven (7) different samples were deposited on Si (100) A and glass substrates for material characterization using various techniques. Three heterostructures with one layer as sample S_75_90 ($\text{Al}_{0.07}\text{Ga}_{0.93}\text{N}$) – Figure 12a – with different thicknesses were produced. Such thicknesses were 250 nm (37 min deposition), 800 nm (120 min deposition) and 1 μm (150 min deposition), in order to study the influence of the buffer layer thickness. In the same sense, two heterostructures with one layer as sample S_75_30 ($\text{Al}_{0.07}\text{Ga}_{0.93}\text{N}$) – Figure 12b – were produced with 166 nm (120 min deposition) and 250 nm thickness (180 min deposition). Besides, two more heterostructures with three and four layers were produced, according to Figure 12c and d, using buffer layers of S_75_30 ($\text{Al}_{0.37}\text{Ga}_{0.63}\text{N}$), S_50_30 ($\text{Al}_{0.24}\text{Ga}_{0.76}\text{N}$) and S_75_90 ($\text{Al}_{0.07}\text{Ga}_{0.93}\text{N}$). All the GaN layers were produced according to sample S_0_60, i.e., using 5×10^{-3} Torr and 60 W on the Ga target during 120 minutes.

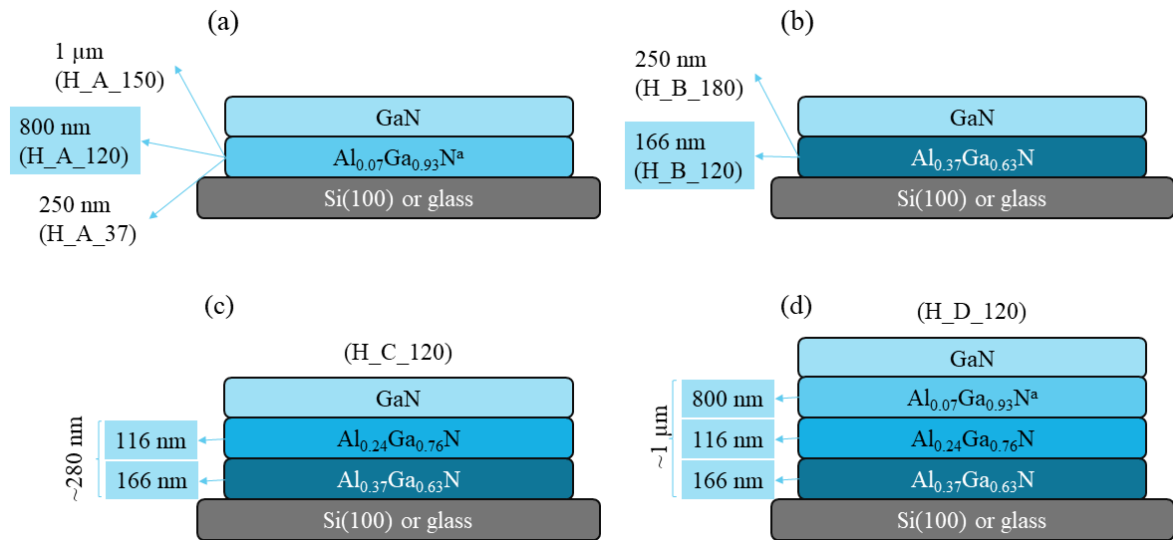


Figure 12: Heterostructures using a) one buffer layer with low Al content, b) one buffer layer rich in Al, c) two buffer layers and d) three buffer layers.

Samples H_A_37 and H_B_180 were produced with the same number of layers (one) and thickness (250 nm) in order to compare the effect of the buffer layer composition. The

effect of the thickness can be observed when comparing samples H_A_150, H_A_120, and H_A_37 for a low-Al one-buffer layer heterostructure, and when comparing samples H_B_180 and H_B_120 for a high-Al one-buffer layer heterostructure. A deposition time of 120 min was used for all the $\text{Al}_x\text{Ga}_{1-x}\text{N}$ samples to maintain the characteristics of the previously analyzed films. Once the heterostructure H_C_120 show a total thickness of ~ 280 nm on the buffer, it could be compared to sample H_B_150 (250 nm on the buffer) in terms of adding a medium composition layer prior to the GaN layer without increasing the thickness. Then, sample H_D_120, with a total thickness of ~ 1 μm on the buffer, could be compared to sample H_A_150 (1 μm), maintaining the thickness and changing the addition of different layers to create a compositional gradient.

The samples were analyzed using XRD, SEM, Raman spectroscopy, and UV-Vis spectrophotometry.

3.5 Profilometry

Profilometry analyses were performed to determine the thickness of the $\text{Al}_x\text{Ga}_{1-x}\text{N}$ films, using an optical profilometer (NanoCalc-VIS by Ocean Optics). These measurements could only be conducted on samples deposited on Si substrates. Therefore, measurements were taken on Si (100) A substrate samples, as they were representative for the other samples since the deposition process was identical for all samples, and thickness and deposition rates should be the similar. For each sample, measurements were taken simulating both a GaN and an AlN layer on top of the Si substrate, and the thickness was determined by averaging the results of both analyses.

3.6 Energy dispersive spectroscopy

Energy dispersive spectroscopy is a technique used to determine the elemental composition of a material by analyzing the energy of X-rays emitted from the sample when it is bombarded with an electron beam. In this case, EDS was used to determine the aluminum content in the $\text{Al}_x\text{Ga}_{1-x}\text{N}$ samples. The analysis was performed using an Oxford X-act instrument attached to a Vega 3 scanning electron microscope. To ensure the accuracy of the

measurements, the analysis was performed at three different points on each sample, and the aluminum content was determined by calculating the arithmetic mean of the measurements.

3.7 X-Ray diffraction crystallography

The XRD characterization study was carried out on a PANalytical Empyrean instrument for all $\text{Al}_x\text{Ga}_{1-x}\text{N}$ samples and the heterostructures. The measurements were performed using a θ - 2θ configuration. All measurements for the $\text{Al}_x\text{Ga}_{1-x}\text{N}$ films were made using a $\frac{1}{2}^\circ$ anti-scatter slit and a 10 mm mask for the incident beam, and a 15.4 mm anti-scatter slit for the diffracted beam, at 40 kV and 40 mA for voltage and current, respectively. The scan speed was $0.01^\circ/\text{s}$. For the heterostructures, the slits, mask, and scan speed were varied to obtain a good signal without exceeding 50k counts on the intensity to prevent equipment damage.

The angle range was adjusted according to the substrate under analyses to avoid the monocrystalline Si peaks. For Si (100) substrates – single or both sides polished –, Si (110), and Si (111), the angle range was 30 to 65° , 30 to 45° , and 30 to 55° , respectively. For the glass substrate, the angle range was 30 to 70° , according to the minimum and maximum expected positions for GaN and AlGaN diffraction peaks.

3.8 UV-Vis spectrophotometry

The $\text{Al}_x\text{Ga}_{1-x}\text{N}$ films and the heterostructures deposited on glass substrates were analyzed using an Evolution 200 Series UV-Vis spectrophotometer by Thermo Fisher Scientific to obtain optical properties such as transmitted radiation, bandgap, refraction index, and thickness.

The thickness obtained for the $\text{Al}_x\text{Ga}_{1-x}\text{N}$ films was compared to the profilometry results to confirm the accuracy and increase confidence in the analyses. The bandgap results were used to infer a relation with the Al content. Static refractive index was compared between samples with different Al content and to expected values.

3.9 Raman spectroscopy

Raman spectroscopy was performed only for the samples on glass substrates, including both the $\text{Al}_x\text{Ga}_{1-x}\text{N}$ films and the heterostructures. All measurements were conducted at room

temperature using a LabRAM HR Evolution confocal Raman microscope (HORIBA). Special care was taken to avoid any damage to both the sample and the equipment during the process.

The samples were analyzed using a 532 nm Nd:YAG solid-state laser as the excitation source and a 100x objective lens. Measurements were made using a 100 % ND filter, 600 gr/mm diffraction grating, and a range of 50 to 1500 cm^{-1} with 3 accumulations under 60s per accumulation. The data was analyzed to determine peak positions and FWHM. The results were then studied in terms of peak shift and broadening.

3.10 Scanning electron microscopy

The samples were analyzed on field emission gun (FEG) SEM with a MIRA 3 Tescan microscope. The samples analyzed were heterostructures deposited on Si substrates with the aim of observe the growth and surface morphology of the films. The instrument was operated at various magnifications to obtain high-resolution images of the samples. Prior to analysis, the samples were prepared by mounting them on a sample holder using conductive carbon tape to ensure proper grounding and by covered with golden for conductivity.

The analysis of the images was carried out by visually inspecting the surface morphology and growth of the films. The images obtained were used to study the grain size, shape, distribution, and any other relevant features of the films. The results obtained from the FEG-SEM analysis were used to understand the growth behavior and quality of the films.

4 Results and discussion

4.1 Initial exploratory study

The $\text{Al}_x\text{Ga}_{1-x}\text{N}$ samples studied initially, as described in Section 3.2, had their composition analyzed to determine the parameters for the definitive samples. The Al content (x) was calculated using three EDS measurements with standard deviation to ensure the precision and accuracy of the results. These results are summarized in Table 5.

Table 5: Al content for the initial $\text{Al}_x\text{Ga}_{1-x}\text{N}$ samples obtained using EDS analyses.

Sample	Al target power (W)	Al content, x	Standard deviation
T_10	10	0.0090	0.0004
T_50	50	0.060	0.002
T_200	200	0.290	0.001

Sample T_10 had a very low Al content in the alloy (less than 1 % in relation to the Ga composition). Sample T_50 (approximately 6 %) showed a good amount of Al for a low Al content, which led to the selection of 50 W as the lower limit for deposition. Sample T_200 was the most Al-rich sample (approximately 29 %). This high Al content, aligned with the specifications for the power supply, led to a selection of 100 W as the upper limit. A value of 75 W (halfway between 50 and 100) was chosen as the medium value.

For the following definitive samples, it was decided to vary the Ga target power, leading to different compositions for the $\text{Al}_x\text{Ga}_{1-x}\text{N}$ samples.

4.2 AlGaN films

4.2.1 AlGaN composition and thickness

The Al content (x) of the $\text{Al}_x\text{Ga}_{1-x}\text{N}$ samples was determined through EDS analyses, and the results are summarized in Table 6. The measurements showed excellent agreement between different substrates (Si or glass), with a difference of less than 0.02.

Table 6: Al content in $\text{Al}_x\text{Ga}_{1-x}\text{N}$ samples with Si and glass substrates measured using EDS.

Sample	Al content, x	
	Si substrate	Glass substrate
S_100_60	0.13	0.14
S_50_60	0.07	0.08
S_75_60	0.11	0.12
S_0_60	0.00	0.00
S_50_30	0.24	0.25
S_100_90	0.09	0.08
S_50_90	0.04	0.04
S_100_30	0.47	0.45
S_75_30	0.38	0.37
S_75_90	0.07	0.07

Some samples obtained with different parameters had equal or similar compositions. Samples S_50_60, S_100_90, and S_75_90 all had close composition values. On glass substrates, the $\text{Al}_x\text{Ga}_{1-x}\text{N}$ samples S_50_60 and S_100_90 had the same composition approximately ($x = 0.08$), while sample S_75_90 had an Al content of $x = 0.07$. For Si substrates, S_50_60 and S_75_90 had the sample composition approximately ($x = 0.07$), while sample S_100_90 had $x = 0.09$.

To clarify the effects of each target on the sample composition, Figure 13 shows the correlation between the measured Al content in the Si substrate samples and the relative power used in the Al target corrected by a factor $\alpha \sim 3$. This factor was obtained from the geometry of the deposition chamber, considering the distance of both targets from the substrate and the angle between them. Figure 13a shows that changes in the RF power create similar behaviors when the DC power is kept fixed. Figure 13b shows a direct relation between the DC power used and the composition, i.e., as the power applied to the Al target increases on the ratio, the Al content increases in the films. However, the different Al and Ga targets influenced the composition differently. Samples with the same ratio showed different composition when the power applied to the targets varied. Samples with a ratio of 0.357 had highly different composition ($x = 0.14$

and $x = 0.25$) while samples with the same ratio of 0.217 had very similar composition ($x = 0.07$ and $x = 0.08$).

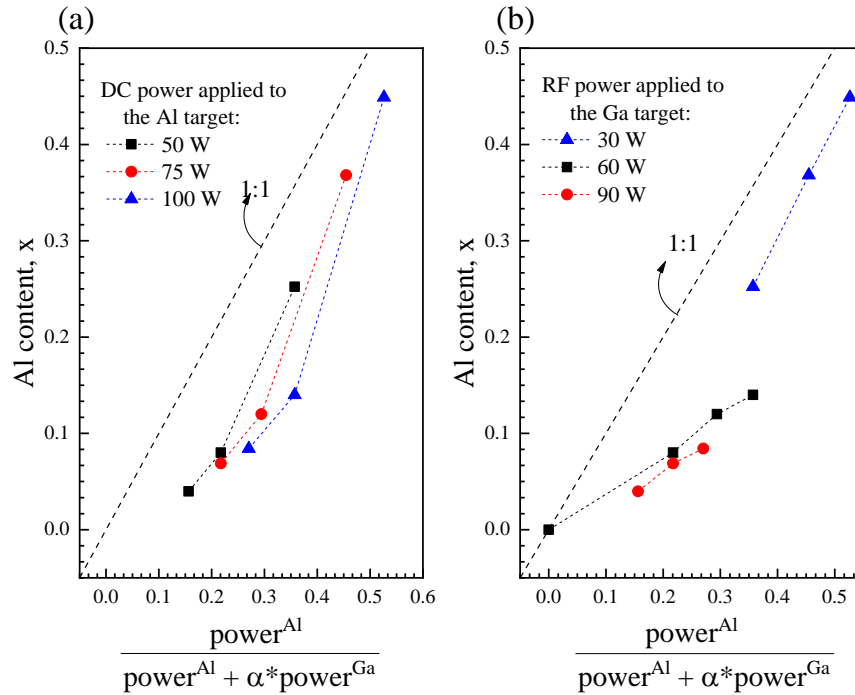


Figure 13: Correlation between the Al content on the $\text{Al}_x\text{Ga}_{1-x}\text{N}/\text{Si}$ samples and the relative power applied to the Al target, highlighting the effects of fixed (a) Al-target DC power and (b) Ga-target RF power.

The Al content is often calculated using the lattice parameters for the samples, assuming Vegard's law (JAMES HOWARD EDGAR, 1999). Therefore, the composition obtained by X-ray diffraction was compared to the EDS results for the glass substrate samples, as shown in Figure 14. Figure 14b shows the relationship between the composition obtained using both methods, and a factor of 1.77 (almost twice the value) was determined between the %Al on XRD to EDS. The implications of such correlation are to assume that there are strains on the $\text{Al}_x\text{Ga}_{1-x}\text{N}$ films, which would lead to an overestimation of Al content using this method. Also, it can help to assume what portion of the peak center shift is related to the composition and what is related to strains on the structure. Therefore, the EDS results are the ones adopted as the correct composition of the films, and they will be used to refer to the samples in the subsequent sections of this work.

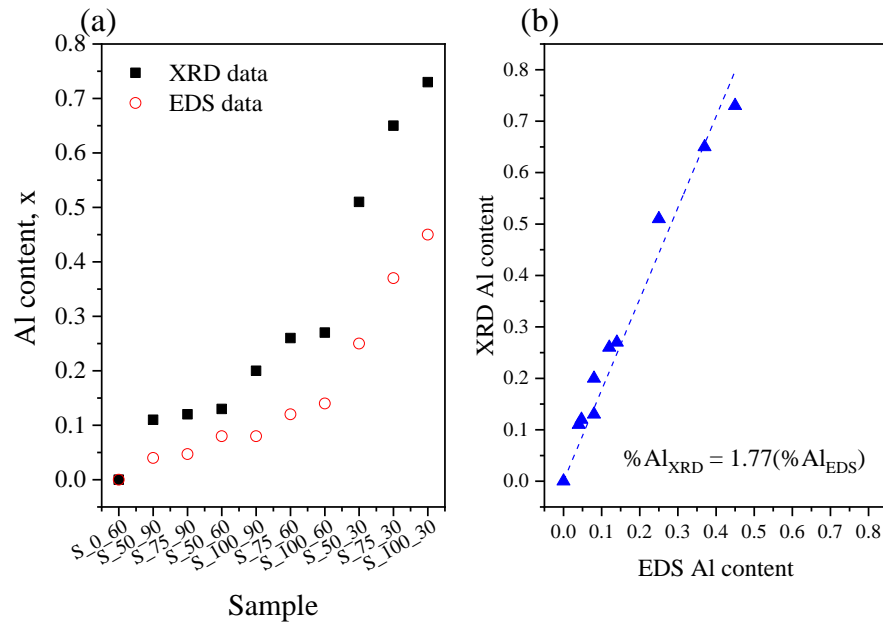


Figure 14: a) Different x values of the $Al_xGa_{1-x}N$ /glass samples calculated using XRD and EDS analyses and b) correlation of the % of Al obtained using EDS and XRD.

The main influence on the thickness and deposition rate was the power applied to the Ga target, followed by the power applied to the Al target. Figure 15 shows the tendency of the deposition rate (and thickness, consequently, since all samples used the same deposition time) with both Ga and the Al target powers. The thickness of the films and the deposition rates calculated using profilometry and UV-Vis are shown on Table 7. For comparison, other studies using sputtering deposition achieved different deposition rates, up to 61.7 nm/min for AlN using unbalanced magnetron reactive sputtering (KE et al., 2015), 2.3 nm/min for AlN using RF reactive sputtering (CHENG et al., 2003), and 77.5 nm/min for AlN using pulsed DC reactive sputtering (TAKEUCHI; OHTSUKA; FUKUYAMA, 2015). This shows that the deposition rate for sputtering processes can vary immensely with different parameters used.

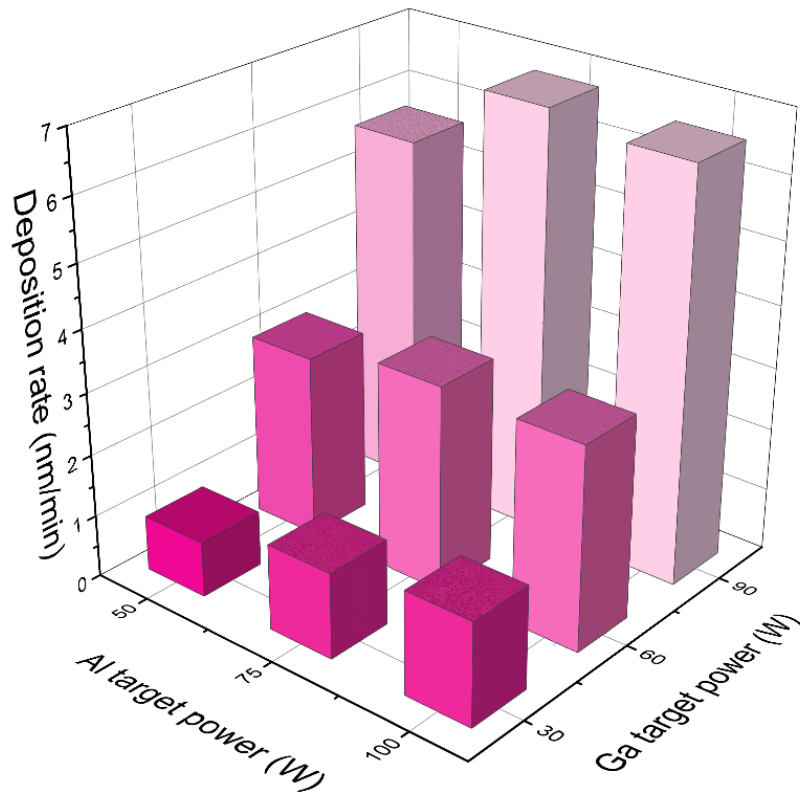


Figure 15: Effects of the power applied to the Al target and the Ga target on the deposition rate of the $\text{Al}_x\text{Ga}_{1-x}\text{N}/\text{Si}$ samples.

Table 7: Thickness measured using profilometry and UV-Vis spectroscopy and the respective deposition rates for the samples produced with different Ga and Al target power. Samples are ordered as they were produced.

Sample	Profilometry (nm)	Deposition rate (nm/min)	UV-Vis (nm)	Deposition rate (nm/min)
S_100_60	407 ± 42	3.4 ± 0.4	382.2 ± 0.2	3.185 ± 0.002
S_50_60	352 ± 36	2.9 ± 0.3	341.2 ± 0.4	2.843 ± 0.003
S_75_60	398 ± 41	3.3 ± 0.3	379.3 ± 0.2	3.161 ± 0.002
S_0_60	253 ± 51	2.1 ± 0.4	254.4 ± 0.3	2.120 ± 0.003
S_50_30	116 ± 14	1.0 ± 0.1	112.7 ± 0.1	0.9392 ± 0.0008
S_100_90	770 ± 77	6.4 ± 0.6	748.6 ± 0.7	6.238 ± 0.006
S_50_90	678 ± 69	5.7 ± 0.6	649.4 ± 0.6	5.412 ± 0.005
S_100_30	193 ± 20	1.6 ± 0.2	196.9 ± 0.1	1.6401 ± 0.0008
S_75_30	166 ± 18	1.4 ± 0.2	164.4 ± 0.1	1.3700 ± 0.0008
S_75_90	805 ± 79	6.7 ± 0.7	784.0 ± 0.6	6.533 ± 0.005

The thicknesses measured using optical profilometry and the ones obtained through UV-Vis calculations were in good agreement, and higher deposition rates were achieved on the samples using 90 W on the Ga target. It is important to note that optical profilometry was used to measure the thickness of the samples on the Si (100) A substrates, whilst the UV-Vis values come from the glass substrate samples. The good agreement between the glass and Si substrate samples for thickness indicates good uniformity of the deposition process, which is related to the rotation of the substrates during the process.

The significant error associated with the optical profilometry-measured thickness results from simulating the R% spectra using GaN or AlN index of refraction, instead of using an intermediary and more appropriated value, which is a limitation of this method for the films with an intermediate composition. The simulations of the UV-Vis T%, on the other hand, take care of estimating the index of refraction of each sample simultaneously with the calculation of the film thickness. Consequently, given the greater accuracy of the UV-Vis T% measurements and analysis and the limited influence of the substrate on thickness and deposition rate, along

with the uniformity of the process, the UV-Vis thickness values will be consistently adopted for all substrates moving forward.

4.2.2 X-Ray diffraction

The X-ray diffractometry results for the $\text{Al}_x\text{Ga}_{1-x}\text{N}$ samples with different substrates are shown and discussed on the following subsections. Due to the large number of samples, studies, and substrates, this section will be divided into different substrates with a review at the end.

4.2.2.1 Glass substrate

The diffractograms for the glass substrate samples can be seen in Figure 16, ordered by Al content. The dashed lines represent the expected peak position for the (0002), (10 $\bar{1}$ 1), (10 $\bar{1}$ 2), and (10 $\bar{1}$ 3) planes of AlGa $_x$ N. The values can range from the expected for GaN to AlN (SCHULZ; THIEMANN, 1977).

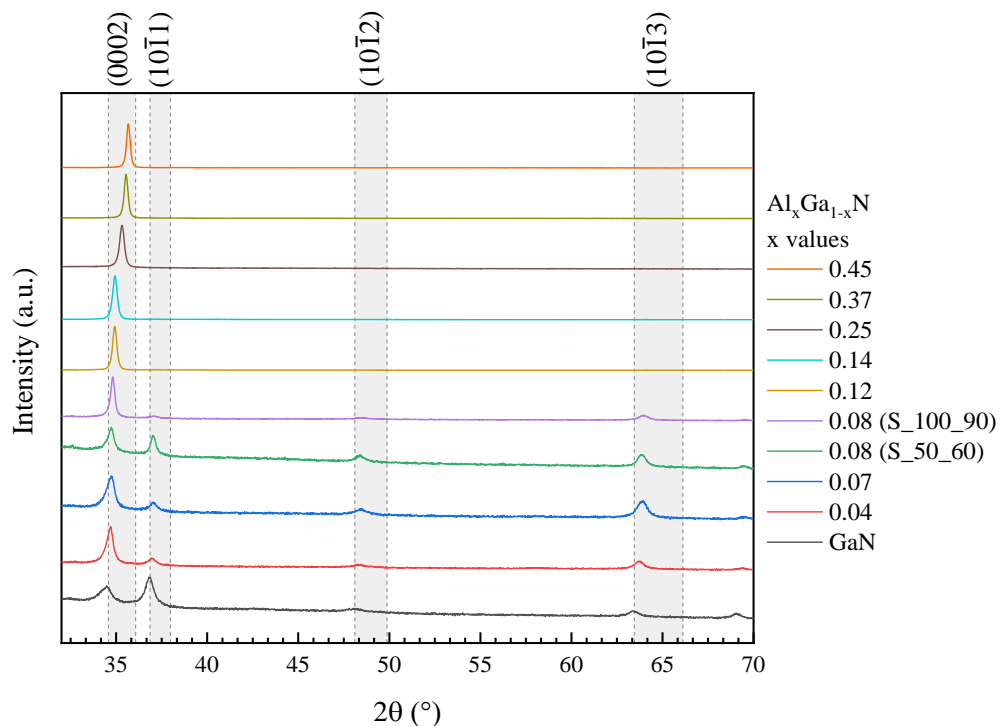


Figure 16: XRD results of the $\text{Al}_x\text{Ga}_{1-x}\text{N}$ samples on glass substrates. Dashed lines indicate the expected position for the $\text{Al}_x\text{Ga}_{1-x}\text{N}$ peaks, that goes from GaN ($x = 0$), in the lower angles, to AlN ($x = 1$), in the higher angles.

From Figure 16, it can be observed that a peak corresponding to the (0002) plane is present in all samples, and its position shifts according to the increase in Al content, as expected. In the samples with lower Al content ($x \leq 0.08$), a second peak related to the (10 $\bar{1}$ 1) plane (expected at 36.86° for GaN) can be seen. As discussed in Section 2.1.1, AlN samples are typically produced using sputtering deposition techniques with high *c*-orientation, which results in a very intense and isolated (0002) peak. The increase in Al content may induce a more oriented growth on the samples, leading to what is observed on the diffractograms. It is also important to note that, although sample S_50_60 (Al_{0.08}Ga_{0.92}N) has a higher Al content than samples S_50_90 (Al_{0.04}Ga_{0.96}N) and S_75_90 (Al_{0.07}Ga_{0.93}N), the latter two showed a more pronounced and relatively high (0002) peak.

The diffractograms were separated according to the Ga target power (30, 60, and 90 W) and are shown in Figure 17. This makes it easier to see the effect of the Al content (or the Al target power) when the other parameters are kept constant. Figure 17 also shows a zoom-in of the (0002) peak region for the diffractograms.

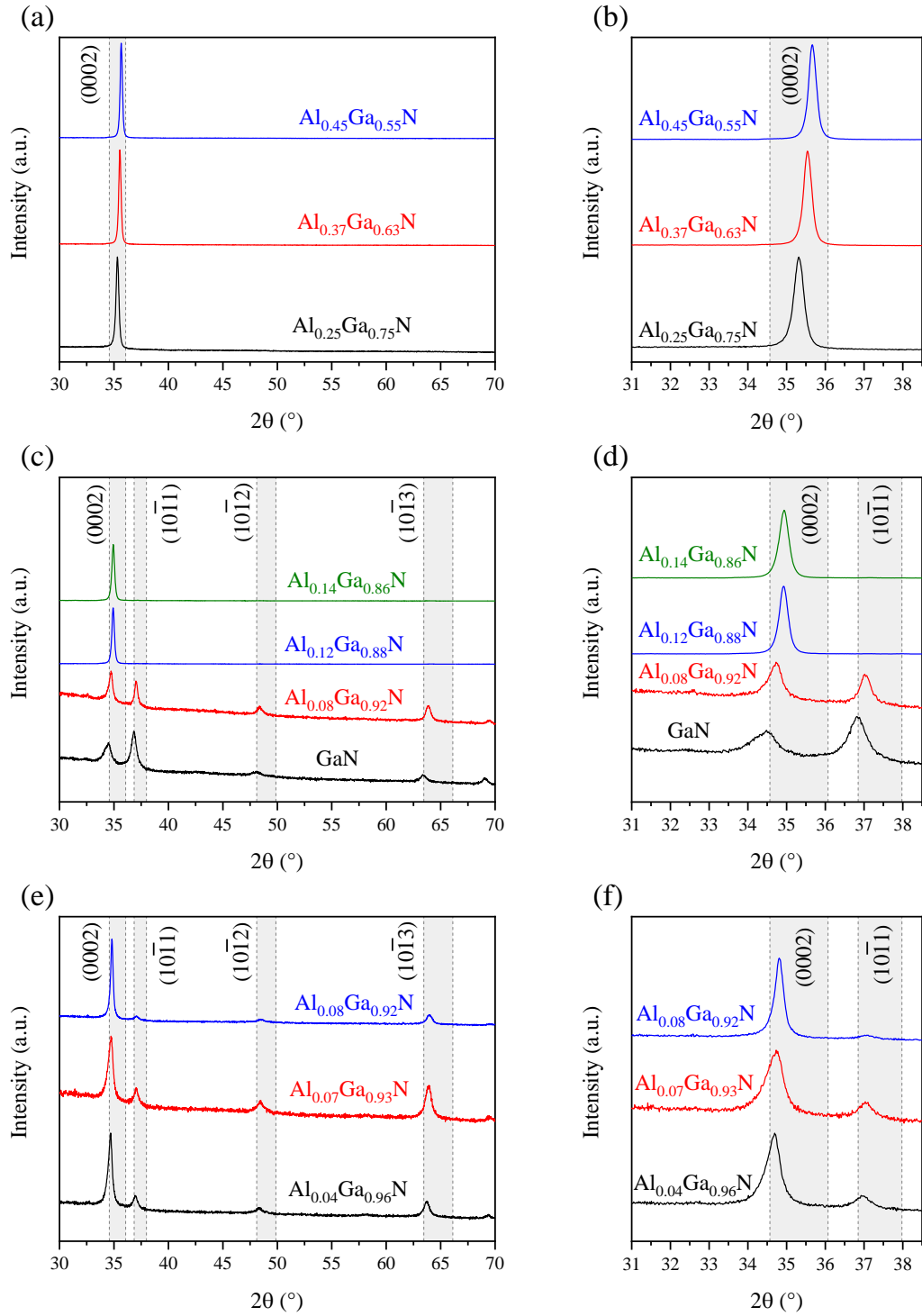


Figure 17: Diffraction patterns of the Al_xGa_{1-x}N samples on glass substrate: (a) using 30 W on the Ga target with (b) a zoom-in of the (0002) region, (c) using 60 W on the Ga target with (d) a

zoom-in of the (0002) region, and (e) using 90 W on the Ga target with (f) a zoom-in of the (0002) region. Dashed lines indicate the expected position for the AlGa_N diffraction peaks.

Once again, it can be concluded that the increase in Al content, which was due to the increase in power applied to the Al target, created more *c*-axis oriented samples, when maintaining the Ga target power fixed. Samples produced using 30 W on the Ga target showed a high preferred crystalline orientation, however, those samples were the ones with more Al content. Nonetheless, the films produced using 60 and 90 W on the Ga target still show a preferred orientation on the *c*-axis, that increases with Al content. This highly preferred crystalline orientation on the *c*-axis for the samples hindered the use of refinements such as Rietveld or Le-Bail. Therefore, the lattice parameters *a* and *c* for the different samples were obtained using Bragg's law for hexagonal structures:

$$d_{(hkl)} = \frac{\lambda}{2\sin\theta} \quad \text{Equation 7}$$

$$\frac{1}{d_{(hkl)}^2} = \frac{4}{3} \left(\frac{h^2+hk+k^2}{a^2} \right) + \frac{1}{c^2} \quad \text{Equation 8}$$

where *d* is the interplanar spacing for the plane with Miller indexes (*hkl*), λ is the wavelength of the incident radiation, and θ is the angle for the (*hkl*) plane.

The interplanar spacing *d* can be calculated using the angle θ from the XRD analyses. By using (*hkl*) as (002), the lattice parameter *c* was obtained by:

$$c = 2d_{(002)} \quad \text{Equation 9}$$

And by using (*hkl*) as (101), the lattice parameter *a* was obtained by:

$$\frac{1}{a^2} = \frac{3}{4} \left(\frac{1}{d_{(101)}^2} - \frac{1}{c^2} \right) \quad \text{Equation 10}$$

Crystallite size D was estimated following Scherrer equation:

$$D = \frac{K\lambda}{\beta \cos \theta} \quad \text{Equation 11}$$

where K is a constant (shape factor), and β is the FWHM of the peak.

The lattice parameters a and c are shown in Figure 18. The lack of the $(10\bar{1}1)$ peak or any other that could help obtain the lattice parameter without high uncertainty for samples with $x \geq 0.12$ prevented the calculation of the lattice parameter a .

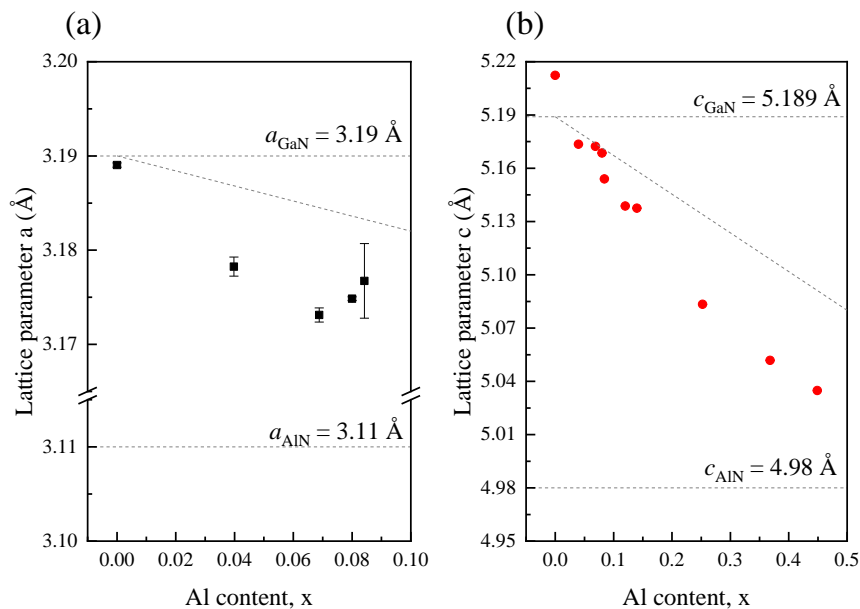


Figure 18: Lattice parameters (a) a and (b) c of the $\text{Al}_x\text{Ga}_{1-x}\text{N}$ samples on glass substrates. The expected values for the unstrained GaN and AlN lattice parameters are indicated, as well as their linear relation. The error bar is not visible because it is smaller than the dots in the graph.

The lattice parameters for unstrained GaN and AlN are marked as dashed lines, with values of 3.11 and 3.19 Å for the lattice parameter a for AlN and GaN, respectively, and 4.98 and 5.189 Å for the lattice parameter c for AlN and GaN, respectively (SCHULZ; THIEMANN, 1977). A decrease in a and c can be seen as the Al content increases, which is the expected behavior. Some studies show this to occur linearly, but this behavior is somewhat disturbed by

the strains and defects on the films (BERNARDINI; FIORENTINI, 2001; KORAKAKIS et al., 1996; NOVIKOV et al., 2015).

Sample S_0_60 (GaN), with no Al content, shows a c parameter above the expected value for unstrained GaN. This is indicative of tensile strain on the film, causing the lattice parameter to expand, and will be discussed in detail further on. The calculated crystallite size (from Equation 11) is shown in Table 8, and it is related to the (0002) peak position and FWHM, which are shown in Figure 19.

Table 8: Crystallite size of the $\text{Al}_x\text{Ga}_{1-x}\text{N}$ /glass samples.

Sample	Al content, x	Crystallite size (\AA)
S_0_60	0	112.8 ± 1.5
S_50_90	0.04	211.2 ± 2.8
S_75_90	0.07	161.4 ± 1.7
S_50_60	0.08	226.1 ± 2.9
S_100_90	0.08	314.2 ± 2.8
S_75_60	0.12	304.1 ± 0.9
S_100_60	0.14	277.4 ± 0.8
S_50_30	0.25	271.8 ± 1.0
S_75_30	0.37	329.7 ± 0.9
S_100_30	0.45	346.2 ± 0.8

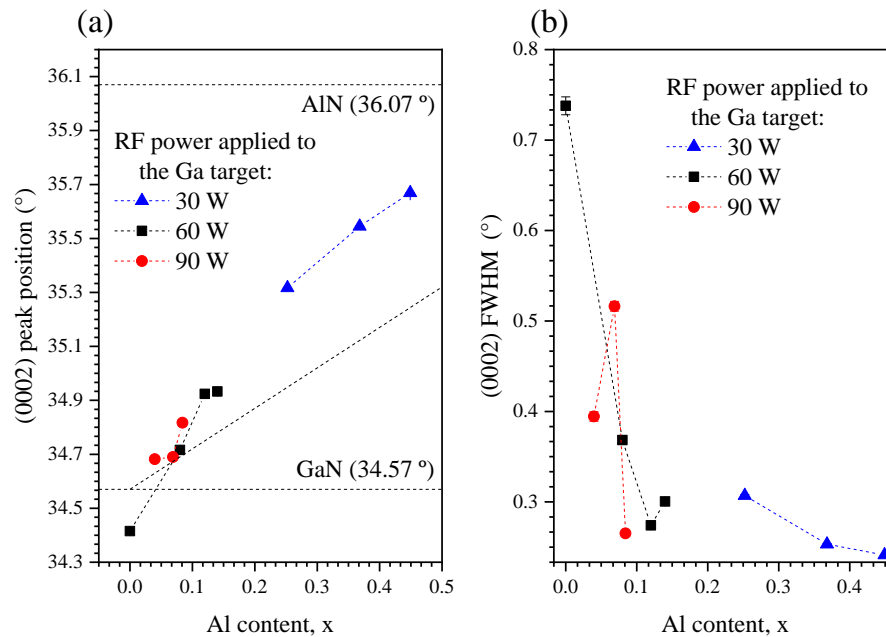


Figure 19: (a) Peak position and (b) FWHM related to the (0002) plane of the $\text{Al}_x\text{Ga}_{1-x}\text{N}$ samples on glass substrate. The expected (0002) peak position for unstrained GaN and AlN are indicated, as well as their linear relation. The error bar is not visible because it is smaller than the dots in the graph.

The increase in the peak position is expected due to the increase in the Al content, with a deviation from the linear behavior due to strains on the films. The FWHM, however can be an indicative of the film's general quality. The GaN sample, and the samples with low Al content ($x < 0.08$) have large FWHM values, which could indicate low crystalline quality. A relationship between the (0002) peak FWHM and the Al content has been established, revealing that with increasing Al content, the FWHM tends to decrease, showing an improvement in the quality of the samples. This observation underscores the significant role played by Al content in enhancing the crystalline quality of $\text{Al}_x\text{Ga}_{1-x}\text{N}$ films on glass substrates. Notably, the substantial FWHM contrast between the GaN ($x = 0$) sample and the Al-rich samples (reducing from 0.74 to 0.25) underscores this improvement. However, given that thin film thickness has been shown to influence FWHM (DUQUENNE et al., 2008; LEE; JOO; KIM, 2014; RODRÍGUEZ-MADRID et al., 2012; SEON et al., 2000; SUN et al., 2016), Figure 20 provides a correlation that illustrates the variation of (0002) FWHM in relation to the thickness of $\text{Al}_x\text{Ga}_{1-x}\text{N}$ samples on glass substrate.

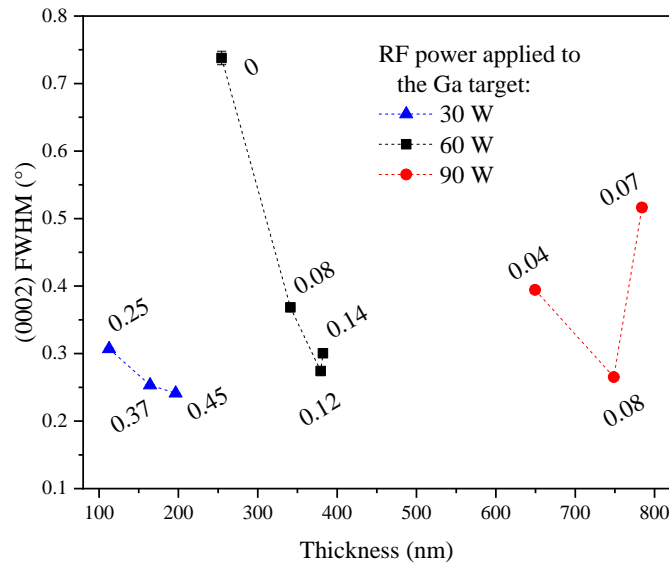


Figure 20: (0002) FWHM related to the thickness of the $\text{Al}_x\text{Ga}_{1-x}\text{N}$ films for glass substrates. The x values of the composition of the films are indicated as the label of each point.

Comparing Figure 19b and Figure 20, it becomes evident that the thickness of the films has no direct or clear influence on the FWHM of the $\text{Al}_x\text{Ga}_{1-x}\text{N}$ films deposited on glass substrates when varying the Al content. In these instances, the composition of the films exhibits a much stronger influence on the crystalline quality. This highlights that the relationship between FWHM and Al content is the predominant factor in determining the crystalline quality of the films. Further analysis of these results can provide a better understanding for optimizing the deposition process for enhanced crystalline quality.

The out-of-plane strain (ε_{zz}) and in-plane strain (ε_{xx}) values in the films were estimated using the following equations (JAYASAKTHI et al., 2014):

$$\varepsilon_{zz} = \frac{c - c_0}{c_0} \quad \text{Equation 12}$$

$$\varepsilon_{xx} = \frac{a - a_0}{a_0} \quad \text{Equation 13}$$

where a and c are the lattice parameters of the $\text{Al}_x\text{Ga}_{1-x}\text{N}$ films, experimentally obtained by XRD measurements, and a_0 and c_0 are the unstrained expected lattice parameters for the film according to the composition.

The values for a_0 and c_0 were based on the discussion from Section 4.2, considering the composition obtained by EDS and assuming a linear behavior for the AlGa_xN lattice parameters with the increase in Al content (from GaN to AlN values). Vegard's law, which relates the lattice parameter and the peak shift, was used to determine the expected peak position ($2\theta_{\text{sample}}$) for a theoretical unstrained sample with the same composition as obtained by EDS:

$$\text{Al molar fraction (x)} = \frac{\Delta\theta}{\Delta\theta_0} \quad \text{Equation 14}$$

where $\Delta\theta$ is the expected shift for the Al_xGa_{1-x}N sample from the GaN peak ($2\theta_{\text{sample}} - 2\theta_{\text{GaN}}$), and $\Delta\theta_0$ is the difference between the GaN peak and the AlN peak, which is 1.5° for the (0002) peak and 1.12° for the (10 $\bar{1}$ 1) peak (SCHULZ; THIEMANN, 1977).

After obtaining the expected 2θ for the Al_xGa_{1-x}N sample, the lattice parameters a and c were calculated as before (using Equation 8). Once a_0 and c_0 were determined, the out-of-plane and in-plane strains were calculated using Equation 12 and Equation 13, respectively. The results for each sample are shown in Table 9, and the associated uncertainties were also calculated.

Table 9: In-plane and out-of-plane strains of the Al_xGa_{1-x}N/glass samples.

Sample	Al content, x	ϵ_{xx} (%)	ϵ_{zz} (%)
S_0_60	0	-0.03 ± 0.01	0.45 ± 0.01
S_50_90	0.04	-0.27 ± 0.03	-0.15 ± 0.01
S_75_90	0.07	-0.36 ± 0.02	-0.05 ± 0.01
S_50_60	0.08	-0.28 ± 0.01	-0.07 ± 0.01
S_100_90	0.08	-0.21 ± 0.12	-0.34 ± 0.01
S_75_60	0.12	-	-0.48 ± 0.01
S_100_60	0.14	-	-0.42 ± 0.01
S_50_30	0.25	-	-1.01 ± 0.02
S_75_30	0.37	-	-1.15 ± 0.01
S_100_30	0.45	-	-1.15 ± 0.01

Samples with more than 12 % of Al could not have their ϵ_{xx} calculated since the lattice parameter a could not be obtained for these samples, as previously stated. Except for sample S_0_60 (GaN), all samples showed compressive strains for both ϵ_{xx} and ϵ_{zz} . The values are similar to or smaller than those of MOCVD $\text{Al}_x\text{Ga}_{1-x}\text{N}$ samples grown on sapphire substrates (FENG et al., 2019; JAYASAKTHI et al., 2014). There is also a general increase in strain with an increase in the Al content, with sample S_100_30 ($\text{Al}_{0.45}\text{Ga}_{0.55}\text{N}$) showing a value of $(-1.1549 \pm 0.0065) \%$.

4.2.2.2 Si (100) substrates

There are two different Si (100) substrates used in this study: one side polished – named as Si (100) A – and two sides polished – named as Si (100) B. The diffractograms for the $\text{Al}_x\text{Ga}_{1-x}\text{N}$ samples on substrates Si (100) A and B are shown on Figure 21 and Figure 22, respectively.

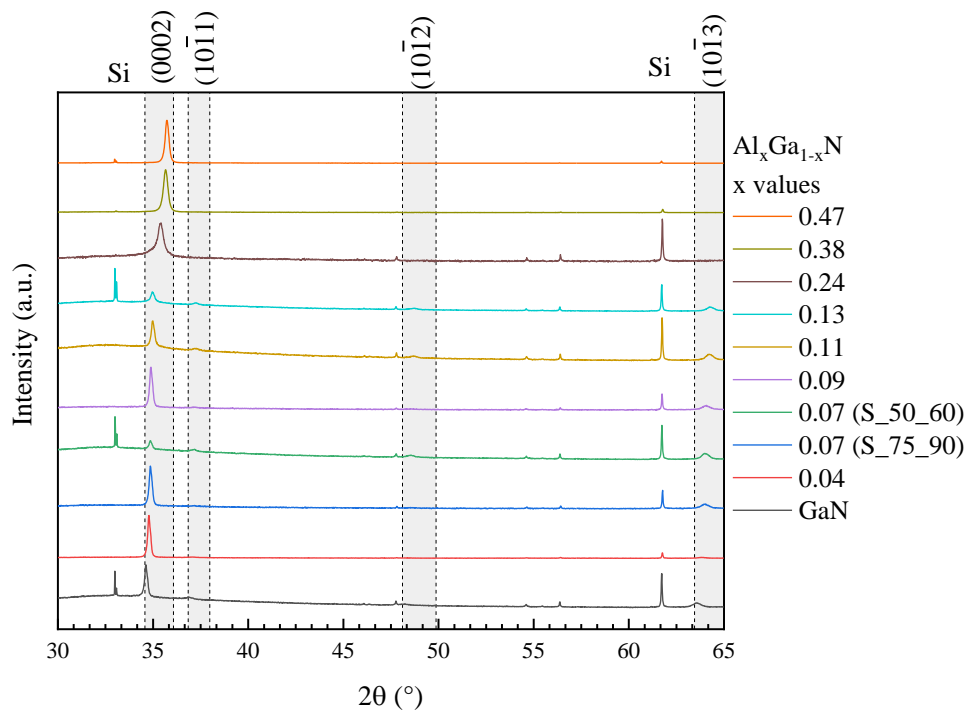


Figure 21: XRD results of the $\text{Al}_x\text{Ga}_{1-x}\text{N}$ samples on Si (100) A substrates. Dashed lines indicate the expected position for the $\text{Al}_x\text{Ga}_{1-x}\text{N}$ peaks, that goes from GaN ($x = 0$), in the lower angles, to AlN ($x = 1$), in the higher angles.

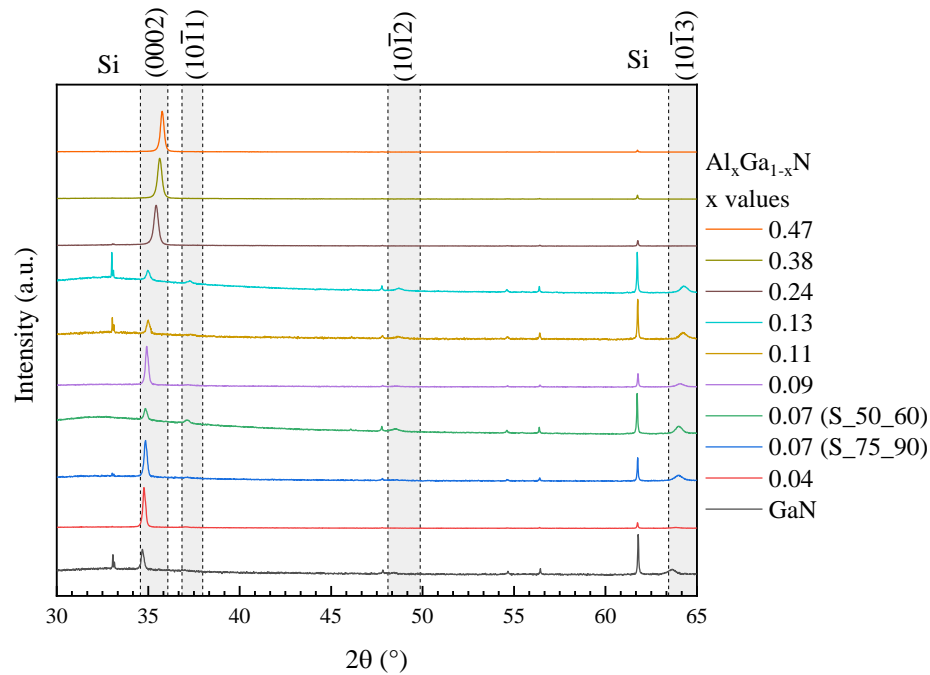


Figure 22: XRD results of the $\text{Al}_x\text{Ga}_{1-x}\text{N}$ samples on Si (100) A substrates. Dashed lines indicate the expected position for the $\text{Al}_x\text{Ga}_{1-x}\text{N}$ peaks, that goes from GaN ($x = 0$), in the lower angles, to AlN ($x = 1$), in the higher angles.

The same as the glass substrate samples, an increase in the Al content creates more pronounced and isolated (0002) peaks for samples on both Si (100) substrates, especially in the samples with high Al content. Again, this indicates an increase in c -axis orientation. The samples produced using 60 W on the Ga target (GaN, $\text{Al}_{0.07}\text{Ga}_{0.93}\text{N}$, $\text{Al}_{0.11}\text{Ga}_{0.89}\text{N}$ and $\text{Al}_{0.13}\text{Ga}_{0.87}\text{N}$) showed low quality, even compared to the samples with less Al content. However, the thicknesses of these samples are much lower than the ones produced using 90 W on the Ga target ($\text{Al}_{0.04}\text{Ga}_{0.96}\text{N}$, $\text{Al}_{0.07}\text{Ga}_{0.93}\text{N}$ and $\text{Al}_{0.09}\text{Ga}_{0.91}\text{N}$). In this sense, the general crystalline quality and the c -axis orientation could be linked to either the composition of the samples (Al content) or the thickness.

Figure 23 and Figure 24 show the diffractograms for the AlGa_xN films on Si (100) A and Si (100) B, respectively, separated by the power applied to the Ga target. This facilitates the understanding of the effect of the Al-target power on the samples, once all other parameters are fixed. It also highlights again that the composition (Al content) is an important factor influencing the c -axis preferred orientation of the films.

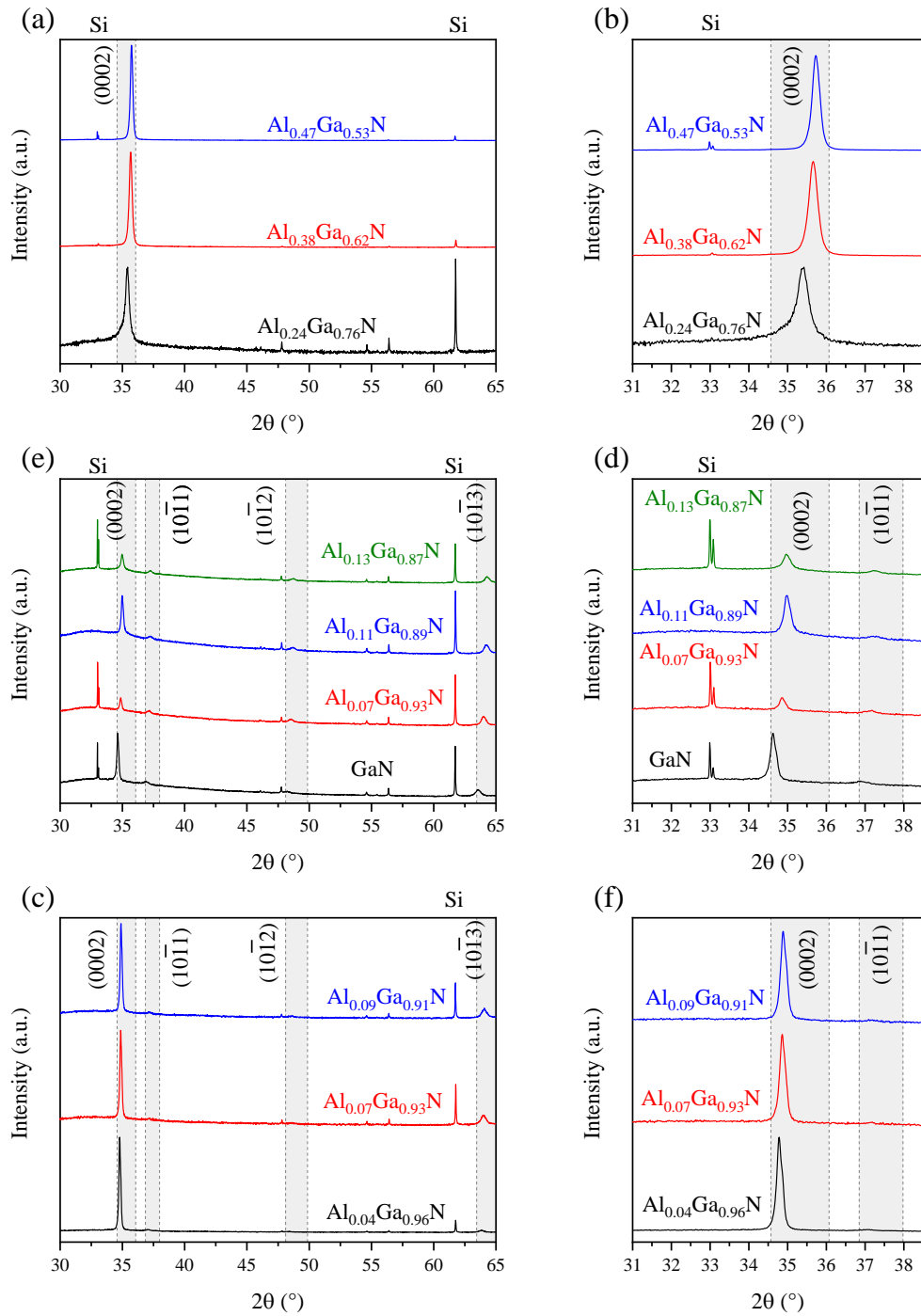


Figure 23: Diffractograms of the Al_xGa_{1-x}N samples on Si (100) A substrate: (a) using 30 W on the Ga target with (b) a zoom-in of the (0002) region, (c) using 60 W on the Ga target with (d) a zoom-in of the (0002) region, and (e) using 90 W on the Ga target with (f) a zoom-in of the (0002) region. Dashed lines indicate the expected position for the AlGaIn diffraction peaks.

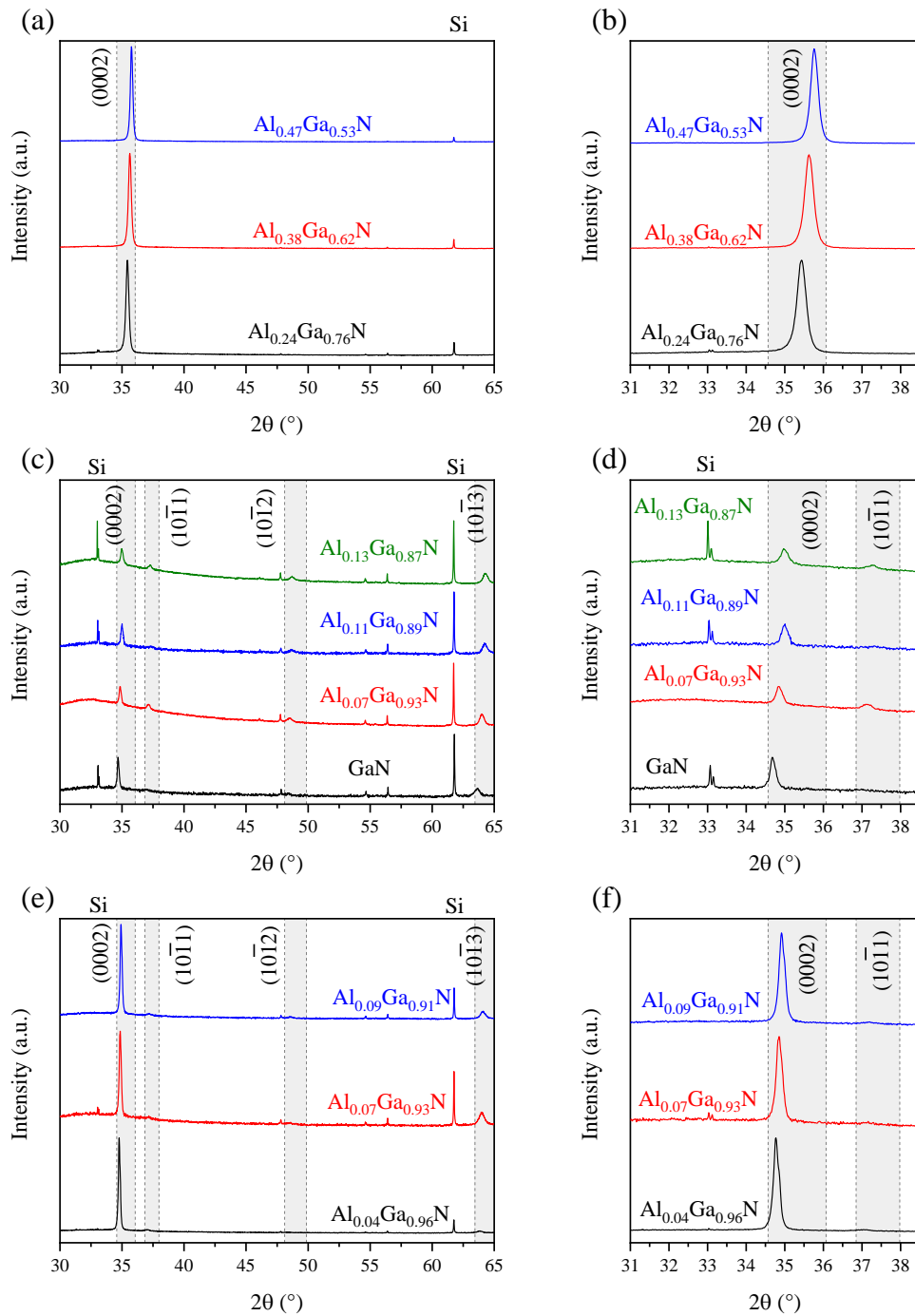


Figure 24: Diffractograms of the Al_xGa_{1-x}N samples on Si (100) A substrate: (a) using 30 W on the Ga target with (b) a zoom-in of the (0002) region, (c) using 60 W on the Ga target with (d) a zoom-in of the (0002) region, and (e) using 90 W on the Ga target with (f) a zoom-in of the (0002) region. Dashed lines indicate the expected position for the AlGa_xN diffraction peaks.

The (10 $\bar{1}$ 1) related peak can still be seen in some of the samples, and is used to calculate the lattice parameter a . It is important to note that some diffractograms show sharp, high intensity, double peaks (here, usually seen at $\sim 31^\circ$ and 61.7°): those are from the Si substrate, that can appear due to the small thickness of the samples and the high penetration of the X-ray. They are also present on some of the samples using the other Si orientation substrates and will be seen further. The lattice parameters a and c were calculated using Equation 7 to Equation 10 for the Si (100) A and Si (100) B substrates samples and are shown in Figure 25 and Figure 26, respectively.

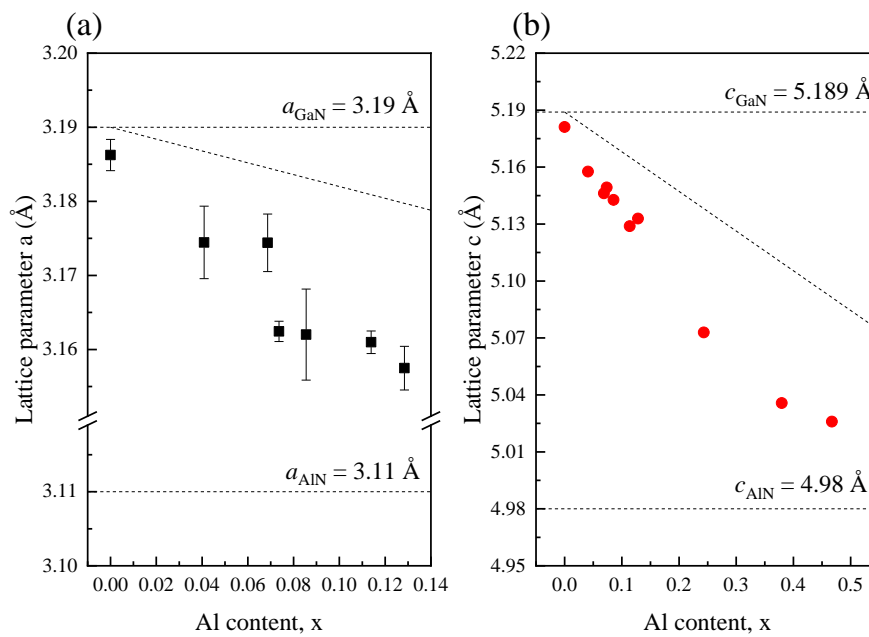


Figure 25: Lattice parameters (a) a and (b) c of the $\text{Al}_x\text{Ga}_{1-x}\text{N}$ samples on Si (100) A substrates. The expected values for the unstrained GaN and AlN lattice parameters are indicated, as well as their linear relation. The error bar is not visible because it is smaller than the dots in the graph.

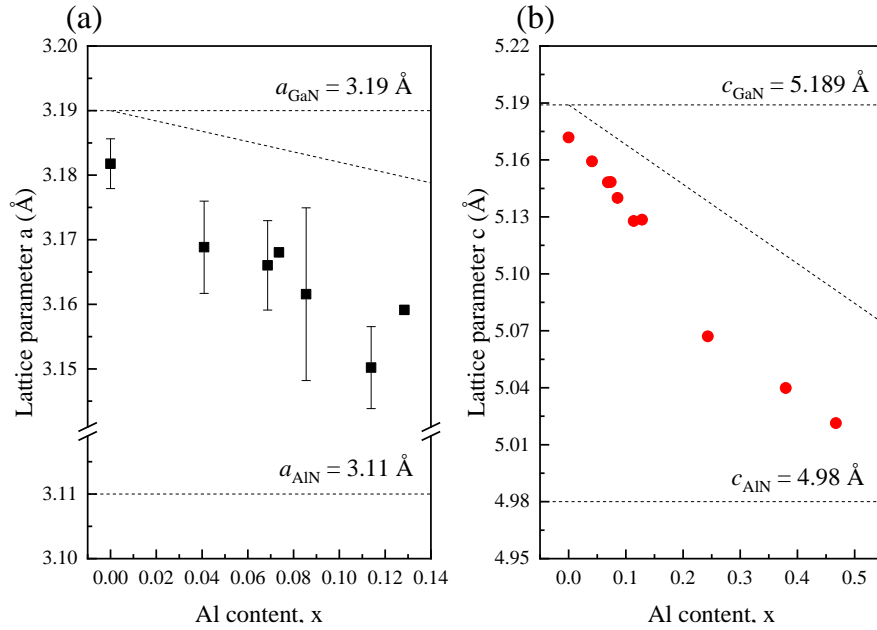


Figure 26: Lattice parameters (a) a and (b) c of $\text{Al}_x\text{Ga}_{1-x}\text{N}$ samples on Si (100) B substrates. The expected values for the unstrained GaN and AlN lattice parameters are indicated as well as their linear relation. The error bar is not visible because it is smaller than the dots in the graph.

The lattice parameters decrease with increasing Al content for the samples, and both Si (100) substrates showed very similar behavior, which is expected, as the lattice parameters (and the associated strains) should be directly related to the mismatch between the substrate and the film. The lack of lattice parameter a for the samples with high Al content is due to the absence of the $(10\bar{1}1)$ peak on the diffractograms, or other peaks that could allow the calculation. The high associated error bars on some of the values are also due to the high relative intensity for the (0002) peak and high c -axis orientation, which leads to low intensity and difficult to fit $(10\bar{1}1)$ peaks, whose errors propagate to the calculated lattice parameter a .

The crystallite size of the samples is shown in Table 10, which is calculated based on the FWHM and peak position using Equation 11. The results are shown in Figure 27 for the Si (100) A substrate and Figure 28 for the Si (100) B substrate.

Table 10: Crystallite size of the $\text{Al}_x\text{Ga}_{1-x}\text{N}/\text{Si}$ (100) samples

Sample	Al content, x	Si (100) A crystallite size (\AA)	Si (100) B crystallite size (\AA)
S_0_60	0	452.3 ± 4.5	478.0 ± 8.8
S_50_90	0.04	459.0 ± 2.7	460.0 ± 3.4
S_75_90	0.07	436.8 ± 2.6	427.9 ± 2.7
S_50_60	0.07	444.9 ± 17.6	418.0 ± 5.9
S_100_90	0.09	441.3 ± 2.6	435.5 ± 4.2
S_75_60	0.11	409.5 ± 3.2	408.4 ± 13.4
S_100_60	0.13	359.5 ± 26.8	363.6 ± 7.3
S_50_30	0.24	241.2 ± 2.8	295.4 ± 1.0
S_75_30	0.38	298.4 ± 0.9	300.1 ± 0.8
S_100_30	0.47	355.7 ± 1.1	355.6 ± 0.9

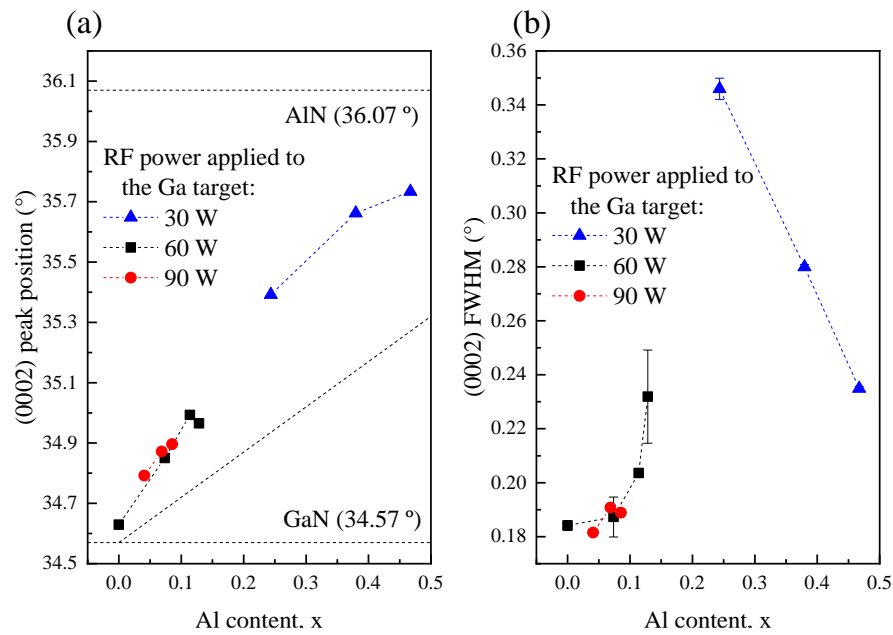


Figure 27: (a) Peak position and (b) FWHM related to the (0002) plane of the $\text{Al}_x\text{Ga}_{1-x}\text{N}$ samples on Si (100) A substrate. The expected (0002) peak positions for unstrained GaN and AlN are indicated, as well as their linear relation. The error bar is not visible because it is smaller than the dots in the graph.

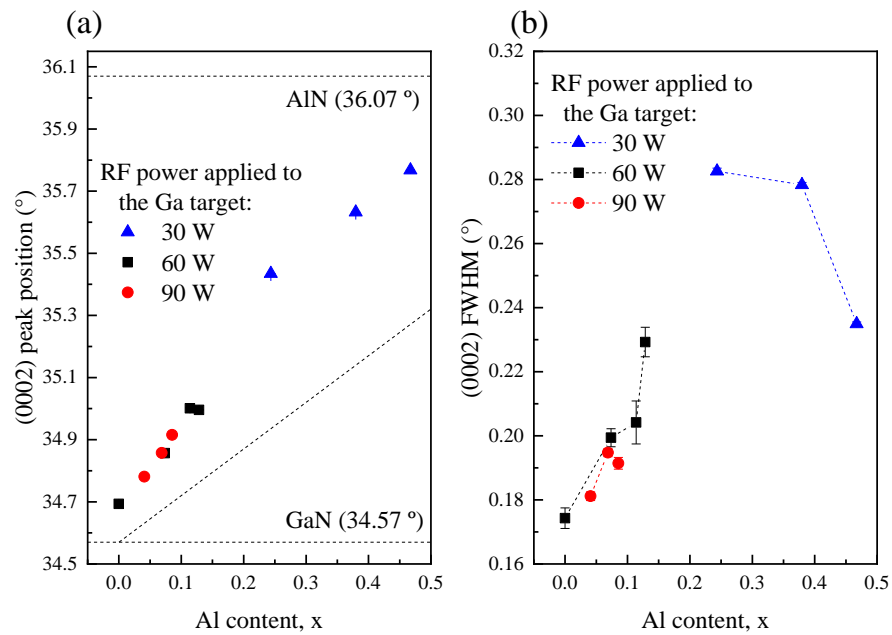


Figure 28: (a) Peak position and (b) FWHM related to the (0002) plane of the $\text{Al}_x\text{Ga}_{1-x}\text{N}$ samples on Si (100) B substrate. The expected (0002) peak positions for unstrained GaN and AlN are indicated, as well as their linear relation. The error bar is not visible because it is smaller than the dots in the graph.

The crystallite sizes show good agreement for most of the samples on the two Si (100) substrates. However, some samples, especially samples S_50_30 ($\text{Al}_{0.24}\text{Ga}_{0.76}\text{N}$) and S_0_60 (GaN), show very distinct values, even considering the associated errors. There are also samples that showed high errors in the calculations, which are derived from FWHM and peak position fitting.

The (0002) peak position and its FWHM exhibit the same behavior for samples on both Si (100) substrates. As discussed previously, there is a shift in the peak position with increasing Al content, and both substrates show a shift from the expected unstrained value, as can be clearly seen for the GaN sample.

Differently than what was observed for the glass substrates, the FWHM shows an increase with Al content, with a slight decrease for the more Al-rich samples. In the glass substrates, the Al content appeared as the main influence in the FWHM. However, looking at the Si(100) substrate samples, a different factor may be influencing these values. With this, in Figure 29 the samples were organized by their thickness in order to verify the relation

supplement by several authors and discussed in Section 2.1.1 (DUQUENNE et al., 2008; LEE; JOO; KIM, 2014; RODRÍGUEZ-MADRID et al., 2012; SEON et al., 2000; SUN et al., 2016).

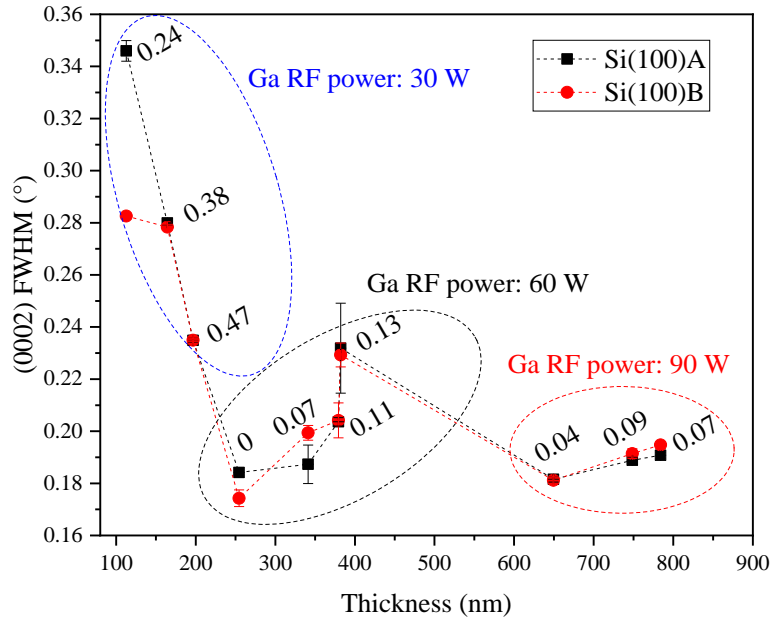


Figure 29: (0002) FWHM related to the thickness of the $\text{Al}_x\text{Ga}_{1-x}\text{N}$ films for the two Si(100) substrates. The x values of the composition of the films are indicated as the label of each point.

Comparing the relations in Figure 27b and Figure 28b with Figure 29, it becomes evident that, differently from what was observed in the glass substrates, the FWHM of the (0002) peak is strongly related to the thickness of the $\text{Al}_x\text{Ga}_{1-x}\text{N}$ films, along with to the Al content. The good agreement between the two Si(100) substrates also shows a good reproducibility of the process and the reliability of the results.

The lower thickness films ($x = 0.25, 0.38,$ and 0.47) display higher FWHM values due to the growth mechanism of the films. In the initial stages of film growth, small and random crystals tend to form before transitioning to more columnar and aligned grains. Consequently, these films did not attain sufficient growth to yield larger crystallites, owing to the low discharge power utilized on the deposition. Beyond a certain thickness ($h > 250$ nm), the influence of thickness becomes less pronounced and the FWHM appears to be more closely linked with the Al content of the films, as demonstrated in Figure 28b. Within this range of

thickness, except for sample S_100_60 ($x = 0.13$), which exhibited an FWHM of 0.23° , all samples exhibited comparable FWHM values ($\sim 0.19^\circ$).

The increase in FWHM with Al content for the samples produced using 60 W on the Ga power source, showing a similar thickness ($0 < x < 0.14$ and $250 \text{ nm} < h < 400 \text{ nm}$), is evident in Figure 29. Thus, the higher FWHM observed for sample S_100_60 could be attributed to this heightened Al content or the increase in the DC power applied to the Al target.

The lattice parameters shown in Figure 25 and Figure 26 diverge from the expected unstrained values, which were obtained based on Equation 14 using Equation 8. The in-plane and out-of-plane strains were calculated for the $\text{Al}_x\text{Ga}_{1-x}\text{N}/\text{Si}$ (100) samples and are shown in Table 11.

Table 11: In-plane and out-of-plane strains of the $\text{Al}_x\text{Ga}_{1-x}\text{N}/\text{Si}$ (100) samples

Sample	Al content, x	Si (100) A ϵ_{xx} (%)	Si (100) A ϵ_{zz} (%)	Si (100) B ϵ_{xx} (%)	Si (100) B ϵ_{zz} (%)
S_0_60	0	-0.12 ± 0.07	-0.15 ± 0.01	-0.26 ± 0.12	-0.33 ± 0.01
S_50_90	0.04	-0.39 ± 0.15	-0.45 ± 0.01	-0.57 ± 0.22	-0.42 ± 0.01
S_75_90	0.07	-0.32 ± 0.12	-0.55 ± 0.01	-0.58 ± 0.22	-0.51 ± 0.01
S_50_60	0.07	-0.68 ± 0.04	-0.47 ± 0.01	-0.51 ± 0.02	-0.49 ± 0.01
S_100_90	0.09	-0.67 ± 0.19	-0.55 ± 0.01	-0.68 ± 0.42	-0.60 ± 0.01
S_75_60	0.11	-0.63 ± 0.05	-0.70 ± 0.01	-0.96 ± 0.20	-0.72 ± 0.01
S_100_60	0.14	-0.70 ± 0.09	-0.56 ± 0.02	-0.65 ± 0.02	-0.65 ± 0.01
S_50_30	0.24	-	-1.25 ± 0.01	-	-1.36 ± 0.01
S_75_30	0.38	-	-1.42 ± 0.01	-	-1.34 ± 0.01
S_100_30	0.47	-	-1.25 ± 0.01	-	-1.34 ± 0.01

The values for in-plane and out-of-plane strains become higher in magnitude (more compressive) as the Al content increases. This behavior is similar to what was observed for the glass substrates and reference (FENG et al., 2019) and is also the same between the two Si (100) substrates. Although most samples show very similar values of strains for the single-side polished and double-sides polished substrates, some samples show high distinction and/or high

associated errors. Due to the high influence of sample thickness, heterogeneity and the fitting process, this strain analyses should be taken into consideration as a quality measurement rather than a quantity measurement. The lack of ϵ_{xx} for the more Al-rich samples is due to the lack of lattice parameter a determination for them.

4.2.2.3 Si (110) substrates

The diffractogram for the samples on Si (110) are shown in Figure 30. The dashed lines are located at the expected position of the (0002) peak for unstrained GaN and AlN, which are at 34.57° and 36.04° , respectively.

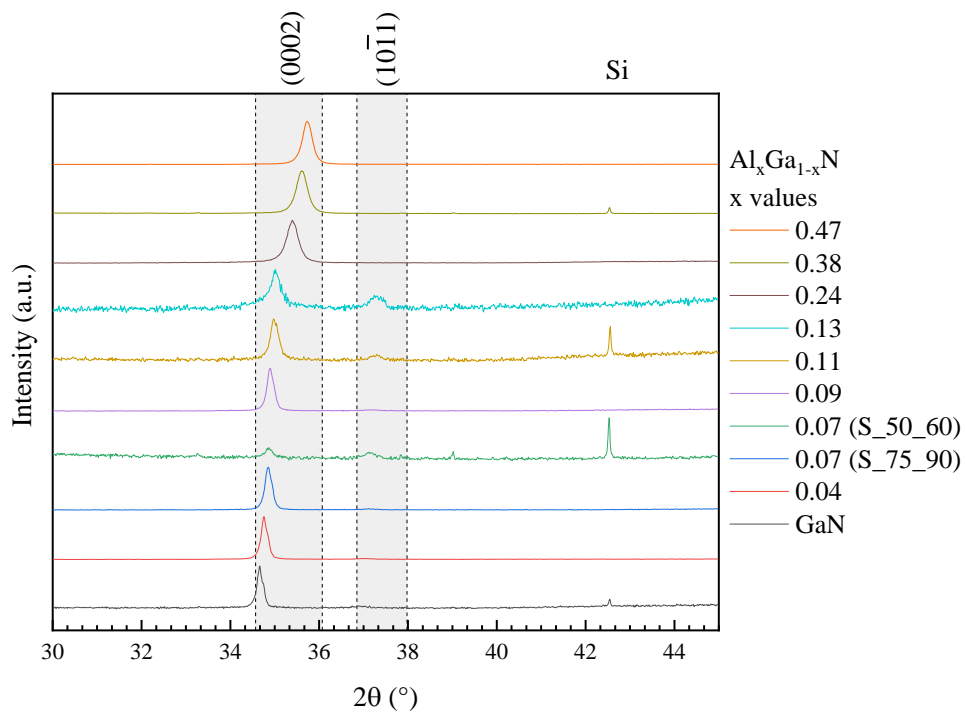


Figure 30: XRD results of the $\text{Al}_x\text{Ga}_{1-x}\text{N}$ samples on Si (110) substrates. Dashed lines indicate the expected position for the $\text{Al}_x\text{Ga}_{1-x}\text{N}$ peaks, that goes from GaN ($x = 0$), in the lower angles, to AlN ($x = 1$), in the higher angles.

From a first glance, the diffractograms could indicate that the samples produced using 60 W on the Ga target (GaN, $\text{Al}_{0.07}\text{Ga}_{0.93}\text{N}$, $\text{Al}_{0.11}\text{Ga}_{0.89}\text{N}$, and $\text{Al}_{0.13}\text{Ga}_{0.87}\text{N}$) had low quality and crystallinity, while the others had a pronounced and isolated (0002) peak, indicating c -axis preferred orientation. This behavior does not seem to be connected to the composition, as

samples with low Al content ($x = 0.04$ and 0.07) also showed good quality. However, those samples were deposited using 90 W on the Ga target. A way to support this is to observe both samples S_100_90 ($\text{Al}_{0.09}\text{Ga}_{0.91}\text{N}$) and S_75_90 ($\text{Al}_{0.07}\text{Ga}_{0.93}\text{N}$), which had similar composition or were in between the composition of the 60 W samples, but still showed better quality and c -axis orientation.

The diffractograms divided into the different Ga-target power are shown in Figure 31, with zoom-in of the region containing the (0002) peak. This shows that, similar to the samples on Si (100) and glass substrates, the Al content heavily influences the c -axis preferred orientation.

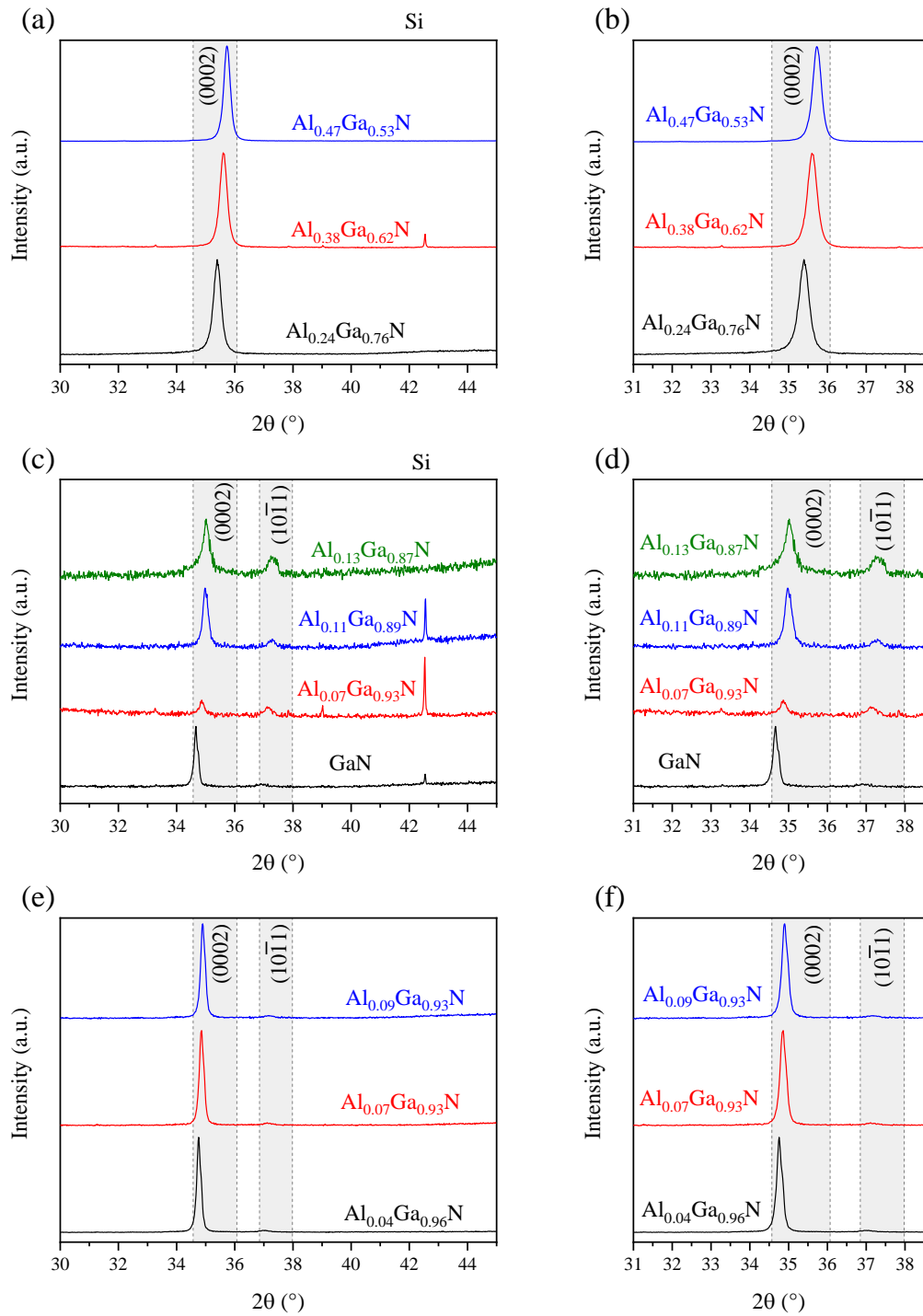


Figure 31: Diffractograms of the $\text{Al}_x\text{Ga}_{1-x}\text{N}$ samples on Si (110) substrate: (a) using 30 W on the Ga target with (b) a zoom-in of the (0002) region, (c) using 60 W on the Ga target with (d) a zoom-in of the (0002) region, and (e) using 90 W on the Ga target with (f) a zoom-in of the (0002) region. Dashed lines indicate the expected position for the AlGaN diffraction peaks.

To further justify the analyses of the samples, lattice parameters and crystallite sizes were calculated and are shown on Figure 32 and Table 12, respectively. The lattice parameter a could not be obtained for samples with the highest Al content (S_50_30, S_75_30, and S_100_30), due to a lack of $(10\bar{1}1)$ plane peak on the diffractograms.

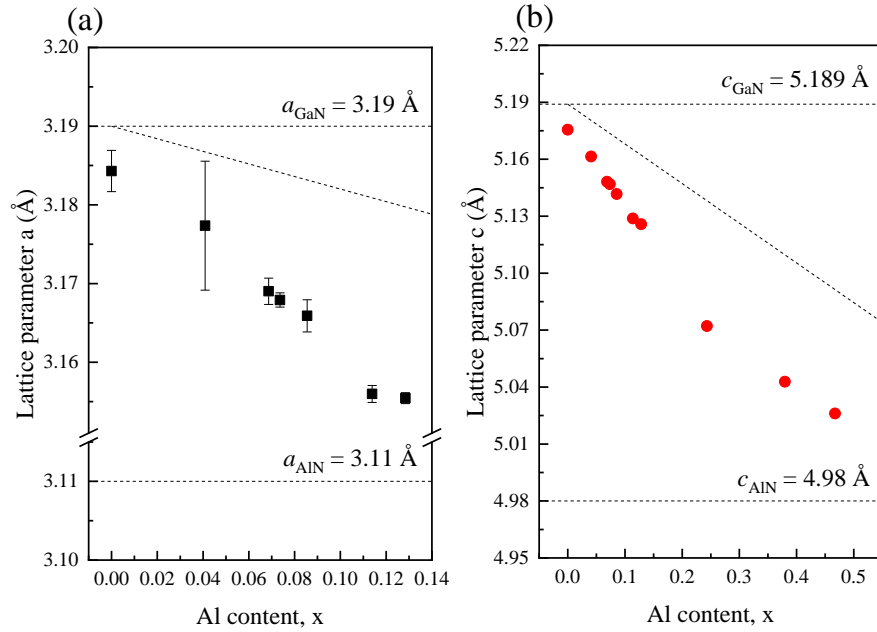


Figure 32: Lattice parameters (a) a and (b) c of the $\text{Al}_x\text{Ga}_{1-x}\text{N}$ samples on Si (110) substrates. The expected values for the unstrained GaN and AlN lattice parameters are indicated, as well as their linear relation. The error bar is not visible because it is smaller than the dots in the graph.

Table 12: Crystallite size of the $\text{Al}_x\text{Ga}_{1-x}\text{N}/\text{Si}$ (110) samples.

Sample	Al content, x	Crystallite size (\AA)
S_0_60	0	486.8 ± 5.3
S_50_90	0.04	455.0 ± 3.4
S_75_90	0.07	432.1 ± 1.4
S_50_60	0.07	485.6 ± 27.5
S_100_90	0.09	437.0 ± 2.0
S_75_60	0.11	381.6 ± 5.0
S_100_60	0.13	329.3 ± 10.9
S_50_30	0.24	265.9 ± 1.0
S_75_30	0.38	279.3 ± 1.2
S_100_30	0.47	314.8 ± 1.0

The lattice parameters show a decreasing tendency with increasing Al content, which is expected, from the values of GaN (0 % Al) to AlN (100 % Al). However, just like for the other substrates, these lattice parameters diverge from the expected unstrained values and linear tendency, which leads to the conclusion that there are stresses on the film. The crystallite sizes, as stated before, are related to the FWHM and peak position, which are shown in Figure 33. There is a general decrease in crystallite size as Al content increases in the film, with some variance.

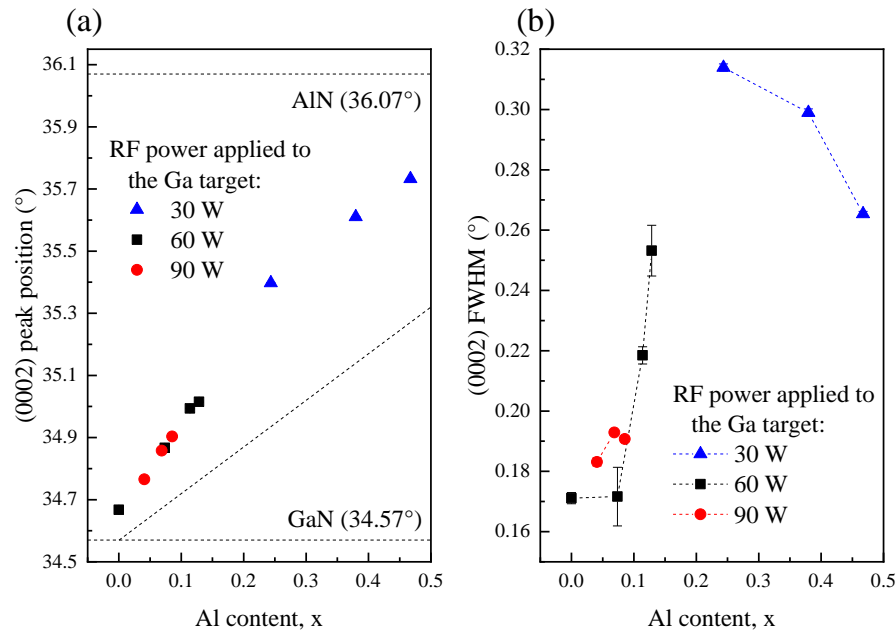


Figure 33: (a) Peak position and (b) FWHM related to the (0002) plane of the $\text{Al}_x\text{Ga}_{1-x}\text{N}$ samples on Si (110) substrate. The expected (0002) peak positions for unstrained GaN and AlN are indicated, as well as their linear relation. The error bar is not visible because it is smaller than the dots in the graph.

The shift in the peak position follows the content of Al in the films, as expected. The FWHM shows a general increase with Al content. In this sense, samples with $x < 0.14$ display smaller widths for the (0002) peak, and although still high, there is a general decrease in FWHM after $x = 0.25$. This behavior is related to the crystallite size, which is calculated according to Equation 11. As this behavior is similar to what was observed for the Si(100) substrate samples, the relation between the FWHM and the thickness of the samples was also verified and is shown in Figure 34.

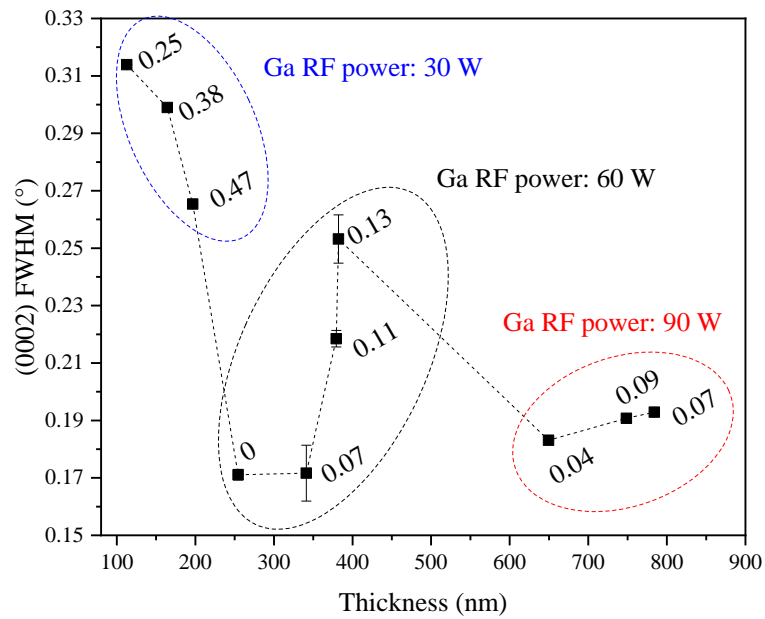


Figure 34: (0002) FWHM related to the thickness of the $\text{Al}_x\text{Ga}_{1-x}\text{N}$ films for the Si(110) substrate. The x values of the composition of the films are indicated as the label of each point.

As seen for the Si(100) substrate, the (0002) FWHM for the $\text{Al}_x\text{Ga}_{1-x}\text{N}$ films on Si(110) substrate also show a strong relation to the thickness of the films, and not only to the Al content. As previously discussed for the Si(100) substrate in Section 4.2.2.2, the FWHM of the low thickness samples are highly dependent of the thickness. After a value $h > 250$ nm, the Al content becomes an important factor alongside the thickness in the FWHM values. The in-plane and out-of-plane strains were calculated as described in Section 4.2.2.1 using Equation 12, and are shown in Table 13.

Table 13: In-plane and out-of-plane strains of the $\text{Al}_x\text{Ga}_{1-x}\text{N}/\text{Si}$ (110) samples.

Sample	Al content, x	ϵ_{xx} (%)	ϵ_{zz} (%)
S_0_60	0	-0.18 ± 0.08	-0.26 ± 0.01
S_50_90	0.04	-0.30 ± 0.26	-0.37 ± 0.01
S_75_90	0.07	-0.49 ± 0.05	-0.51 ± 0.01
S_50_60	0.07	-0.51 ± 0.03	-0.52 ± 0.02
S_100_90	0.09	-0.54 ± 0.06	-0.57 ± 0.01
S_75_60	0.11	-0.78 ± 0.04	-0.70 ± 0.01
S_100_60	0.14	-0.76 ± 0.02	-0.70 ± 0.01
S_50_30	0.24	-	-1.27 ± 0.01
S_75_30	0.38	-	-1.28 ± 0.01
S_100_30	0.47	-	-1.25 ± 0.01

All samples show compressive strains in both directions, but samples $\text{Al}_{0.24}\text{Ga}_{0.76}\text{N}$, $\text{Al}_{0.38}\text{Ga}_{0.62}\text{N}$, and $\text{Al}_{0.47}\text{Ga}_{0.53}\text{N}$ could not have their in-plane strain calculated since, as stated before, the lattice parameter a could not be obtained for them. Sample $\text{Al}_{0.04}\text{Ga}_{0.96}\text{N}$ had an extremely high error for the calculated in-plane strain, which is associated with the error for the lattice parameter a . Nonetheless, in general, an increase in tension can be observed for the samples as the Al content increases.

4.2.2.4 Si (111) substrates

The diffractograms of the $\text{Al}_x\text{Ga}_{1-x}\text{N}$ samples on Si (111) substrates are presented in Figure 35. They are arranged in order of composition, similar to the previous figures, and the two samples with a similar composition (approximately $x = 0.07$) are distinguished in the legend. The expected positions for the (0002) peak of GaN and AlN are indicated on the graph by dashed lines and properly labeled.

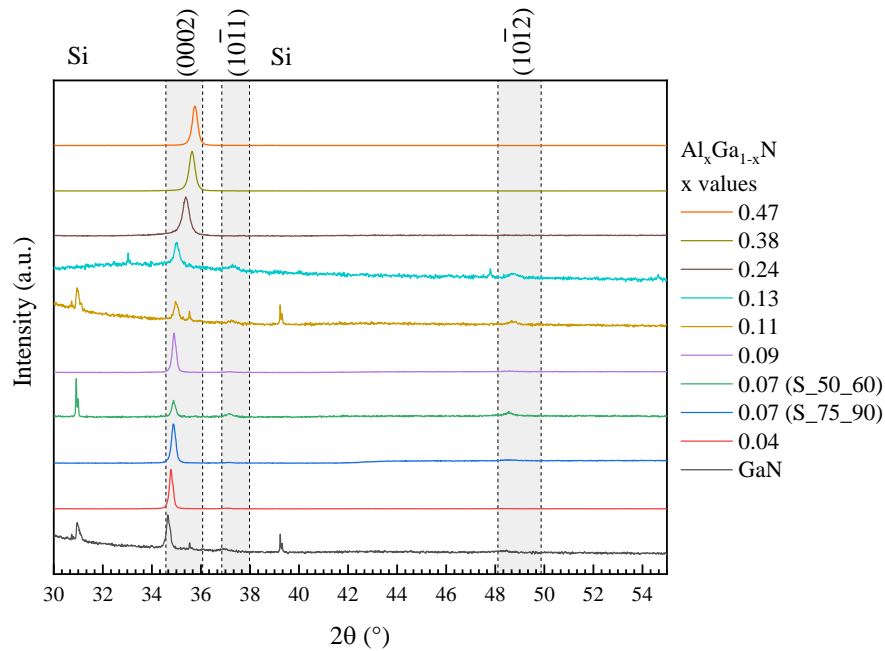


Figure 35: XRD results of the $\text{Al}_x\text{Ga}_{1-x}\text{N}$ samples on Si (111) substrates. Dashed lines indicate the expected position for the $\text{Al}_x\text{Ga}_{1-x}\text{N}$ peaks, that goes from GaN ($x = 0$), in the lower angles, to AlN ($x = 1$), in the higher angles.

Once again, similar to the Si (110) samples, there is a noticeable shift and an increase in the relative intensity of the (0002) peak as Al content increases, but also a disturbance in such a pattern in the samples using 60 W on the Ga target. Even when comparing samples with similar composition (S_75_90, S_50_60, and S_100_90), the one produced using 60 W on the Ga target shows a noticeably lower quality on the diffractogram. However, this distinction was not observed in the glass substrate samples and will be further discussed in Section 4.2.2.5.

Figure 36 shows the diffractograms of the AlGa_{1-x}N films on Si (111) substrates, with a zoom-in of the region containing the (0002) peak. As seen for the other substrates, the increase in Al content plays an important role on the *c*-axis preferred orientation. However, more clearly than in the other substrates, dividing the diffractograms according to the power applied to the Ga target, shows also the effect of the such Ga-target power. Samples produced using 90 W on the Ga target (Figure 36e and f) show more pronounced (0002) peak, i.e., they show a higher preferred orientation when compared to the samples produced using 60 W (Figure 36c and d). This occurs even though the 60 W samples have higher Al content. This could occur due to the difference in thickness for these samples, which will be discussed forward.

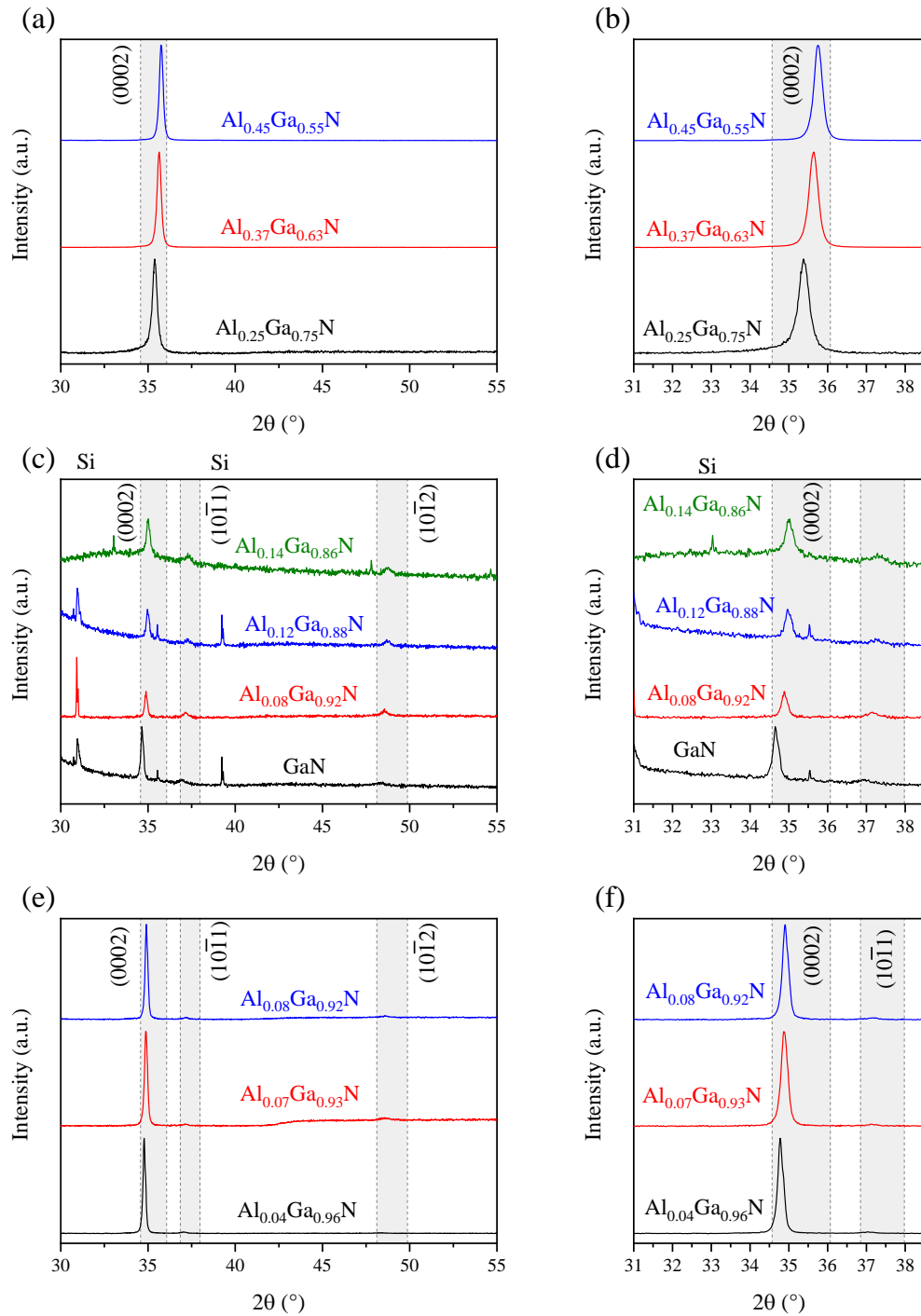


Figure 36: Diffraction patterns of the $\text{Al}_x\text{Ga}_{1-x}\text{N}$ samples on Si (111) substrate: (a) using 30 W on the Ga target with (b) a zoom-in of the (0002) region, (c) using 60 W on the Ga target with (d) a zoom-in of the (0002) region, and (e) using 90 W on the Ga target with (f) a zoom-in of the (0002) region. Dashed lines indicate the expected position for the AlGaN diffraction peaks.

The lattice parameters a and c were calculated as before and are displayed in Figure 37. Once again, the lattice parameter a could not be obtained for samples with higher Al content ($x > 0.13$) and therefore are not shown.

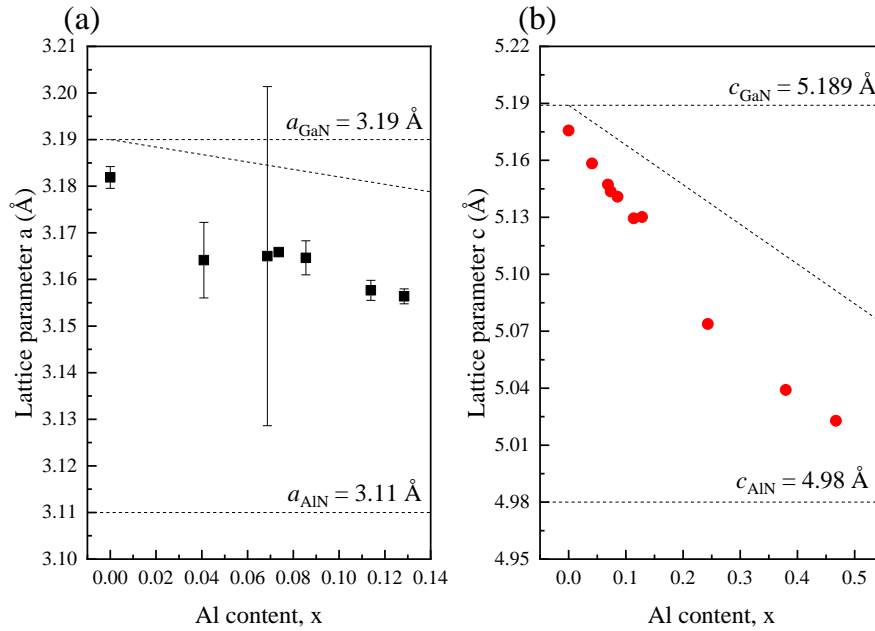


Figure 37: Lattice parameters (a) a and (b) c for the $\text{Al}_x\text{Ga}_{1-x}\text{N}$ samples on Si (111) substrates. The expected values for the unstrained GaN and AlN lattice parameters are indicated, as well as their linear relation. The error bar is not visible because it is smaller than the dots in the graph.

The decrease in the lattice parameters a and c is expected with an increase in Al content. The extremely high error bar for sample $\text{Al}_{0.07}\text{Ga}_{0.93}\text{N}$ (S_75_90) can be associated to the fact that the diffractogram showed a high relative intensity for the (0002) peak. As a result, the values for the peak position obtained for the $(10\bar{1}1)$ plane when fitting had a high associated uncertainty. The divergence of the calculated lattice parameters from an expected linear regression from 5.189 \AA for GaN to 4.98 \AA for AlN indicates strains in the structure.

The crystallite size was calculated for the $\text{Al}_x\text{Ga}_{1-x}\text{N}/\text{Si}$ (111) samples according to Equation 11 and is shown in Table 14.

Table 14: Crystallite size of the $\text{Al}_x\text{Ga}_{1-x}\text{N}/\text{Si}$ (111) samples.

Sample	Al content, x	Crystallite size (\AA)
S_0_60	0	448.4 ± 7.1
S_50_90	0.04	463.4 ± 3.1
S_75_90	0.07	392.0 ± 6.9
S_50_60	0.07	441.8 ± 7.2
S_100_90	0.09	437.7 ± 2.2
S_75_60	0.11	418.2 ± 13.0
S_100_60	0.13	318.8 ± 12.2
S_50_30	0.24	258.0 ± 1.4
S_75_30	0.38	294.7 ± 0.8
S_100_30	0.47	320.4 ± 0.8

There is a decrease in crystallite size with the increase in Al content in the films, as observed in the samples with other Si substrates. The increase in Al content also caused an expected shift in the (0002) peak position and a noticeable increase in FWHM, as observed in Figure 35. These changes are better illustrated in Figure 38 and are related to the crystallite size.

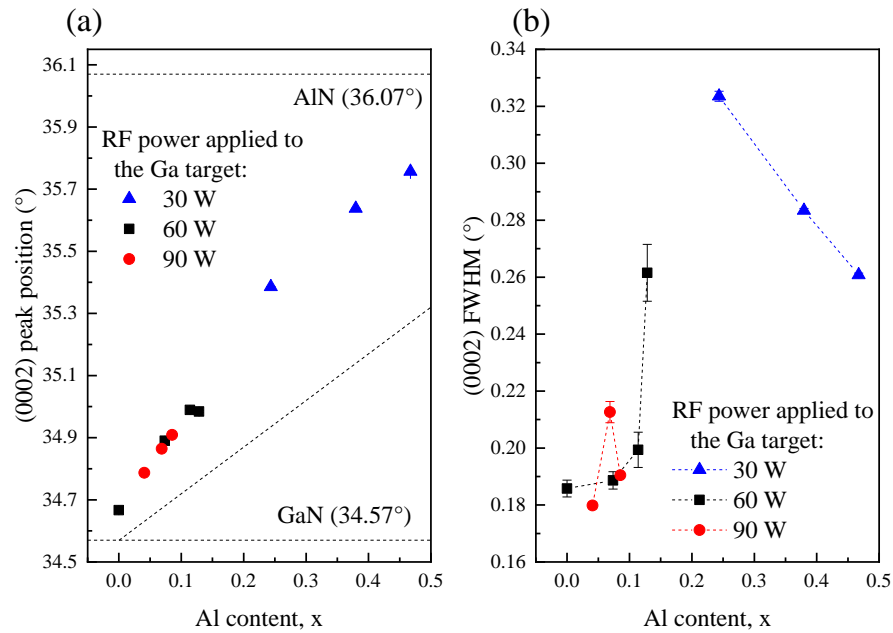


Figure 38: (a) Peak position and (b) FWHM related to the (0002) plane for the $\text{Al}_x\text{Ga}_{1-x}\text{N}$ samples on Si (111) substrate. The expected (0002) peak positions for unstrained GaN and AlN are indicated, as well as their linear relation. The error bar is not visible because it is smaller than the dots in the graph.

The FWHM follows the same pattern as the other samples on Si substrates: an increase in FWHM for samples with $x > 0.13$ and a slight decrease after $x > 0.24$. This could indicate lower quality for these samples, suggesting that the Al content and the increase in c -axis orientation are not necessarily related to the overall crystalline quality, or isn't the only factor influencing the (0002) FWHM. Therefore, similar to the other Si substrates, the relation with the thickness of the films was verified and is shown in Figure 39.

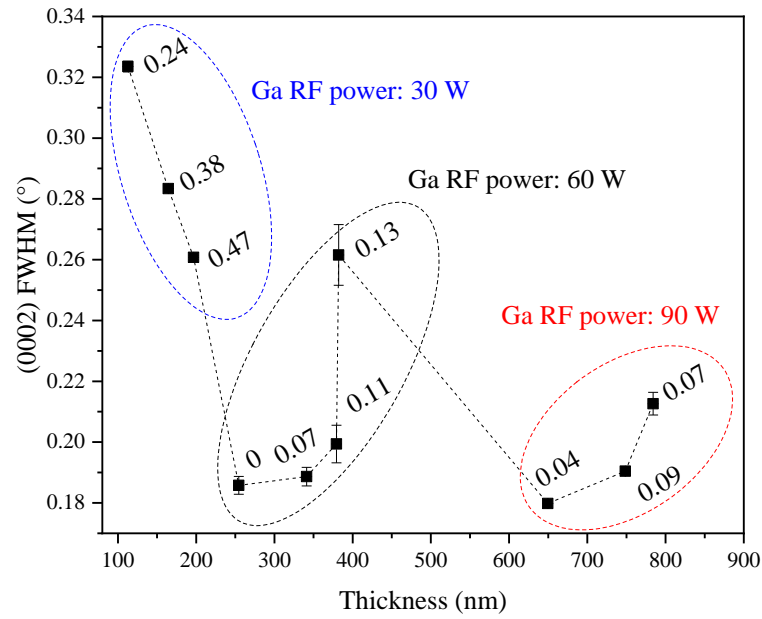


Figure 39: (0002) FWHM related to the thickness of the $\text{Al}_x\text{Ga}_{1-x}\text{N}$ films for the Si(111) substrate. The x values of the composition of the films are indicated as the label of each point.

The (0002) FWHM for the $\text{Al}_x\text{Ga}_{1-x}\text{N}$ films deposited on Si(111) substrates also show a relation to the thickness of the films, as was observed for the other Si substrates, with a strong contribution of the Al content for thicknesses $h > 250$ nm. The in-plane and out-of-plane strains were calculated for the Si (111) substrate samples using Equation 12 and Equation 13, and are shown in Table 15.

Table 15: In-plane and out-of-plane strains of the $\text{Al}_x\text{Ga}_{1-x}\text{N}/\text{Si}$ (111) samples.

Sample	Al content, x	ϵ_{xx} (%)	ϵ_{zz} (%)
S_0_60	0	-0.25 ± 0.07	-0.26 ± 0.01
S_50_90	0.04	-0.71 ± 0.25	-0.43 ± 0.01
S_75_90	0.07	-0.61 ± 1.14	-0.53 ± 0.01
S_50_60	0.07	-0.57 ± 0.02	-0.58 ± 0.01
S_100_90	0.09	-0.58 ± 0.11	-0.59 ± 0.01
S_75_60	0.11	-0.73 ± 0.07	-0.69 ± 0.01
S_100_60	0.14	-0.73 ± 0.05	-0.61 ± 0.01
S_50_30	0.24	-	-1.23 ± 0.01
S_75_30	0.38	-	-1.35 ± 0.01
S_100_30	0.47	-	-1.32 ± 0.01

Samples with high Al content (S_50_30, S_75_30, and S_100_30) could not have their in-plane strain calculated due to a lack of determination for the lattice parameter a . All of the samples show negative values, indicating compressive strains of the films. There is also a general increase in strain as Al content increases, the same as for the other substrates. The elevated associated error for some samples is due to the error in the determination of the lattice parameters. Therefore, some of the results must be considered with care.

4.2.2.5 $\text{Al}_x\text{Ga}_{1-x}\text{N}$ samples summarization

Because of the extensive results for XRD analyses, due to the many studied samples, it is important to summarize them in order to actually call attention to the objective.

Firstly, in terms of c -axis orientation, the glass substrate samples generally exhibited relatively higher (0002) peaks compared to all the Si substrates. Overall, however, for all the different substrate samples, there is a consistent trend that an increase in Al content led to more c -axis oriented samples. It should be emphasized that to accurately assess texture and its coefficient, rocking curve analyses must be performed on the samples. Nevertheless, the

relative intensity serves as a good indicator of the c -axis preferred orientation and has been found to be related to rocking curve analyses in other studies (CHANG et al., 2014).

The degree of c -orientation was calculated by the relative intensity between the (0002) and the other identified peaks as $\frac{I_{(0002)}}{I_{(0002)}+I_{(10\bar{1}1)}}$, where $I_{(0002)}$ and $I_{(10\bar{1}1)}$ are the intensities of the (0002) and (10 $\bar{1}$ 1) diffraction peaks. Values lower than 0.5 indicate that the (10 $\bar{1}$ 1) peak is more intense, and values higher than 0.5 that the (0002) peak is more intense. It was observed that there is a general increase in relative intensity as the Al content increases in the samples. However, samples using 60 W on the Ga target seemed to deviate from this behavior, displaying lower values of relative intensity for the (0002) peak compared to samples with similar composition using different power on the Ga target. The relative intensity for samples using different Si substrates exhibited very similar behaviors, as shown in Figure 40.

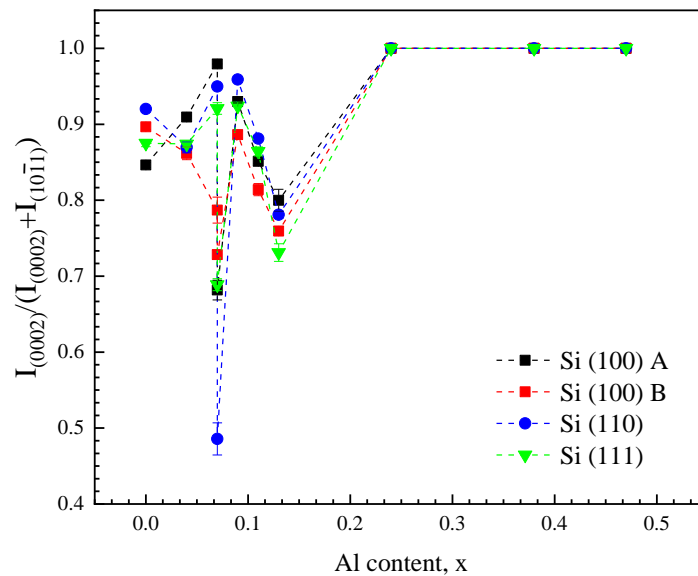


Figure 40: Relative intensity between the (0002) and (10 $\bar{1}$ 1) peaks for the different Si substrate samples. The error bar is not visible because it is smaller than the dots in the graph.

For the glass substrate, the increase in relative intensity is slightly more pronounced, even with the disarrayed 60 W on the Ga target samples, as shown in Figure 41. The overall conclusion is that above a certain Al content ($x = 0.24$ for Si substrates and $x = 0.12$ for glass

substrate), the relative intensity tends to 1, meaning that only (0002) planes could be detected and the samples are highly *c*-oriented. Additionally, the samples produced using 60 W on the Ga target are the ones that showed less preferred orientation.

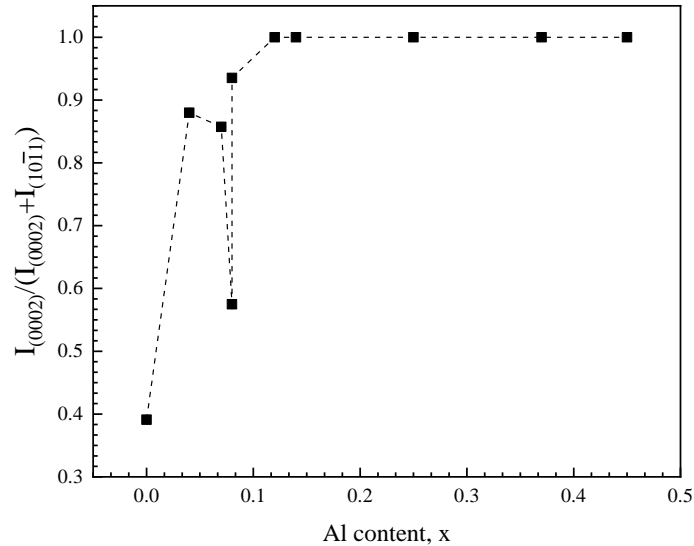


Figure 41: Relative intensity between the (0002) and (10 $\bar{1}$ 1) peaks for the glass substrate samples. The error bar is not visible because it is smaller than the dots in the graph.

When discussing samples S_50_60, S_100_90, and S_75_90, which showed similar compositions on Si and glass substrates (*x* ranging from 0.07 to 0.09), a difference in quality could be observed, especially for the Si substrates. If the Al content were the only parameter to influence the diffractogram characteristics, this effect should not occur, and differences can be seen in Figure 17, Figure 23, Figure 24, Figure 31, and Figure 36. However, there are two important distinctions in these samples: the first is the RF power applied to the Ga target during deposition, and the second is the thickness of the samples.

The RF power could be an important factor, since both samples that were produced using 90 W (S_100_90 and S_75_90) showed better quality, in general. However, the thicknesses of the samples are very different (341.2 ± 0.4 nm for sample S_50_60, 748.6 ± 0.7 nm for sample S_100_90, and 784.0 ± 0.6 nm for sample S_75_90). This could indicate that the thickness is an important factor in the quality of the films and the degree of *c*-axis orientation assessed using XRD, as it was observed for the FWHM in the Si substrate samples, discussed

in Sections 4.2.2.2, 4.2.2.3 and 4.2.2.4, and in other studies (DUQUENNE et al., 2008; SEON et al., 2000). Therefore, in Figure 42 the variation in relative intensity was arranged with the thickness of the samples, except for the high-Al content samples that show a relative intensity equal to 1.

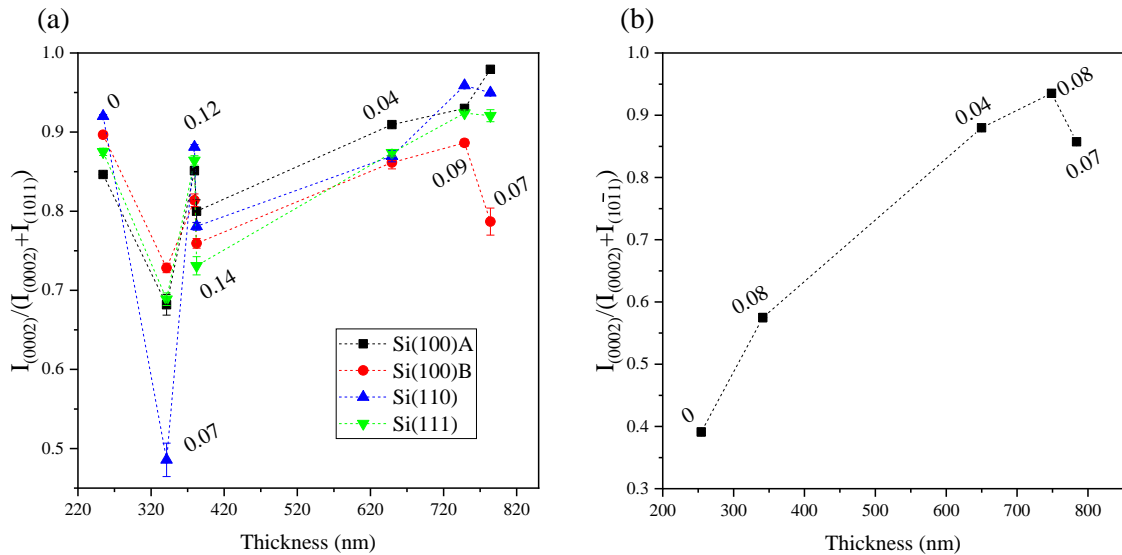


Figure 42: Degree of *c*-orientation (relative intensity of the (0002) peak) in relation to the thickness for (a) the Si substrate samples and (b) the glass substrate samples. The *x* values of the composition of the films are indicated as the label of each point.

The degree of *c*-axis orientation exhibits a relationship with both the thickness and the Al content of the samples. In instances where the samples possess low Al content and/or a similar composition (ranging from 4 to 12 % Al), the influence of thickness on the preferred orientation is more pronounced than that of the Al content, particularly evident in the samples with glass substrates. This phenomenon can be understood as the development of an intermediate layer of random crystals during the initial stages of film growth. This layer subsequently transitions into a more columnar-aligned structure as the thickness increases, a phenomenon elucidated by the Van der Drift model. This growth mechanism has been extensively investigated in GaN films grown on silica or glass substrates, as well as in sputtered AlN films grown on Si substrates (HWANG et al., 2002; LEITE et al., 2011; OLIVEIRA et al., 2023; VAN DER DRIFT, 1967).

The FWHM of the samples exhibit a correlation with the composition and the thickness. In general, as the Al content increased in all samples in Si substrates, an increase in FWHM was observed, without correlating it to any other property. This trend is consistent with other studies that reported an increase in FWHM for AlGa_xN samples deposited on sapphire substrates with AlN buffer layer as Al content increased, which resulted in a decline in quality (FENG et al., 2019; WANG et al., 2017). Additionally, the FWHM shows a decrease with the increase in thickness for the samples deposited in Si substrates, which is also consistent with what was described in the literature (DUQUENNE et al., 2008; LEE; JOO; KIM, 2014; SUN et al., 2016). Therefore, it can be concluded that the crystalline quality in Al_xGa_{1-x}N films depends on both Al content and thickness.

However, for glass substrates, the FWHM decreased as the Al content increased, indicating that an increase in Al was beneficial for the quality of the samples, and no relation to the thickness was observed. Nevertheless, the glass samples with the smallest FWHM (from 0.24 to 0.27°) can be compared to the Si samples with the largest FWHM (0.23 to 0.34° for Si A), showing that the Si is still a better option for the growth of GaN films. A study using MOVPE-grown Al_{0.42}Ga_{0.58}N and Al_{0.50}Ga_{0.50}N samples on Si (111) substrates with an AlN buffer layer exhibited FWHM values for the (0002) peak of 0.32 and 0.38°, respectively, which are much broader than the samples with similar composition (Al_{0.38}Ga_{0.62}N and Al_{0.47}Ga_{0.53}N) in this study, either on Si (111) substrates or on the other Si orientation and glass substrates (WANG et al., 2006).

For all substrates, the increase in Al content led to an increase in compressive strain. They showed similar behavior, especially the different Si substrates with similar strain values. The glass substrate samples had lower strain values. The increase in strains observed in the samples is consistent with what was observed in the literature (JAYASAKTHI et al., 2014).

4.2.3 UV-Vis analyses

Transmission spectra of the Al_xGa_{1-x}N/glass samples and the glass substrate are shown in Figure 43. The increase in aluminum content resulted in the absorption edge of the spectra shifting to lower values of wavelength, as highlighted by the inset in Figure 43. This is expected, as an increase in Al content should lead to higher values of bandgap in the Al_xGa_{1-x}N alloy. The

interference fringes show a regularity compatible with homogeneous composition throughout the thickness of the film, smooth surface and good optical quality.

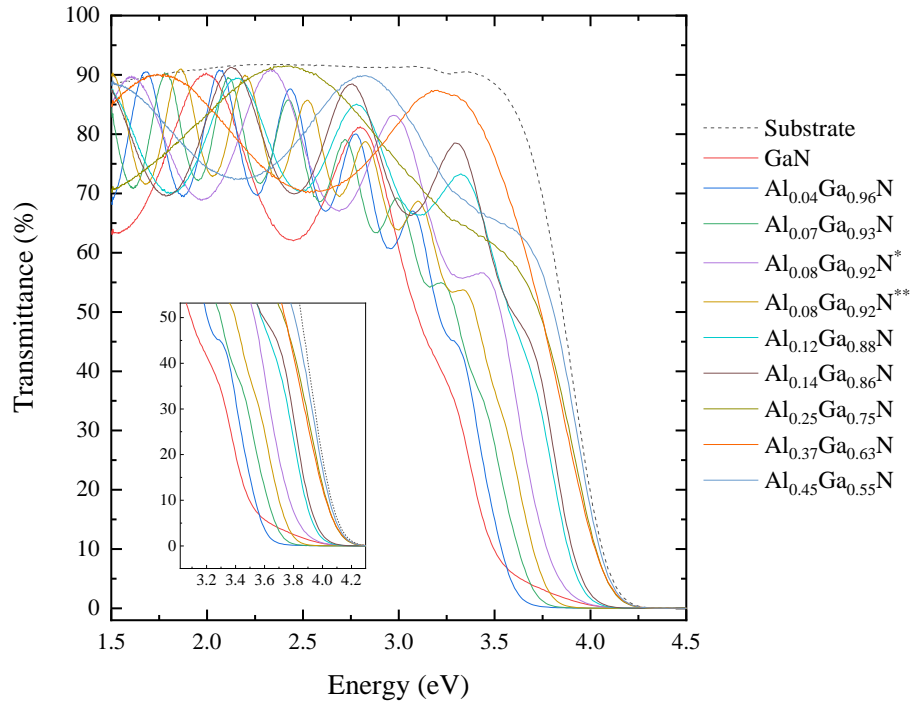


Figure 43: UV-Vis transmission spectra of the $\text{Al}_x\text{Ga}_{1-x}\text{N}$ /glass samples with zoom-in of the absorption edge. *S_50_60, produced using 60 W on the Ga target. **S_100_90, produced using 90 W on the Ga target

It should be noted that samples S_50_30, S_100_30, and S_75_30 (Figure 44c), which were deposited using 30 W on the Ga target, show few fringes on the transmission spectra, resulting in high uncertainty in the analyses. In fact, for sample S_50_30, there wasn't enough data to determine the standard deviation for the calculations. This is due to the low deposition rate resulting from the low RF power on the Ga target power supply, leading to sample thicknesses under 200 nm. Samples deposited using 60 W and 90 W on the Ga target are shown in Figure 44a and Figure 44b, respectively.

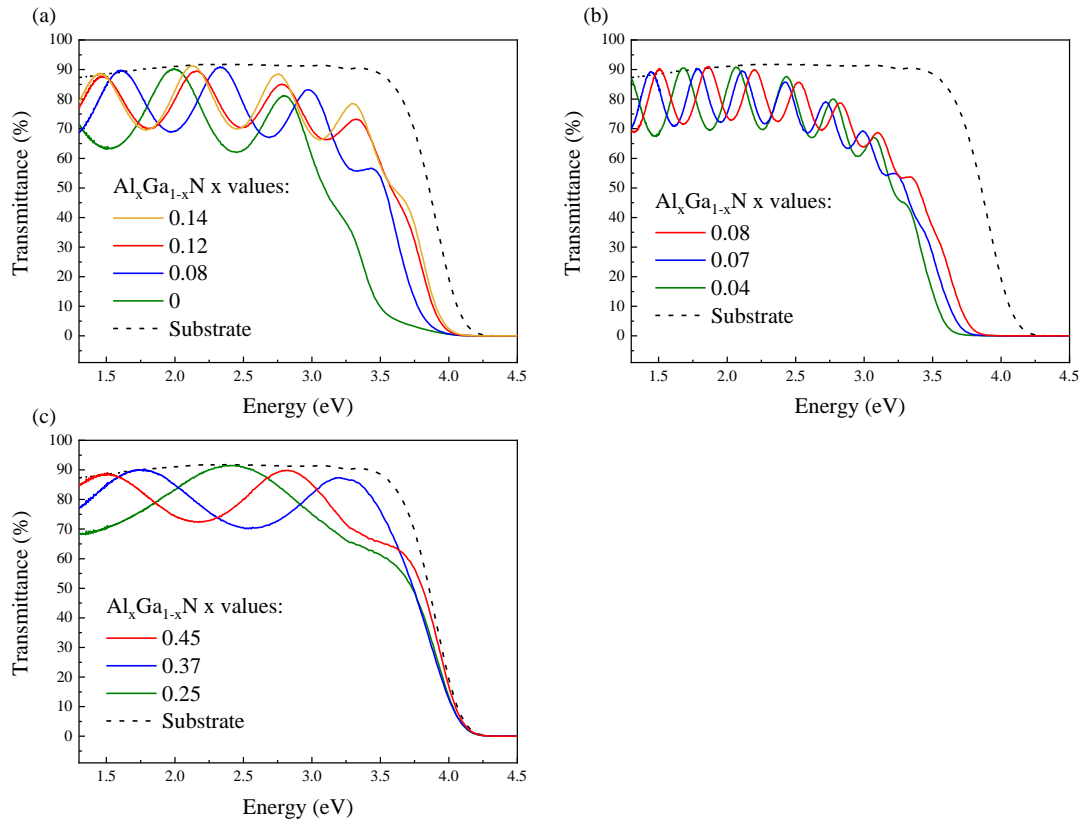


Figure 44: UV-Vis transmission spectra of the $\text{Al}_x\text{Ga}_{1-x}\text{N}$ samples deposited using (a) 60 W, (b) 90 W, and (c) 30 W, on the RF supply for the Ga target.

Thickness, static refractive index, and bandgap E_g were obtained through the UV-Vis measurements and are shown in Table 16 (except for thickness, which was discussed previously and is shown in Table 7). The bandgap E_g was obtained as the energy where the absorption coefficient overcome $7.4 \times 10^4 \text{ cm}^{-1}$. This approach to E_g is known to avoid underestimation of the bandgap due to subgap absorption and absorption of free excitons (ANGERER et al., 1997).

Due to the increase in Al content and the shift of the spectra, the samples S_50_30, S_100_30, and S_75_30 show high values of error for the bandgap. This occurs because of the absorption limit of the substrate at $\sim 300 \text{ nm}$, which interferes with the samples when the bandgap is near or above this value. Since the bandgap values for $\text{Al}_x\text{Ga}_{1-x}\text{N}$ can vary from 3.42 eV ($x = 0$) to 6.2 eV ($x = 1$), when the Al content increases in the sample, the bandgap shifts to higher values and receives more interference from the substrate on the UV-Vis analysis.

Table 16: Calculations from the UV-Vis data for the $\text{Al}_x\text{Ga}_{1-x}\text{N}$ samples.

Sample	Al content, x	Static refractive index	Bandgap E_{04} (eV)
S_0_60	0	2.328 ± 0.002	3.374 ± 0.005
S_50_90	0.04	2.210 ± 0.002	3.516 ± 0.003
S_75_90	0.07	2.147 ± 0.002	3.672 ± 0.003
S_50_60	0.08	2.207 ± 0.002	3.744 ± 0.003
S_100_90	0.08	2.156 ± 0.002	3.742 ± 0.005
S_75_60	0.12	2.181 ± 0.001	3.871 ± 0.001
S_100_60	0.14	2.193 ± 0.001	3.911 ± 0.002
S_50_30	0.25	2.170 ± 0.001	4.16 ± 0.02
S_75_30	0.37	2.144 ± 0.001	4.2 ± 0.2
S_100_30	0.45	2.118 ± 0.001	4.19 ± 0.04

The refractive index shows an overall decrease with increasing Al content when comparing samples using the same RF power on the Ga target, as shown in Figure 45, which is consistent with the variation of refractive index from GaN ($x = 0$) to AlN ($x = 1$). This relationship was also verified by Brunner *et al.* (BRUNNER *et al.*, 1997).

Comparing samples with different parameters, such as different RF power for the Ga target, could lead to misinterpretation of the results, as they could show different densities of point defects that can affect the refractive index and cause shifts, as discussed in Section 2.1.3 using Equation 6.

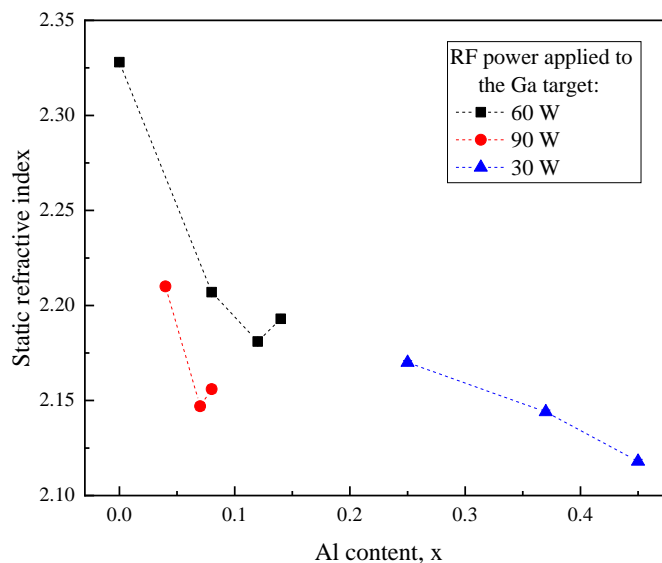


Figure 45: Static refractive index as a function of Al content highlighting the different RF power used. The error bar is not visible because it is smaller than the dots in the graph.

The bandgap increased with the increase in Al content for the $\text{Al}_x\text{Ga}_{1-x}\text{N}$ samples, and the relationship between E_g and Al content is shown in Figure 46a. Figure 46b shows a comparison between the bandgap for the $\text{Al}_x\text{Ga}_{1-x}\text{N}$ produced in this work and the bandgap from other reports using different deposition techniques (ANGERER et al., 1997; JIANG et al., 2001; KOIDE et al., 1987; LI et al., 2021; TAKEUCHI et al., 1997; TISCH et al., 2001; YUN et al., 2002). The discrepancy in the bandgaps can be explained by the use of different deposition techniques/parameters and the strain status of the samples (LI et al., 2021). The high values of bandgap obtained for some of the $\text{Al}_x\text{Ga}_{1-x}\text{N}$ samples may be related to the density of defects in the films and the compressive strains calculated using the XRD results (Table 9).

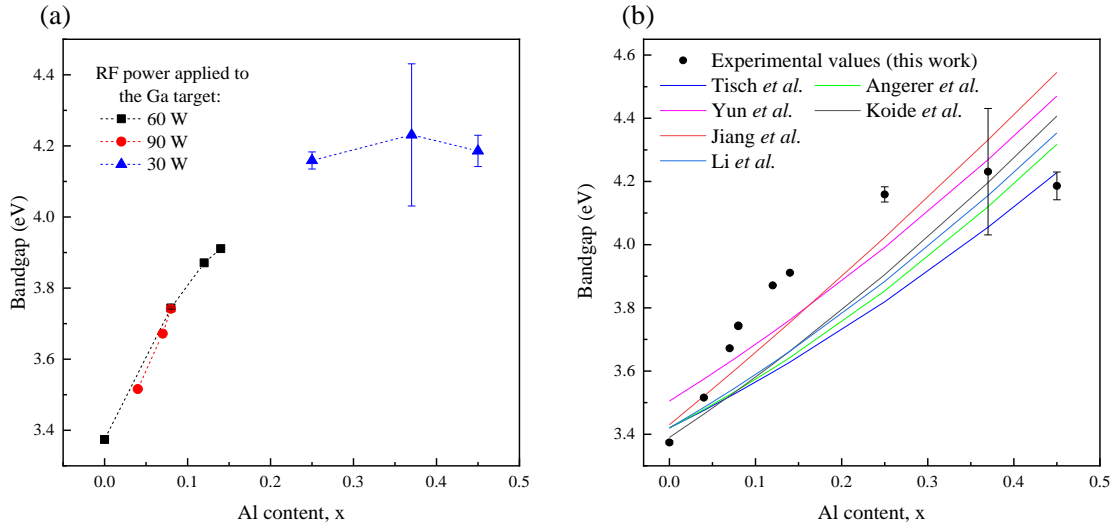


Figure 46: (a) Bandgap E_g of the $\text{Al}_x\text{Ga}_{1-x}\text{N}$ samples and its relation to the Al content highlighting the different RF power used and (b) the comparative with reference data (ANGERER *et al.*, 1997; JIANG *et al.*, 2001; KOIDE *et al.*, 1987; LI *et al.*, 2021; TAKEUCHI *et al.*, 1997; TISCH *et al.*, 2001; YUN *et al.*, 2002). The error bar is not visible because it is smaller than the dots in the graph.

Even for samples that showed no correlation with the composition for the static refractive index (which was explained as being due to different densities of defects), the bandgap values still exhibited a trend of increasing with the Al content. Samples with the same composition demonstrated extremely accurate and similar bandgap values. When examining at the trend for the samples produced using 60 and 90 W (the lower Al content samples), they followed the same path for bandgap values (Figure 46a).

4.2.4 Raman spectroscopy

Unstrained wurtzite GaN thin films usually show E_2^H and $A_1(\text{LO})$ active phonon modes at 568 cm^{-1} and 734 cm^{-1} , respectively, the E_2^H being the more strong and common for hexagonal GaN (DAVYDOV *et al.*, 1998; HARIMA, 2002). The Raman spectra for the $\text{Al}_x\text{Ga}_{1-x}\text{N}$ on glass substrate samples, along with a pure glass substrate spectrum, are shown in Figure 47, and the expected E_2^H and $A_1(\text{LO})$ for GaN are also indicated in the figure.

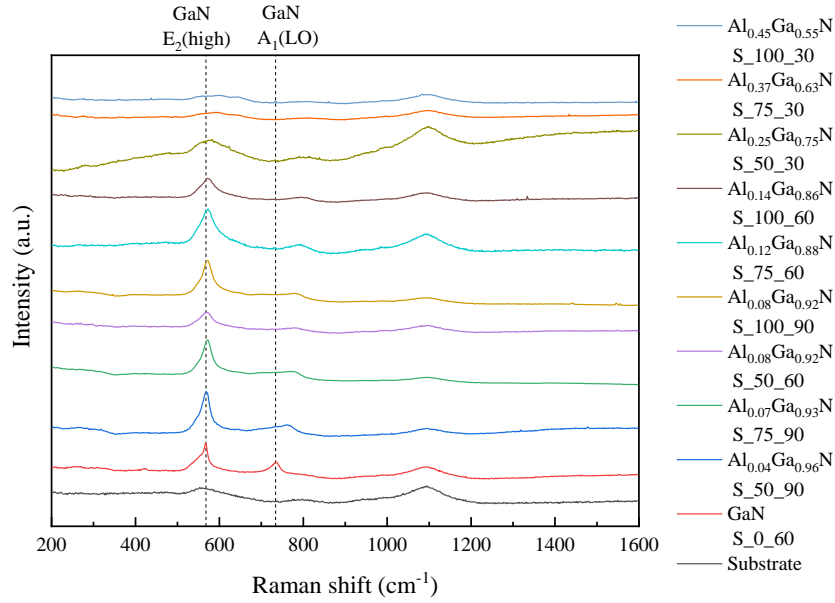


Figure 47: Raman spectra of the $\text{Al}_x\text{Ga}_{1-x}\text{N}/\text{glass}$ samples and the glass substrate. Dashed lines indicate the expected positions for the E_2^{H} and $\text{A}_1(\text{LO})$ phonon modes for GaN.

Both phonon modes, E_2^{H} and $\text{A}_1(\text{LO})$, have their frequency affected by the Al content of the film. A shift in the E_2^{H} peak position towards higher wavenumber can be observed, indicating compressive strain in the films, in good agreement with the calculations from the XRD results. The increase in Al content, as discussed in Section 2.1.1, leads to a natural blueshift in the E_2^{H} peak position, as well as the appearance of a shoulder for specific compositions, and makes it impossible to distinguish between the E_2^{H} and $\text{E}_1(\text{TO})$ modes. These effects can be more clearly seen in the magnification of the region where the E_2^{H} , $\text{E}_1(\text{TO})$ and $\text{A}_1(\text{LO})$ peaks are located, in Figure 48.

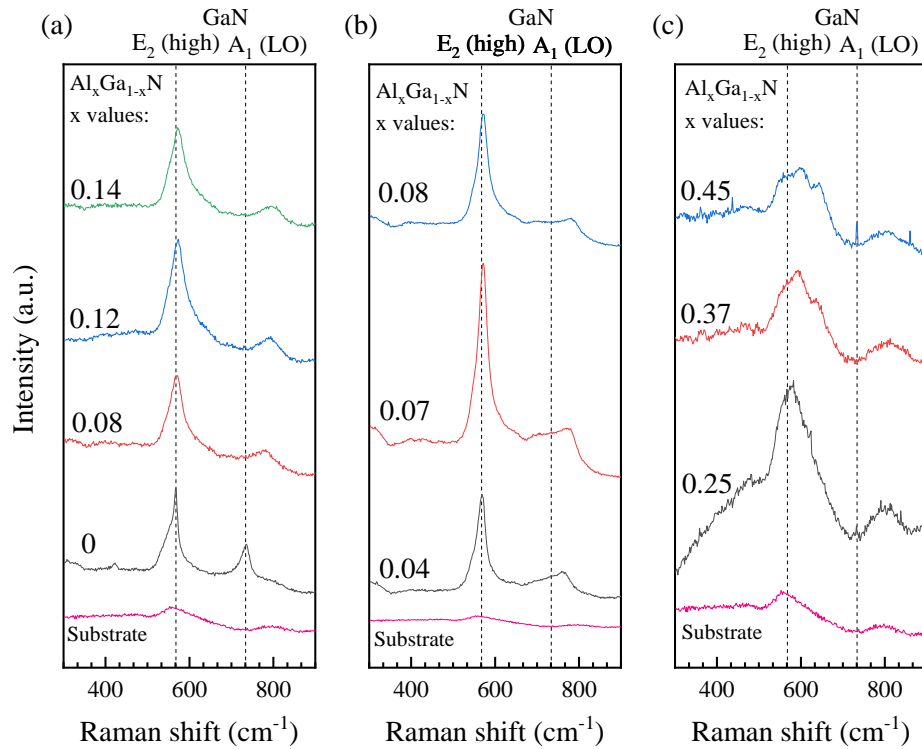


Figure 48: Magnification of Raman spectra of pure GaN, AlGaN thin films, and glass substrate detailing the E_2 (high) and A_1 (LO) phonon modes for samples deposited using (a) 60 W, (b) 90 W, and (c) 30 W on the Ga-target RF-power supply.

The shift in the E_2^H -related peak for the GaN sample (S_0_60) was calculated to be 0.5 cm^{-1} from the expected unstrained value of 568 cm^{-1} , which is relatively negligible. As the Al content increases in the samples, the blueshift in the GaN-like E_2^H becomes more apparent, consistent with the compressive strains observed in the XRD results. The abrupt shift for samples with higher x values (0.37 and 0.45) could be related to the high values of strains (see Table 9).

Additionally, the composition is above the determined 0.36 for the appearance of a shoulder on a higher frequency, which could interfere with the analyses (DAVYDOV et al., 2002). Apart from these samples whose results are highly uncertain, Figure 49 shows the Raman shift of the E_2^H phonon mode according to the Al content, indicating that the composition of the sample is an important factor that changes the E_2^H peak position.

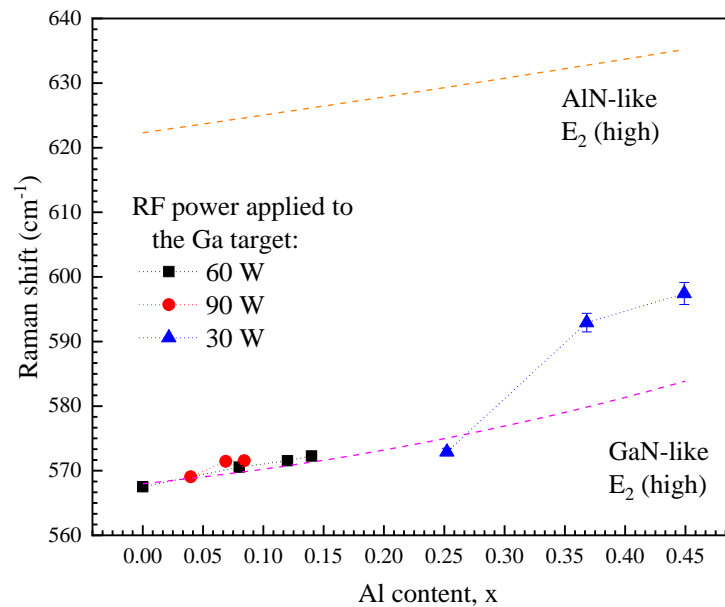


Figure 49: E_2^H peak Raman shift of the $Al_xGa_{1-x}N$ samples on glass substrates for the different RF power used on the Ga-target. The dashed pink line shows the expected position for the GaN-like E_2^H phonon mode of the AlGaN alloy. The error bar is not visible because it is smaller than the dots in the graph.

The blueshift in the $A_1(LO)$ phonon mode is noticeable with the increase in Al content for the $Al_xGa_{1-x}N$ samples, which is consistent with the literature. Some studies explain this behavior due to phonon confinement or electron-phonon coupling. Specially, the phonon confinement effect is associated to a reduction in crystal dimensions as Al replaces the Ga atoms (WANG et al., 2017). This shift is consistent with compressive strains in the crystal. The $A_1(LO)$ position is shown in Figure 50, along with the expected values obtained according to Equation 1.

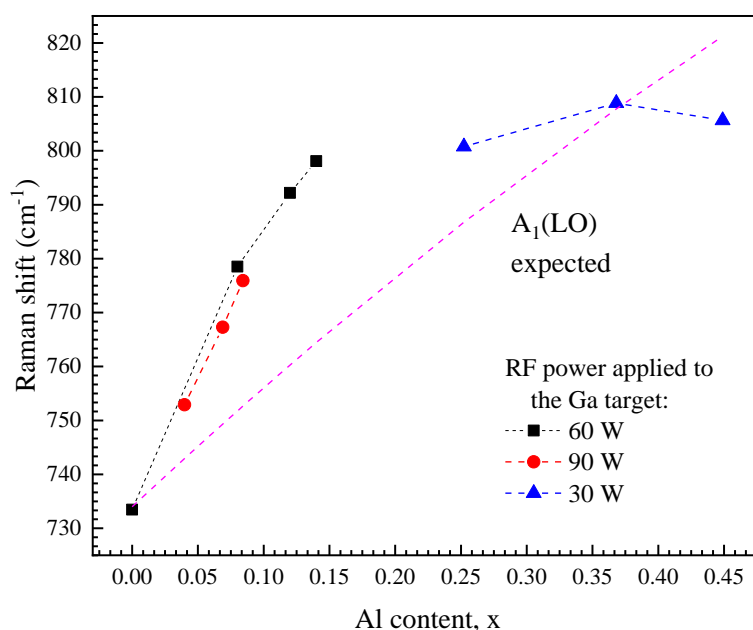


Figure 50: $A_1(\text{LO})$ peak Raman shift of the $\text{Al}_x\text{Ga}_{1-x}\text{N}$ samples on glass substrates for the different RF power used on the Ga-target. The dashed pink dashed line shows the expected position for the $A_1(\text{LO})$ phonon mode of the AlGa N alloy. The error bar is not visible because it is smaller than the dots in the graph.

Although the shift in the $A_1(\text{LO})$ position occurs, such positions differ from the expected values, shown in Figure 50 as the pink dashed line. Except for the Ga N sample ($x = 0$) and the richer AlGa N sample ($x = 0.45$), the $A_1(\text{LO})$ peak appears on higher values than the expected. This tendency could suggest the presence of compressive strains within the structure, further substantiating the outcomes obtained from the XRD calculations and the findings derived from the bandgap study.

4.3 GaN/AlGa N heterostructures

4.3.1 X-Ray diffraction

As described in Section 3.4, seven (7) heterostructures were produced with $\text{Al}_x\text{Ga}_{1-x}\text{N}$ layers with different values of x , thicknesses, and number of layers. These heterostructures on

Si(100) substrates were analyzed using XRD and compared among each other in terms of those variations. For clarification purposes, these analyses will be divided into subsections. Also, for comparison, the XRD of the GaN/Si(100) film without buffer layer is shown in Figure 51. The diffractograms of the heterostructures in glass substrates are shown in Appendix A and pose similar conclusions from the Si(100) substrate samples. Since the substrate is not influencing the analyses, only the Si(100) samples are shown here.

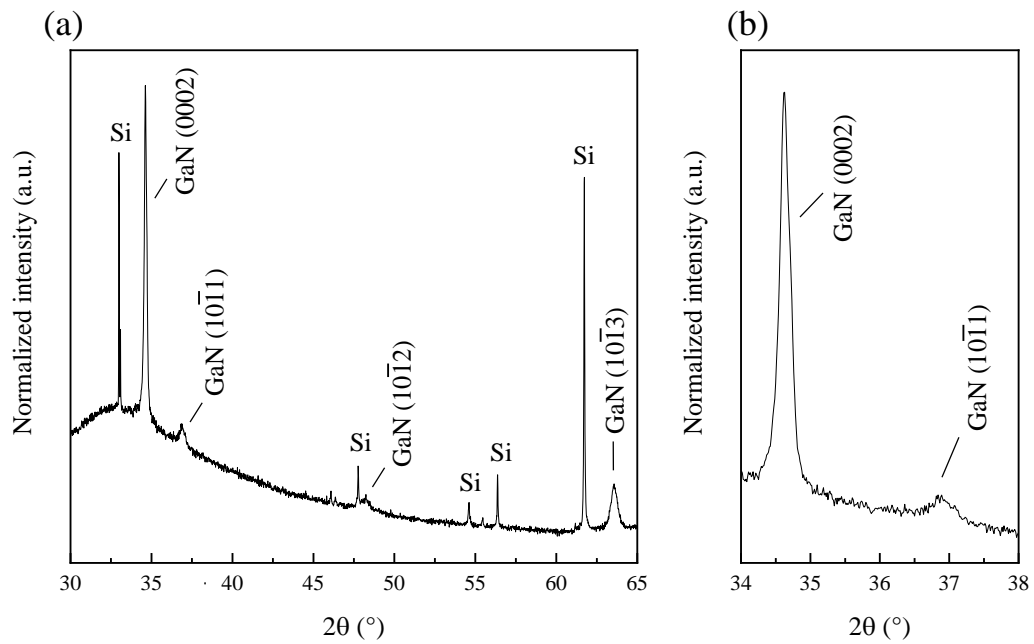


Figure 51: (a) X-Ray diffractogram of the GaN/Si(100) film without buffer layer and (b) zoom-in on the (0002) peak region.

4.3.1.1 Buffer layer thickness

The effect of the thickness of the $\text{Al}_x\text{Ga}_{1-x}\text{N}$ buffer layer can be seen in the heterostructures using low-Al content or high-Al content. Figure 52 shows the diffractograms of samples H_A_150, H_A_120, and H_A_37, all with one $\text{Al}_{0.07}\text{Ga}_{0.93}\text{N}$ (low-Al content) layer with different thicknesses.

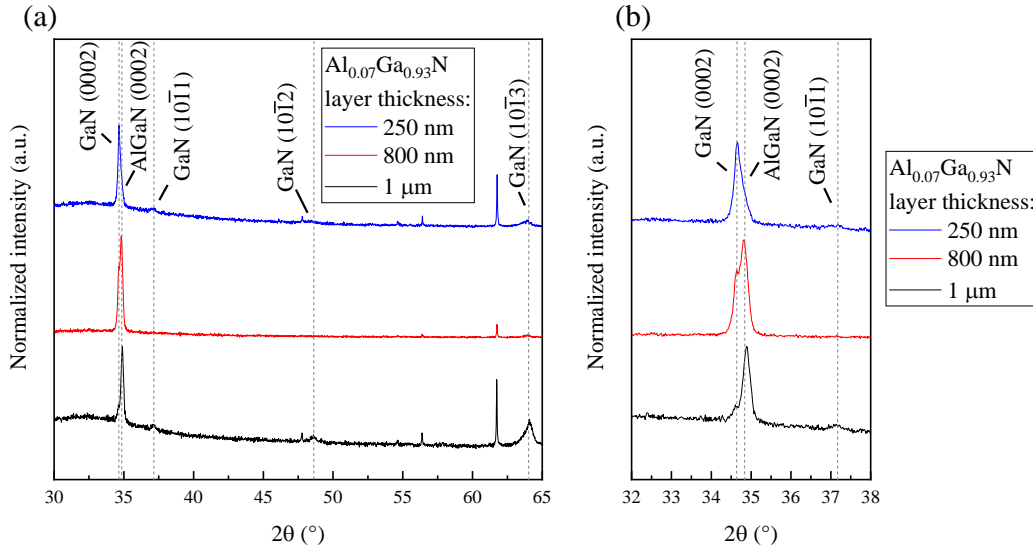


Figure 52: (a) Diffractogram of different buffer layer thicknesses of three GaN/ $\text{Al}_{0.07}\text{Ga}_{0.93}\text{N}$ heterostructures and (b) zoom in on the region with the (0002) peak.

The double peak at $\sim 35^\circ$, which can be better observed in Figure 52(b) is due to the mixing of the (0002) peaks of the GaN and $\text{Al}_x\text{Ga}_{1-x}\text{N}$ layers. In comparison to the GaN without buffer layer (Figure 51), the increase in the relative intensity of the GaN (0002) peak shows an improvement in c -axis orientation. An improvement in peak-noise ratio is also visible. However, the other diffraction peaks are still visible. The different thicknesses did not create obvious changes, and the (0002) peaks were deconvoluted and fitted. The results are shown in Table 17.

Table 17: Fitting results of the (0002) peak position and FWHM of the GaN/ $\text{Al}_{0.07}\text{Ga}_{0.93}\text{N}$ heterostructures.

$\text{Al}_{0.07}\text{Ga}_{0.93}\text{N}$ thickness (nm)	GaN (0002) peak position ($^\circ$)	GaN (0002) FWHM ($^\circ$)	$\text{Al}_{0.07}\text{Ga}_{0.93}\text{N}$ (0002) peak position ($^\circ$)	$\text{Al}_{0.07}\text{Ga}_{0.93}\text{N}$ (0002) FWHM ($^\circ$)
1 000	34.638 ± 0.017	0.329 ± 0.043	34.891 ± 0.001	0.205 ± 0.003
800	34.620 ± 0.001	0.154 ± 0.003	34.823 ± 0.001	0.227 ± 0.002
250	34.646 ± 0.001	0.139 ± 0.007	34.738 ± 0.008	0.327 ± 0.009

The increase in thickness shifted the $\text{Al}_{0.07}\text{Ga}_{0.93}\text{N}$ to higher values, further from the expected unstrained position ($\sim 34.673^\circ$). However, it also led to a decrease in the FWHM, which is consistent with what was described in Section 2.1.1. On the other hand, the position of the GaN (0002) peak showed no clear relation to the thickness of the buffer layer, but the FWHM of the GaN (0002) peak increased greatly for the sample with $1\mu\text{m}$ thickness.

Figure 53 shows the diffractograms for the heterostructures using one high-Al content buffer (H_B_120 and H_B_180).

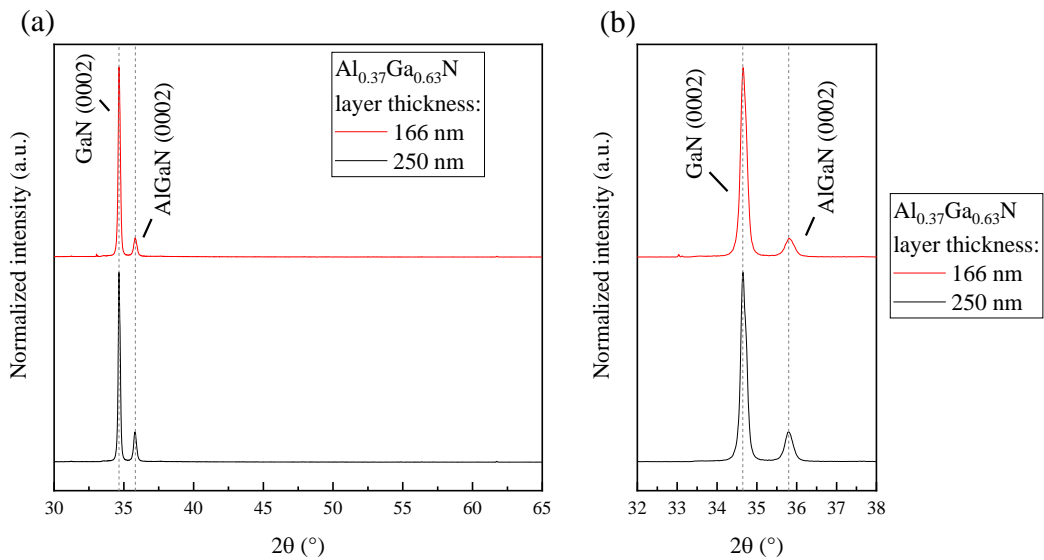


Figure 53: (a) Diffractogram of different buffer layer thicknesses of three GaN/ $\text{Al}_{0.37}\text{Ga}_{0.63}\text{N}$ heterostructures and (b) zoom in on the region with the (0002) peak.

There is a clear distinction between the (0002) peaks for the GaN and $\text{Al}_{0.37}\text{Ga}_{0.63}\text{N}$ layers. The GaN (0002) peak shows a high intensity, and no other peaks can be observed. This allows us to conclude that for either thickness, the $\text{Al}_{0.37}\text{Ga}_{0.63}\text{N}$ buffer led to a highly c -axis oriented GaN film with no clear distinction between the different thicknesses. The (0002) peak position and FWHM for the GaN and $\text{Al}_{0.37}\text{Ga}_{0.63}\text{N}$ layers are shown in Table 18.

Table 18: Fitting results of the (0002) peak position and FWHM of the GaN/Al_{0.37}Ga_{0.63}N heterostructures.

Al _{0.37} Ga _{0.63} N thickness (nm)	GaN (0002) peak position (°)	GaN (0002) FWHM (°)	Al _{0.37} Ga _{0.63} N (0002) peak position (°)	Al _{0.37} Ga _{0.63} N (0002) FWHM (°)
250	34.667 ± 0.001	0.175 ± 0.001	35.806 ± 0.003	0.240 ± 0.010
166	34.669 ± 0.001	0.186 ± 0.001	35.825 ± 0.005	0.261 ± 0.013

The increase in the thickness of the Al_{0.37}Ga_{0.63}N layer shifted the (0002) position to lower values, closer to the expected unstrained value (~35.139°) and led to a decrease in the FWHM, which is also compatible with what was previously discussed. The GaN (0002) peak position showed no relation to the buffer layer thickness, but the FWHM showed a slight decrease with the buffer layer thickness.

From what was observed for the variation of thickness of the low-Al content and high-Al content buffer layer heterostructures, the buffer layer thickness showed no direct or clear effect on the GaN layer, apart from the 1 μm buffer on sample H_A_150 that created a larger FWHM. Therefore, lower thickness - which is also related to an optimization of the deposition time – is more suitable for the production of the GaN/Al_xGa_{1-x}N heterostructures.

4.3.1.2 Buffer layer composition

To understand the effect of the Al_xGa_{1-x}N buffer layer composition on the GaN film, two heterostructures with the same thickness (~250 nm) (H_A_37 and H_B_180) were deposited, one with low-Al content ($x = 0.07$) and one with high-Al content ($x = 0.37$) buffer layer. Their normalized diffractograms can be seen in Figure 54. The GaN (0002) peak is presented at ~34.6° for both samples, the Al_{0.07}Ga_{0.93}N (0002) peak is presented at ~34.7° for sample H_A_37 (which is convoluted with the GaN one) and the Al_{0.37}Ga_{0.63}N (0002) peak is presented at ~35.8° for sample H_B_180.

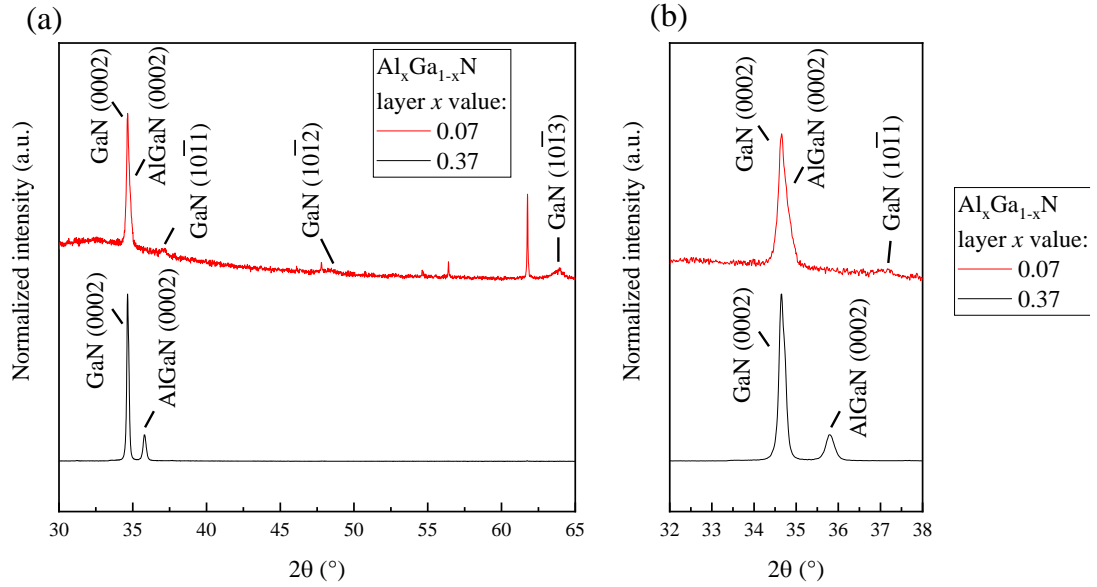


Figure 54: (a) Diffractogram of different 250 nm buffer layer composition of two GaN/ $\text{Al}_x\text{Ga}_{1-x}\text{N}$ heterostructures and (b) zoom in on the region with the (0002) peak.

From the diffractograms, a clear improvement in the crystalline quality and c -axis orientation of the GaN can be seen as the Al-content on the buffer layer increases. Sample H_A_37 ($x = 0.07$) showed a low intensity for the GaN (0002) peak and the presence of peaks related to other planes, while sample H_B_180 ($x = 0.37$) showed a high intensity and isolated GaN (0002) peak. When compared to the GaN sample without buffer (Figure 51), the Al-rich buffer greatly increased the relative intensity of the GaN (0002) peak. There is also an obvious improvement in the peak-to-noise ratio. The results for peak position and FWHM of the heterostructures are presented in Table 19.

Table 19: Fitting results of the (0002) peak position and FWHM of the GaN/ $\text{Al}_x\text{Ga}_{1-x}\text{N}$ heterostructures with 250 nm buffer layer.

$\text{Al}_x\text{Ga}_{1-x}\text{N}$ x value	GaN (0002) peak position (°)	GaN (0002) FWHM (°)
0.07	34.646 ± 0.001	0.139 ± 0.007
0.37	34.667 ± 0.001	0.175 ± 0.001

The changes in the GaN (0002) peak position and FWHM can be indicative that the low-Al content layer was more effective in reducing strains and increasing the crystallite size of the GaN film. The low-Al content samples were also produced with a shorter deposition time. However, the increase in *c*-axis orientation of the GaN film is still an important factor to consider for the production of the heterostructures when aiming for SAW devices, due to improving the piezoelectric properties (IRIARTE; RODRÍGUEZ; CALLE, 2010). In this sense, the high-Al content buffer layer is more suitable for this purpose.

4.3.1.3 Buffer layer number and compositional gradient

In three samples, the number of buffer layers with a compositional gradient was varied. To compare them, all the $\text{Al}_x\text{Ga}_{1-x}\text{N}$ layers were produced using a deposition time of 120 minutes, as in the previously studied films. As shown in Figure 12, sample H_B_120 has one $\text{Al}_{0.37}\text{Ga}_{0.63}\text{N}$ layer (GaN/ $\text{Al}_{0.37}\text{Ga}_{0.63}\text{N}$), sample H_C_120 has one $\text{Al}_{0.37}\text{Ga}_{0.63}\text{N}$ and one $\text{Al}_{0.24}\text{Ga}_{0.76}\text{N}$ layer (GaN/ $\text{Al}_{0.24}\text{Ga}_{0.76}\text{N}/\text{Al}_{0.37}\text{Ga}_{0.63}\text{N}$), and sample H_D_120 has one $\text{Al}_{0.37}\text{Ga}_{0.63}\text{N}$, one $\text{Al}_{0.24}\text{Ga}_{0.76}\text{N}$ and one $\text{Al}_{0.07}\text{Ga}_{0.93}\text{N}$ layer (GaN/ $\text{Al}_{0.07}\text{Ga}_{0.93}\text{N}/\text{Al}_{0.24}\text{Ga}_{0.76}\text{N}/\text{Al}_{0.37}\text{Ga}_{0.63}\text{N}$). Figure 55 shows the diffractograms of these samples.

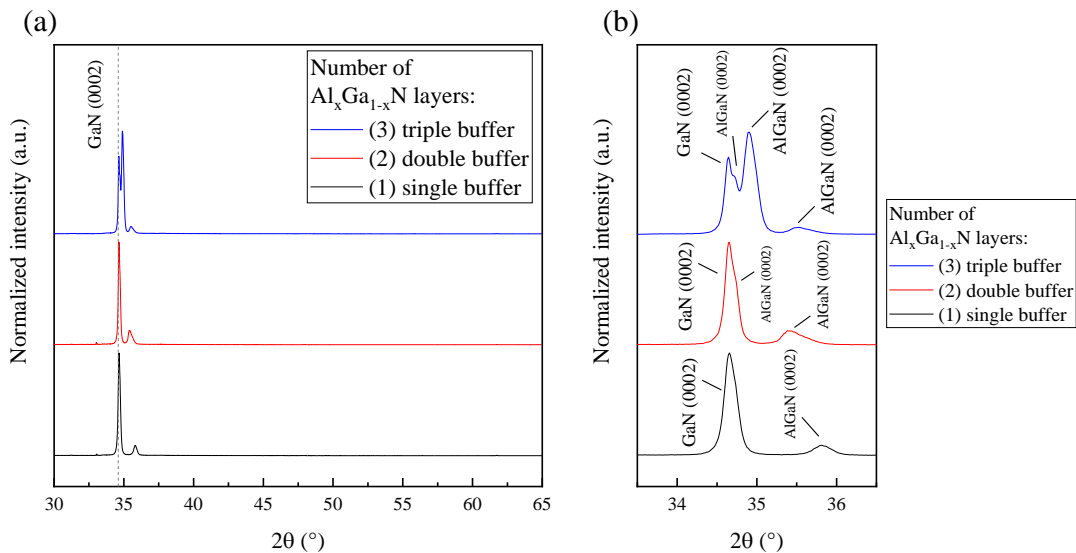


Figure 55: (a) Diffractogram of different buffer layer number of three heterostructures and (b) zoom in on the region with the (0002) peak.

The increase of the number of peaks in the $34 - 36^\circ$ region is due to the (0002) peaks for the different layers of GaN and $\text{Al}_x\text{Ga}_{1-x}\text{N}$. In terms of c -axis orientation, all samples show only GaN (0002) related peaks, with high relative intensity. These peaks were fitted in terms of position and FWHM, and the results are shown in Table 20.

Table 20: Fitting results of the GaN (0002) peak position and FWHM of the heterostructures with different number of buffer layers.

Number of $\text{Al}_x\text{Ga}_{1-x}\text{N}$ layers:	GaN (0002) peak position ($^\circ$)	GaN (0002) FWHM ($^\circ$)
No buffer (0)	34.6293 ± 0.0005	0.184 ± 0.002
One (1)	34.669 ± 0.001	0.186 ± 0.001
Two (2)	34.655 ± 0.005	0.145 ± 0.012
Three (3)	34.633 ± 0.002	0.101 ± 0.027

From the fitted results presented in Table 20, it can be observed that as the number of layers increases and a compositional gradient is present in the heterostructures, the GaN (0002) peak shifts to lower values, approaching the expected unstrained value of 34.57° . Furthermore, the FWHM of the GaN (0002) peak decreases significantly with the addition of $\text{Al}_x\text{Ga}_{1-x}\text{N}$ layers, indicating higher crystalline quality and larger crystallites. Therefore, it can be concluded that for smoother composition variation, the GaN layer is more relaxed and has higher crystalline quality. However, the GaN sample without a buffer showed a peak position closer to the expected value, but the variation in FWHM and preferred orientation was a significant improvement on the samples.

Nonetheless, it is important to consider that increasing the number of layers also increases the deposition time, which is a crucial factor to consider for optimizing the production of these heterostructures.

4.3.2 UV-Vis analyses

UV-Vis transmission was performed on the GaN/ $\text{Al}_x\text{Ga}_{1-x}\text{N}$ heterostructures on glass substrates, and the spectra are shown in Figure 56. All samples show high values of transmission in the visible light range (~ 1.8 to 3.3 eV). The number of interference fringes

increases with the total thickness of the samples. The absorption edge of the heterostructures containing layers with the same Al content were in similar energy values. The absorption edge of samples H_B_120, H_B_150 and H_C_120 were in higher energy values, and they do not have an $\text{Al}_{0.07}\text{Ga}_{0.93}\text{N}$ layer. Similar, the absorption edge for samples H_A_37, H_A_120, H_A_150, and H_D_120 were in similar energy values, all containing an $\text{Al}_{0.07}\text{Ga}_{0.93}\text{N}$ layer.

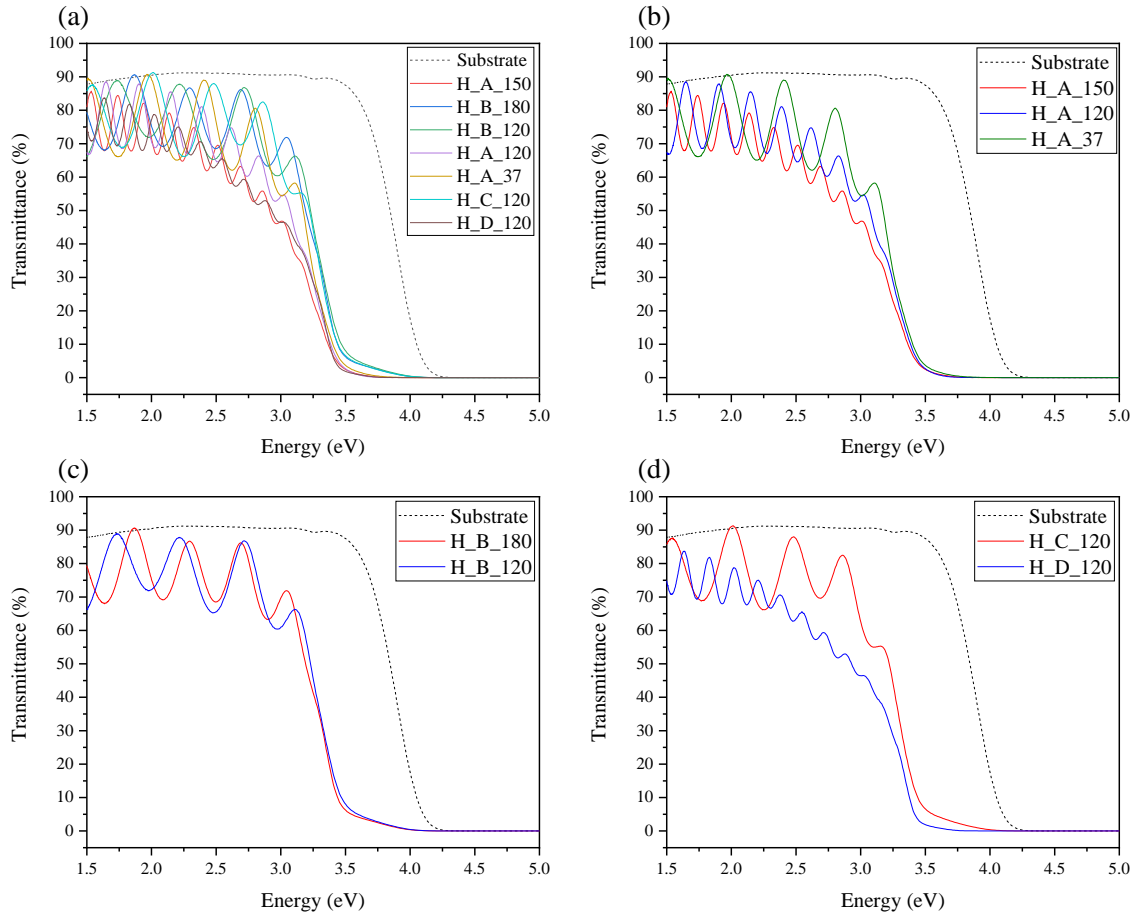


Figure 56: UV-Vis transmission spectra of (a) all the $\text{GaN}/\text{Al}_x\text{Ga}_{1-x}\text{N}$ samples, (b) the $\text{GaN}/\text{Al}_{0.07}\text{Ga}_{0.93}\text{N}$ samples, (c) the $\text{GaN}/\text{Al}_{0.37}\text{Ga}_{0.67}\text{N}$ samples, and (d) the multiple buffer samples.

The interference fringes for the $\text{GaN}/\text{Al}_x\text{Ga}_{1-x}\text{N}$ samples were not as uniform as those observed in the $\text{Al}_x\text{Ga}_{1-x}\text{N}$ films, due to the non-homogeneity of the composition along the thickness of the films. Some fluctuations in the fringes are expected due to the interference between the fringes of each layer with different composition, refractive index, and thickness. These fluctuations are clearer for samples H_B_120 and H_B_150, once they show an abrupt

variation of composition (from 37 % Al to 0 % Al) and somewhat visible for sample H_C_120, with a composition variation from 24 % Al to 0 % Al. The individual spectrum for all samples is shown in Appendix B.

Unlike the scenario with the $\text{Al}_x\text{Ga}_{1-x}\text{N}$ films, determining the bandgap of the heterostructures through UV-Vis results presents a challenge due to the intricate influence of multiple layers and the transmittance edge effects. To overcome this, calculating the bandgap of individual layers becomes essential. However, accomplishing this task through conventional UV-Vis measurements is unattainable, primarily because the layer with the smallest bandgap causes the transmittance to go down to zero, consequently concealing values of other layers. This effect can be observed as all T% curves show a decay at ~ 3.4 eV, which is the bandgap for GaN. In this context, spectroscopic ellipsometry emerges as a promising technique capable of unveiling the optical properties of individual layers.

4.3.3 Raman spectroscopy

The different GaN/ $\text{Al}_x\text{Ga}_{1-x}\text{N}$ /glass heterostructures were investigated using Raman spectroscopy. The Raman spectra of the heterostructures produced using a single $\text{Al}_{0.07}\text{Ga}_{0.93}\text{N}$ buffer layer with different deposition time (and thicknesses) are shown in Figure 57.

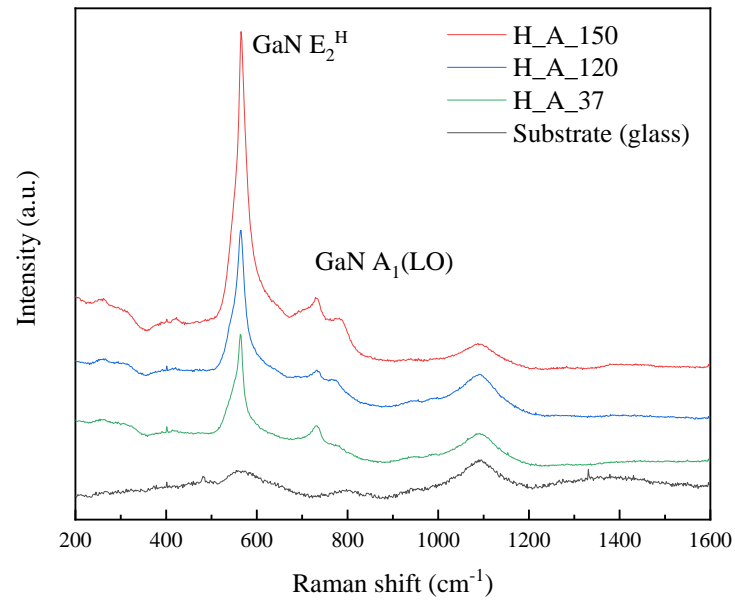


Figure 57: Raman spectra of the GaN/ $\text{Al}_{0.07}\text{Ga}_{0.93}\text{N}$ samples.

The increase in the intensity can be attributed to the thickness of the $\text{Al}_{0.07}\text{Ga}_{0.93}\text{N}$ layer, which contributes to the GaN E_2^{H} due to its position. The E_2^{H} and $\text{A}_1(\text{LO})$ modes are visible for all samples, confirming the presence of only wurtzite phase for the films. No significant difference can be seen in the position of the peaks between the samples with different thickness for the $\text{Al}_{0.07}\text{Ga}_{0.93}\text{N}$ layer, indicating that this feature does not seem to influence in strains of the films, which supports what was observed in the XRD analyses (Section 4.3.1.1). The samples with a single $\text{Al}_{0.37}\text{Ga}_{0.93}\text{N}$ layer, shown in Figure 58, however, show some differences from the samples with a single $\text{Al}_{0.07}\text{Ga}_{0.93}\text{N}$ layer.

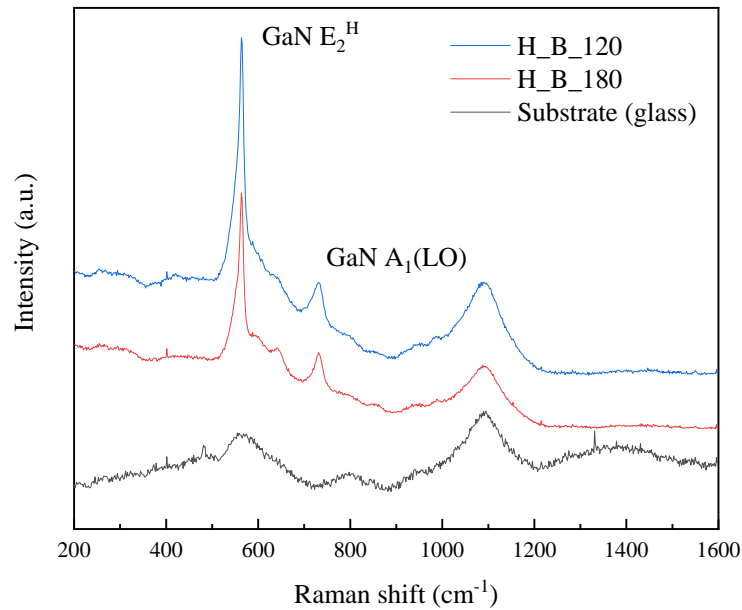


Figure 58: Raman spectra of the GaN/ $\text{Al}_{0.37}\text{Ga}_{0.63}\text{N}$ samples.

Again, only wurtzite peaks are visible. The GaN $A_1(\text{LO})$ peak is more distinct in the heterostructures using an Al-rich buffer layer (37 % Al), when compared to the ones using a buffer layer with 7 % Al (Figure 57). Also, the GaN E_2^{H} peak appears thinner, however in this case, the $\text{Al}_{0.37}\text{Ga}_{0.63}\text{N}$ E_2^{H} (samples H_B) is more shifted and does not highly contribute to the apparent thickness of the GaN peak (as discussed for the $\text{Al}_x\text{Ga}_{1-x}\text{N}$ samples in Section 4.2.4), in opposition to the samples with an $\text{Al}_{0.07}\text{Ga}_{0.93}\text{N}$ buffer (samples H_A). In good agreement to what was observed before, the thickness of the buffer layer did not influence in the GaN Raman shift. The Raman spectra for the heterostructures with multiple AlGa_N layers (double and triple buffer) are shown in Figure 59.

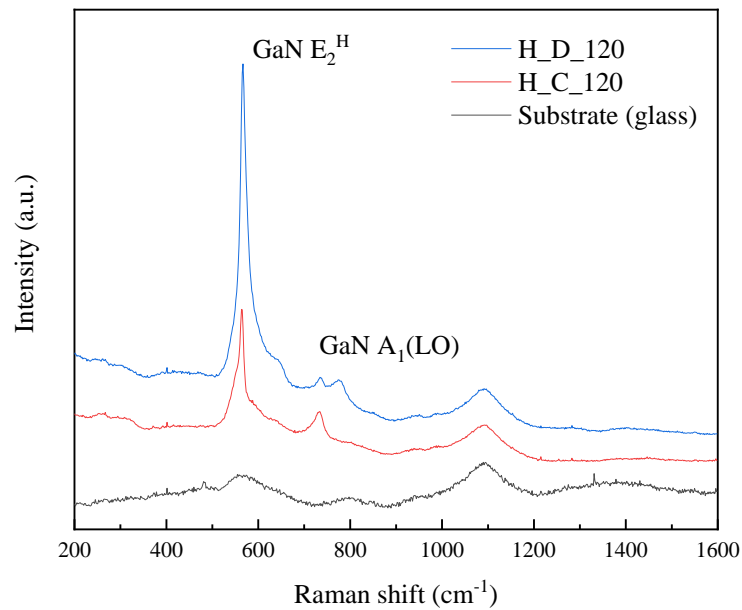


Figure 59: Raman spectra of the GaN/Al_xGa_{1-x}N samples with multiple AlGaN layers.

In the Raman spectra of Figure 59 the E₂^H and A₁(LO) modes can be observed. The presence of multiple peaks related to the different Al_xGa_{1-x}N composition of the buffer layers create an agglomeration in the E₂^H region, which impairs the observation of the peaks FWHM and precise position. Similar to what was observed for the single buffer layer samples, the E₂^H peak position coincides with the expected for GaN, showing that the main contribution to this peak is the GaN layer. This, together with the high intensity of this peak and quality of the Raman spectra, indicates a high quality of the GaN samples, confirming the XRD results. Sample H_D_120, which is composed of multiple layers forming a compositional gradient, shows very intense Raman signal, with a low FWHM for the E₂^H peak (approximately 14 cm⁻¹).

4.3.4 Scanning electron microscopy

Field emission gun scanning electron microscopy (FEG-SEM) was performed on the GaN/Al_xGa_{1-x}N heterostructures grown on Si (100) substrates and on the GaN sample S_0_60. Figure 60 shows the FEG-SEM images of the GaN/Si (100) sample without any AlGaN buffer layer.

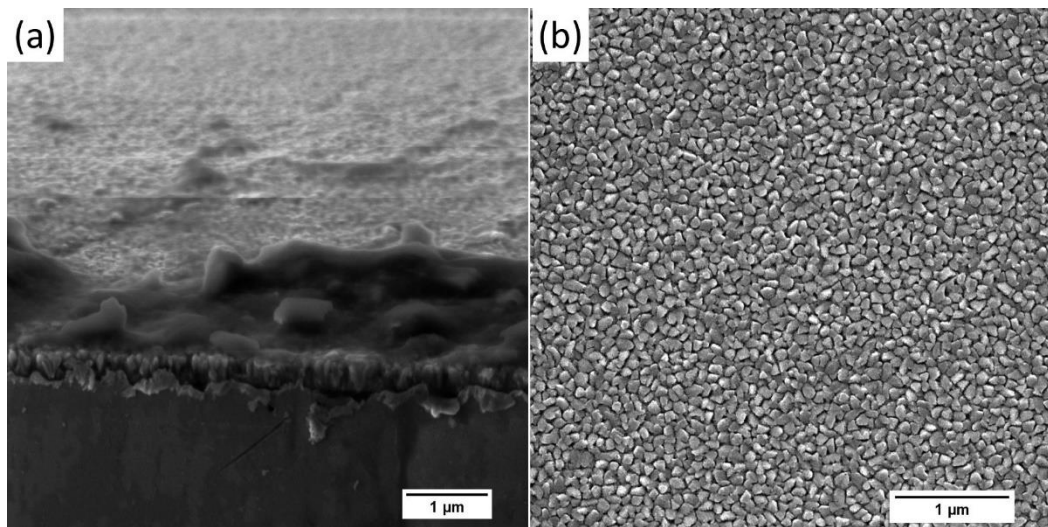


Figure 60: Cross-sectional and surface FEG-SEM images of the GaN sample.

The GaN film without an AlGaN buffer layer shows a columnar but highly disordered morphology observed on the cross-sectional image (Figure 60a), while the surface (Figure 60b) shows a homogeneous and well-defined morphology of finely agglomerated grains . Figure 61 shows the FEG-SEM images of the heterostructures with one $\text{Al}_{0.07}\text{Ga}_{0.93}\text{N}$ layer (low Al content) with varying thicknesses.

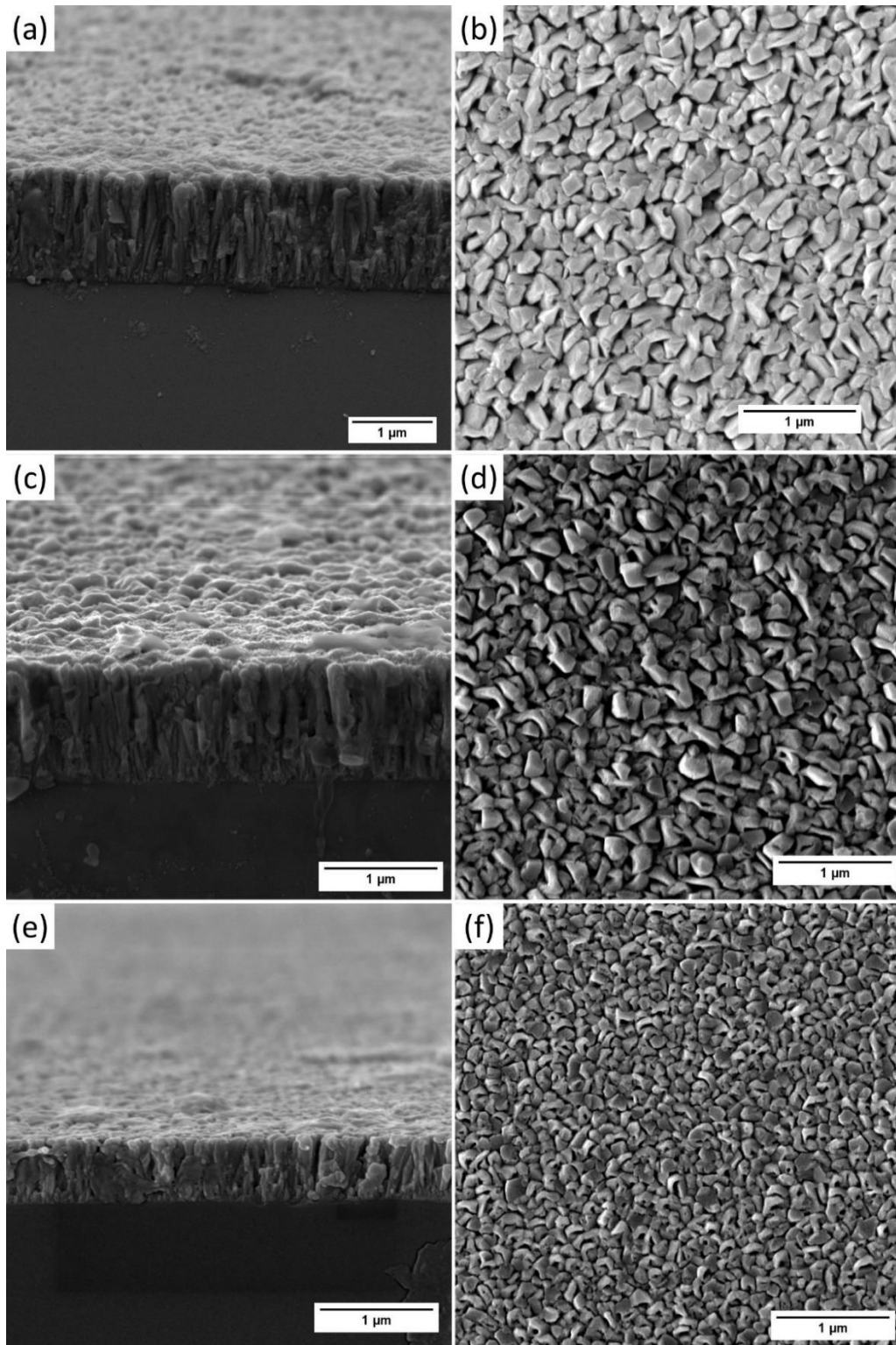


Figure 61: Cross-sectional and surface FEG-SEM images of the GaN/ $\text{Al}_{0.07}\text{Ga}_{0.93}\text{N}$ samples with an $\text{Al}_{0.07}\text{Ga}_{0.93}\text{N}$ layer thickness of approximately: (a) and (b) 1 μm, (c) and (d) 800 nm, and (e) and (f) 250 nm.

The FEG-SEM images of the GaN/Al_{0.07}Ga_{0.93}N films show an improvement on the columnar structure when compared to the GaN film without an AlGaN buffer layer (Figure 60). A surface with fine agglomerated grains in a gravel-like morphology with different sizes and shapes can be observed (Figure 61), similar to that the GaN sample. As the film thickness increases, the grains become larger, as shown in Figure 61b, d, and f, and the columns in the cross-sectional images become clearly organized (Figure 61a, c, and e). The same relationship with the grain size can be observed for the samples with an Al-rich layer in Figure 62.

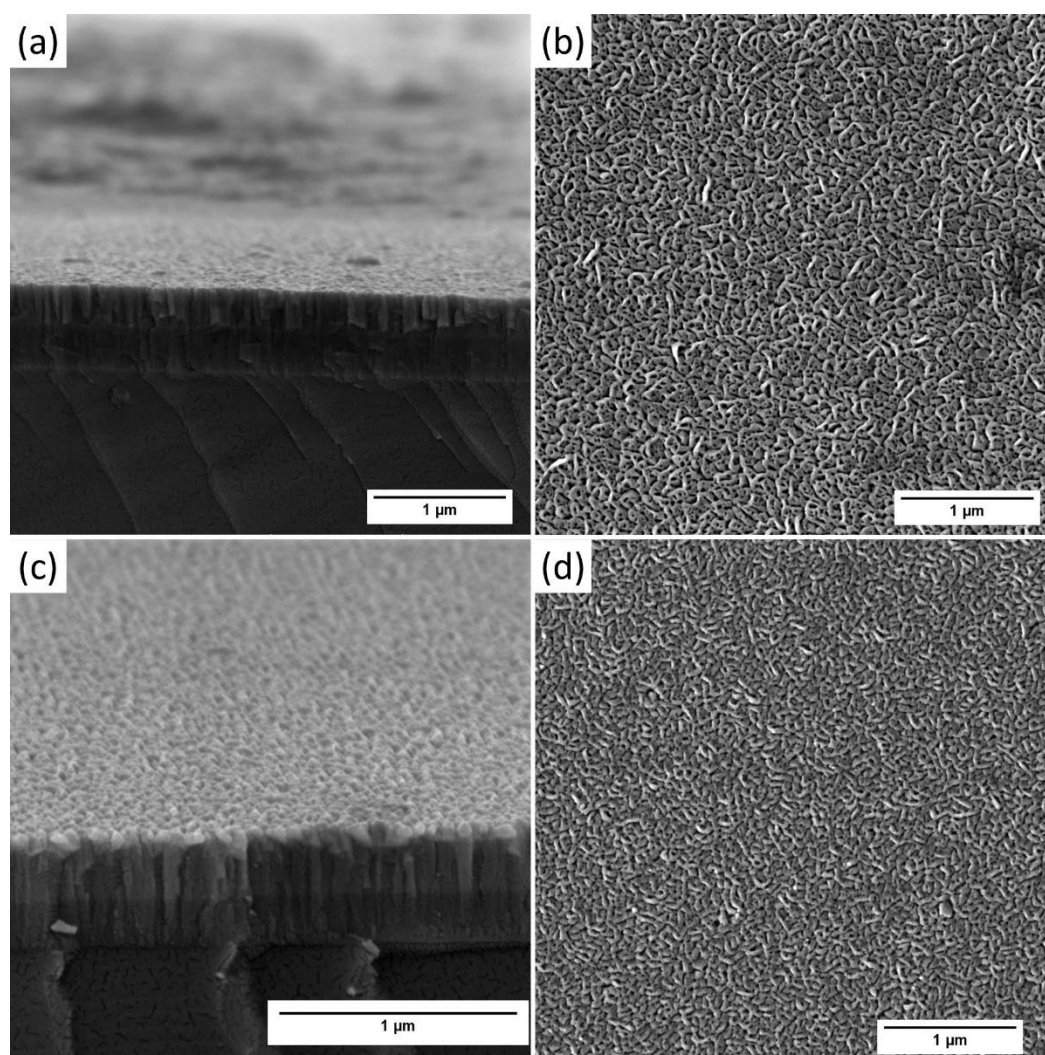


Figure 62: Cross-sectional and surface FEG-SEM images of the GaN/Al_{0.37}Ga_{0.63}N samples with an Al_{0.37}Ga_{0.63}N layer thickness of approximately: (a) and (b) 250 nm, and (c) and (d) 166 nm.

The heterostructures produced using an Al-rich layer showed a more organized columnar structure, with a surface morphology of fine elongated and continuous grains. The grain size on the surface of the films shows an increase with the thickness (Figure 62b and d), similar to the GaN/Al_{0.07}Ga_{0.93}N samples. Furthermore, a clear division between the GaN and Al_{0.37}Ga_{0.63}N layers can be observed in Figure 62a and c, which cannot be distinguished for the samples with low Al content, but is also observable in a recent study of GaN/AlGaN grown by MOCVD (GHOSH et al., 2023). This division between the layers with different composition can be related to the fluctuations of the interference fringes seen in the UV-Vis transmission spectra (Section 4.3.2). Comparing Figure 61 and Figure 62, it can be observed that an increase in Al content on the buffer layer induced significant changes in the morphology of the GaN films.

Figure 63 shows the SEM images of samples with multiple Al_xGa_{1-x}N layers forming a compositional gradient. It clearly shows that the thickness of the samples and the grain size of the GaN film increases with the number of layers.

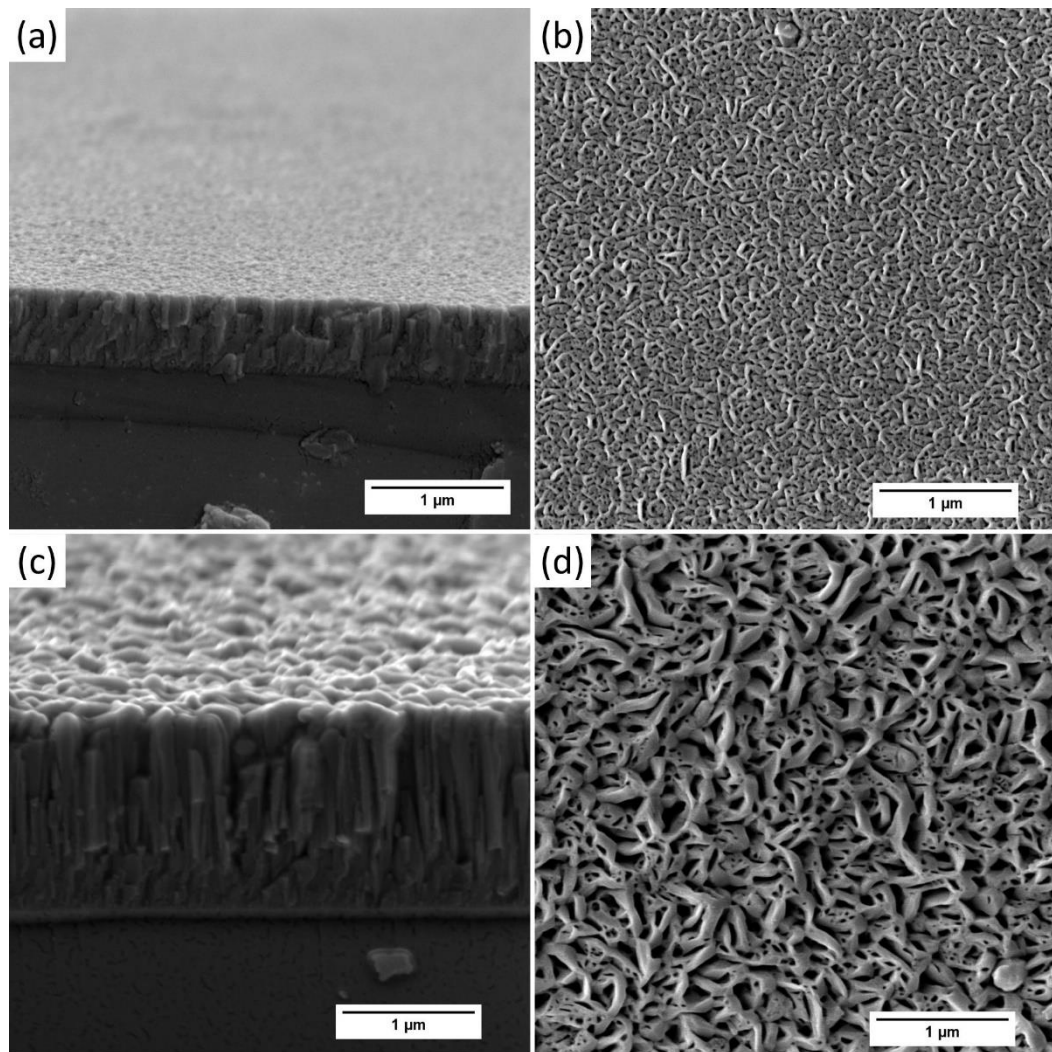


Figure 63: Cross-sectional and surface FEG-SEM images of the a) GaN/Al_{0.24}Ga_{0.76}N/Al_{0.37}Ga_{0.63}N and b) GaN/Al_{0.07}Ga_{0.63}N/Al_{0.24}Ga_{0.76}N/Al_{0.37}Ga_{0.63}N heterostructures.

The sample with double AlGaN buffer layer (Figure 63a and b) displays a morphology similar to what was observed for the sample with Al_{0.37}Ga_{0.63}N buffer layer. However, the sample with a triple buffer layer displays a highly ordered columnar growth (Figure 63c), and the surface is composed of a porous surface with quasi-continuous grains. A similar morphology was observed in epitaxial (0001) GaN films using sapphire substrates with AlN or GaN buffer produced by MOCVD (BILOUSOV et al., 2014).

Figure 64 shows the surface of the GaN film and GaN/AlGaN heterostructures obtained using a low magnification (10 or 20 kx). From these images it can be observed the uniformity

of the films' surface without cracks. The heterostructure with a triple buffer layer (Figure 64d) shows a very smooth surface, free of any defects. The FEG-SEM of the surface of the other samples are shown in Appendix C.

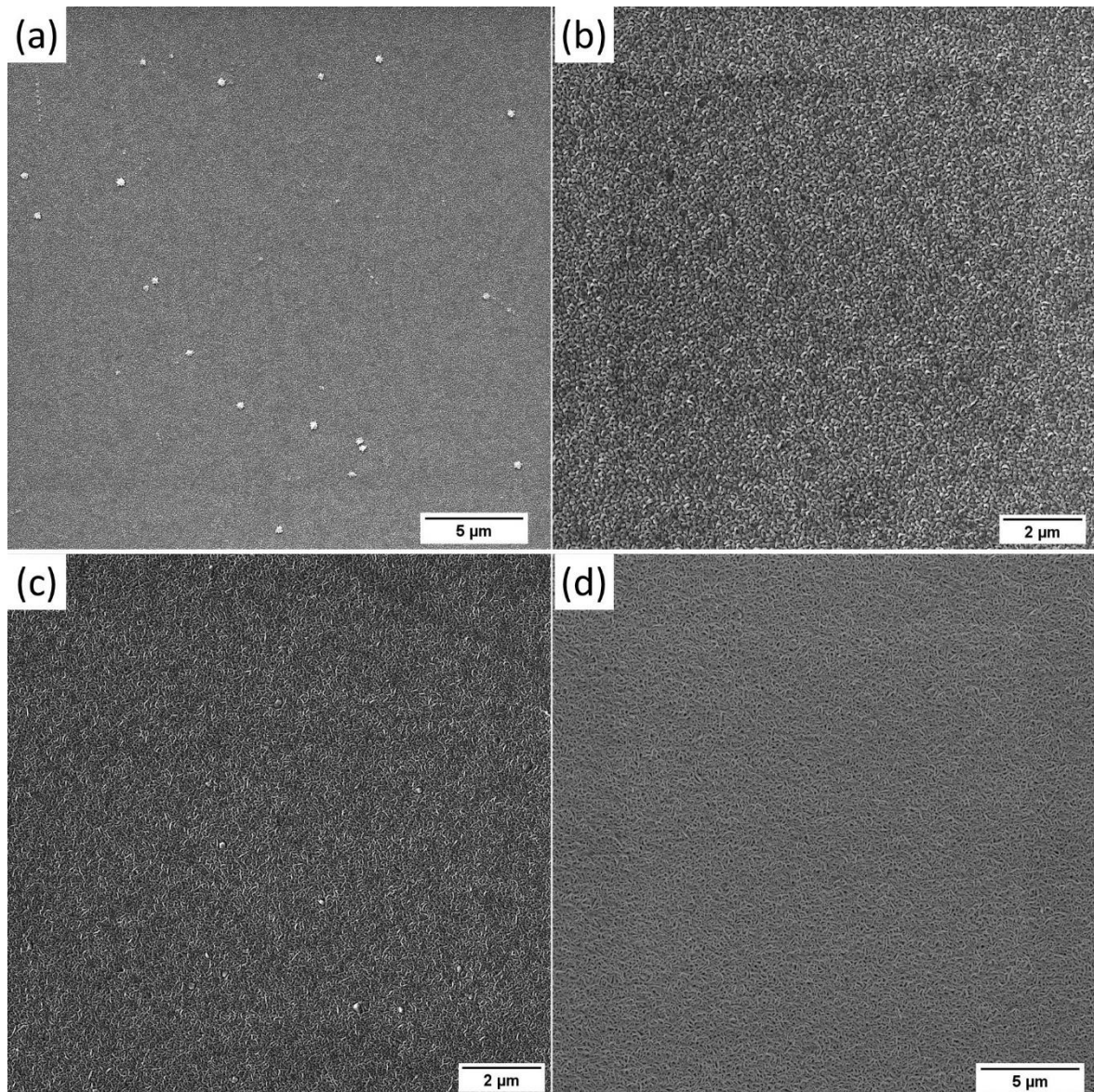


Figure 64: Surface FEG-SEM images of (a) GaN without buffer layer, (b) GaN/Al_{0.07}Ga_{0.93}N heterostructure, (c) GaN/Al_{0.37}Ga_{0.63}N heterostructure, and (d) GaN/Al_{0.07}Ga_{0.63}N/Al_{0.24}Ga_{0.76}N/Al_{0.37}Ga_{0.63}N heterostructure.

5 Conclusions

The deposition of $\text{Al}_x\text{Ga}_{1-x}\text{N}$ films with different x values using magnetron sputtering showed that the Al content had a significant influence on the properties of the films. In general, the increase in Al content showed to improve the crystalline quality of the samples. Additionally, the different substrates exhibited different behaviors for the samples. More specifically:

- The composition was homogeneous in different spots of the samples, and it was fairly similar between the different substrates (silicon and glass were compared);
- The increase in Al content in the films influenced the production of more c -axis oriented samples for all substrates. The glass substrate samples had more pronounced and isolated (0002) peaks when compared to the Si substrate samples, which were similar to each other;
- The increase in Al content also led to a shift in the (0002) peak position and variation of the lattice parameters a and c . The deviation of the peak position from the unstrained expected one increased with Al content. This behavior was associated with strains in the structure and led to overestimation of the Al content using XRD analyses in comparison to EDS measurements;
- The films produced on the glass substrates showed lower strain values compared to the Si substrates, and no significant difference was observed between the different Si orientation substrates;
- The FWHM of the (0002) peak was fairly similar between the samples on different Si substrates, but generally lower than those on the glass substrate, especially for low Al content. In those cases, the Si substrate samples showed more pronounced and sharper (0002) peaks, indicating better structural quality and larger crystallites;
- The thickness of the samples appears to have a significant impact on the FWHM of the (0002) peak. Therefore, the samples with low Al content produced using higher power on the Ga target, i.e., thicker samples, showed a better relationship between low strains and low FWHM. For the samples with more pronounced

c-axis orientation, those with higher Al content exhibited better results and more relatively intense (0002) peaks;

- The bandgap and static refractive index varied with the composition of the samples. The refractive index decreased with the increase in the power of the Al target (and the increase in Al content as a consequence). The bandgap increased with the increase in Al content, as expected for tunable bandgap alloys such as AlGaIn;
- Raman spectra showed the E_2^H and $A_1(LO)$ phonon modes for all the glass substrate samples that were analyzed. The $A_1(LO)$ peak shifted with Al content, as expected from the literature. The E_2^H peak also showed a similar behavior to that described in other studies: a shift occurred as the composition of the $Al_xGa_{1-x}N$ samples changed, and the peaks became broader and more difficult to distinguish. Additionally, a shoulder appeared for compositions with $x > 0.36$.

The conclusions above about the AlGaIn samples led to the selection of the buffer layer, considering both the Al content and the deposition parameters (the power applied to the Al and Ga targets). This decision was based on using films with different Al content, all of which demonstrated good quality for the buffer.

For the GaN/ $Al_xGa_{1-x}N$ heterostructures, the results showed that the Al content in the $Al_xGa_{1-x}N$ buffer layer significantly influenced the quality of the GaN film. Increasing the Al content led to more *c*-oriented GaN films, with a high relative intensity for the (0002) peak. Additionally, samples with an Al-rich buffer exhibited a smoother surface, characterized by a highly organized columnar growth of the films.

The thickness of the buffer layer did not appear to influence the GaN crystalline properties within the studied range. Regardless of the thickness, GaN samples with the same composition of the buffer layer displayed similar characteristics of *c*-axis orientation and crystalline quality. However, increasing the buffer layer thickness (and the total thickness of the samples) resulted in larger grains in the films, without altering their morphology, as observed by SEM.

A compositional gradient for the buffer layer also proved to improve some of the film's properties, albeit with an increase in deposition time and complexity of the sample production.

The addition of a number of buffer layers in a compositional gradient led to a slight improvement in crystalline quality. In terms of the film's morphology, the addition of a gradient resulted in highly organized columns and a quasi-continuous grain in the surface, similar to what is observed in epitaxial films. Overall, the general quality and uniformity of the surface were also improved.

6 Published works

The following works are result of the studies in this thesis:

HORTA, I. M.; DAMASCENO, B. S.; DE OLIVEIRA, R. S.; PEREIRA, A. L. J.; MASSI, M.; SOBRINHO, A. S. S.; LEITE, D. M. G. AlGa_N films grown by reactive magnetron sputtering on glass substrates with different Al content. SURFACES AND INTERFACES, v. 40, p. 103023, 2023.

HORTA, I. M.; PEREIRA, A. L. J.; LEITE, D. M. G. Deposition and characterization of AlGa_N films produced using reactive magnetron sputtering. In: 13^of Workshop em Engenharia e Tecnologia Espaciais, 2022, São José dos Campos. Artigos do 13^o Workshop em Engenharia e Tecnologia Espaciais, 2022.

HORTA, I. M.; DE OLIVEIRA, R. S.; DAMASCENO, B. S.; PEREIRA, A. L. J.; LEITE, D. M. G. Characterization of GaN/Si films using spectroscopic ellipsometry and Raman spectroscopy. 2021. (Work presented at the XIX Brazilian MRS Meeting).

HORTA, I. M.; DAMASCENO, B. S.; DE OLIVEIRA, R. S.; SOBRINHO, A. S. S.; PEREIRA, A. L. J. ; LEITE, D. M. G. Production and characterization of Al_xGa_{1-x}N films by reactive dual magnetron sputtering. 2023 (Work presented at the XX Brazilian MRS Meeting).

7 Recommendations

The author suggests future works that would build upon this study to gain a better understanding of the material and enhance the research in the following ways:

- Deepen the XRD analyses by conducting rocking curve (omega scan) and pole figure measurements to accurately assess the preferred orientation and texture degree of the samples. Analyzing intensity variations alone may lead to misinterpretations due to the influence of lattice defects on the intensity (RAMADAN et al., 2009);
- Perform spectroscopic ellipsometry on the Si substrate samples to obtain optical properties such as refractive index, absorption coefficient, and bandgap. This technique can also be utilized to fit the chemical composition of the films. Spectroscopic ellipsometry is a powerful tool capable of providing much more accurate measurements compared to UV-Vis spectrophotometry, and it can be conducted on Si substrates. Additionally, ellipsometry can be employed on the heterostructure samples to obtain the optical properties of the individual layers;
- Reduce the step size between each buffer layer composition to create a smoother compositional gradient with proportional thicknesses. This can be achieved by either implementing discrete steps with varying power applied to each target and adjusting the deposition time for each layer or by employing continuous variation in an automated system.

8 References

ANGERER, H. et al. Determination of the Al mole fraction and the band gap bowing of epitaxial $\text{Al}_x\text{Ga}_{1-x}\text{N}$ films. **Applied Physics Letters**, [S. l.], v. 71, n. 11, p. 1504–1506, 1997. DOI: 10.1063/1.119949. Available on: <http://aip.scitation.org/doi/10.1063/1.119949>.

ARIFIN, Pepen; SUTANTO, Heri; SUGIANTO; SUBAGIO, Agus. Plasma-Assisted MOCVD Growth of Non-Polar GaN and AlGa_N on Si(111) Substrates Utilizing GaN-AlN Buffer Layer. **Coatings**, [S. l.], v. 12, n. 1, p. 94, 2022. DOI: 10.3390/coatings12010094. Available on: <https://www.mdpi.com/2079-6412/12/1/94>.

BACA, Justin; SEVERNS, Virginia; LOVATO, Debbie; BRANCH, Darren; LARSON, Richard. Rapid Detection of Ebola Virus with a Reagent-Free, Point-of-Care Biosensor. **Sensors (Basel, Switzerland)**, [S. l.], v. 15, p. 8605–8614, 2015. DOI: 10.3390/s150408605.

BARTOLI, F. et al. AlN/GaN/Sapphire heterostructure for high-temperature packageless acoustic wave devices. **Sensors and Actuators A: Physical**, [S. l.], v. 283, p. 9–16, 2018. DOI: 10.1016/j.sna.2018.08.011. Available on: <https://linkinghub.elsevier.com/retrieve/pii/S0924424718305971>.

BERNARDINI, Fabio; FIORENTINI, Vincenzo. Nonlinear macroscopic polarization in III-V nitride alloys. **Physical Review B**, [S. l.], v. 64, n. 8, p. 085207, 2001. DOI: 10.1103/PhysRevB.64.085207. Available on: <https://link.aps.org/doi/10.1103/PhysRevB.64.085207>.

BHAT, Aasif Mohammad; POONIA, Ritu; VARGHESE, Arathy; SHAFI, Nawaz; PERIASAMY, C. AlGa_N/GaN high electron mobility transistor for various sensing applications: A review. **Micro and Nanostructures**, [S. l.], v. 176, p. 207528, 2023. DOI: 10.1016/j.micrna.2023.207528. Available on: <https://linkinghub.elsevier.com/retrieve/pii/S2773012323000250>.

BILOUSOV, Oleksandr V.; CARVAJAL, Joan J.; MENA, Josué; MARTÍNEZ, Oscar; JIMÉNEZ, Juan; GEANEY, Hugh; DÍAZ, Francesc; AGUILÓ, Magdalena; O'DWYER, Colm. Epitaxial growth of (0001) oriented porous GaN layers by chemical vapour deposition. **CrystEngComm**, [S. l.], v. 16, n. 44, p. 10255–10261, 2014. DOI: 10.1039/C4CE01339E. Available on: <http://xlink.rsc.org/?DOI=C4CE01339E>.

BRUNNER, D.; ANGERER, H.; BUSTARRET, E.; FREUDENBERG, F.; HÖPLER,

R.; DIMITROV, R.; AMBACHER, O.; STUTZMANN, M. Optical constants of epitaxial AlGa_N films and their temperature dependence. **Journal of Applied Physics**, [S. l.], v. 82, n. 10, p. 5090–5096, 1997. DOI: 10.1063/1.366309.

CAPPUCCIO, G.; TERRANOVA, M. L. **Thin film characterisation by advanced X-ray diffraction techniques**, 1996. Available on: https://inis.iaea.org/search/search.aspx?orig_q=RN:28044496.

CHANG, Chen-Te; YANG, Yung-Chin; LEE, Jyh-Wei; LOU, Bih-Show. The influence of deposition parameters on the structure and properties of aluminum nitride coatings deposited by high power impulse magnetron sputtering. **Thin Solid Films**, [S. l.], v. 572, p. 161–168, 2014. DOI: 10.1016/j.tsf.2014.09.007. Available on: <https://linkinghub.elsevier.com/retrieve/pii/S0040609014008840>.

CHENG, H.; SUN, Y.; ZHANG, J. ...; ZHANG, Y. ...; YUAN, S.; HING, P. AlN films deposited under various nitrogen concentrations by RF reactive sputtering. **Journal of Crystal Growth**, [S. l.], v. 254, n. 1–2, p. 46–54, 2003. DOI: 10.1016/S0022-0248(03)01176-X. Available on: <https://linkinghub.elsevier.com/retrieve/pii/S002202480301176X>.

DADGAR, A. et al. Epitaxy of GaN on silicon - Impact of symmetry and surface reconstruction. **New Journal of Physics**, [S. l.], v. 9, n. May, 2007. DOI: 10.1088/1367-2630/9/10/389.

DAVYDOV, V. Yu. et al. Phonon dispersion and Raman scattering in hexagonal GaN and AlN. **Physical Review B**, [S. l.], v. 58, n. 19, p. 12899–12907, 1998. DOI: 10.1103/PhysRevB.58.12899. Available on: <https://link.aps.org/doi/10.1103/PhysRevB.58.12899>.

DAVYDOV, Yu V. et al. Composition dependence of optical phonon energies and Raman line broadening in hexagonal Al_xGa_{1-x}N alloys. **Physical Review B - Condensed Matter and Materials Physics**, [S. l.], v. 65, n. 12, p. 1–13, 2002. DOI: 10.1103/PhysRevB.65.125203. Available on: https://www.researchgate.net/publication/239290889_Composition_dependence_of_optical_phonon_energies_and_Raman_line_broadening_in_hexagonal_AlxGa1-xN_alloys.

DEPLA, D.; DE GRYSSE, R. Target poisoning during reactive magnetron sputtering: Part I: the influence of ion implantation. **Surface and Coatings Technology**, [S. l.], v. 183, n. 2–3, p. 184–189, 2004. DOI: 10.1016/j.surfcoat.2003.10.006. Available on:

<https://linkinghub.elsevier.com/retrieve/pii/S0257897203011344>.

DEPLA, D.; MAHIEU, S.; DE GRYSSE, R. Magnetron sputter deposition: Linking discharge voltage with target properties. **Thin Solid Films**, [*S. l.*], v. 517, n. 9, p. 2825–2839, 2009. DOI: 10.1016/j.tsf.2008.11.108. Available on: <https://linkinghub.elsevier.com/retrieve/pii/S0040609008015149>.

DU, Chao; ZHAO, Yali; LI, Yong. Effect of Surface Cleaning Process on the Wafer Bonding of Silicon and Pyrex Glass. **Journal of Inorganic and Organometallic Polymers and Materials**, [*S. l.*], v. 33, n. 3, p. 673–679, 2023. DOI: 10.1007/s10904-022-02510-x. Available on: <https://link.springer.com/10.1007/s10904-022-02510-x>.

DUQUENNE, C.; DJOUADI, M. A.; TESSIER, P. Y.; JOUAN, P. Y.; BESLAND, M. P.; BRYLINSKI, C.; AUBRY, R.; DELAGE, S. Epitaxial growth of aluminum nitride on AlGa_N by reactive sputtering at low temperature. **Applied Physics Letters**, [*S. l.*], v. 93, n. 5, p. 052905, 2008. DOI: 10.1063/1.2967816. Available on: <http://aip.scitation.org/doi/10.1063/1.2967816>.

FENG, Yining; SARAVADE, Vishal; CHUNG, Ting-Fung; DONG, Yongqi; ZHOU, Hua; KUCUKGOK, Bahadir; FERGUSON, Ian T.; LU, Na. Strain-stress study of Al_xGa_{1-x}N/AlN heterostructures on c-plane sapphire and related optical properties. **Scientific Reports**, [*S. l.*], v. 9, n. 1, p. 10172, 2019. DOI: 10.1038/s41598-019-46628-4. Available on: <http://www.nature.com/articles/s41598-019-46628-4>.

FEYNMAN, Richard Phillips; LEIGHTON, Robert Benjamin; SANDS, Matthew Linzee. **The Feynman Lectures on Physics**. 50. ed. [s.l.: s.n.].

FURQAN, C. M.; HO, Jacob Y. L.; KWOK, H. S. GaN thin film: Growth and Characterizations by Magnetron Sputtering. **Surfaces and Interfaces**, [*S. l.*], v. 26, p. 101364, 2021. DOI: 10.1016/j.surfin.2021.101364. Available on: <https://linkinghub.elsevier.com/retrieve/pii/S2468023021004417>.

GHOSH, Saptarsi; HINZ, Alexander M.; FRENTRUP, Martin; ALAM, Saiful; WALLIS, David J.; OLIVER, Rachel A. Design of step-graded AlGa_N buffers for GaN-on-Si heterostructures grown by MOCVD. **Semiconductor Science and Technology**, [*S. l.*], v. 38, n. 4, p. 044001, 2023. DOI: 10.1088/1361-6641/acb9b6. Available on: <https://iopscience.iop.org/article/10.1088/1361-6641/acb9b6>.

GUDMUNDSSON, J. T. Physics and technology of magnetron sputtering discharges.

Plasma Sources Science and Technology, [*S. l.*], v. 29, n. 11, p. 113001, 2020. DOI: 10.1088/1361-6595/abb7bd. Available on: <https://iopscience.iop.org/article/10.1088/1361-6595/abb7bd>.

GUO, Qixin; NISHIO, Mitsuhiro; OGAWA, Hiroshi. Recent progress on low-temperature epitaxial growth of nitride semiconductors. *In*: (Jinfa Tang, Chao-Nan Xu, Haizhang Li, Org.) 2000, **Anais** [...]. [s.l: s.n.] p. 361. DOI: 10.1117/12.401686. Available on: <http://proceedings.spiedigitallibrary.org/proceeding.aspx?doi=10.1117/12.401686>.

HAN, Sang-Woo; NOH, Youngkyun; JO, Min-Gi; KIM, Seung-Hwan; OH, Jae-Eung; SEO, Kwang-Seok; CHA, Ho-Young. Normally-Off MOS-HFET on AlGaIn/GaN-on-Si(110) Grown by NH₃ MBE. **IEEE Electron Device Letters**, [*S. l.*], v. 37, n. 12, p. 1613–1616, 2016. DOI: 10.1109/LED.2016.2621184. Available on: <http://ieeexplore.ieee.org/document/7676266/>.

HARIMA, Hiroshi. Properties of GaN and related compounds studied by means of Raman scattering. **Journal of Physics: Condensed Matter**, [*S. l.*], v. 14, n. 38, p. R967–R993, 2002. DOI: 10.1088/0953-8984/14/38/201. Available on: <https://iopscience.iop.org/article/10.1088/0953-8984/14/38/201>.

HENRY, T. A.; ARMSTRONG, A.; ALLERMAN, A. A.; CRAWFORD, M. H. The influence of Al composition on point defect incorporation in AlGaIn. **Applied Physics Letters**, [*S. l.*], v. 100, n. 4, p. 043509, 2012. DOI: 10.1063/1.3679681. Available on: <http://aip.scitation.org/doi/10.1063/1.3679681>.

HORTA, Isabela Machado; DAMASCENO, Barbara Souza; DE OLIVEIRA, Regiane Santana; PEREIRA, André Luis de Jesus; MASSI, Marcos; SOBRINHO, Argemiro Soares da Silva; LEITE, Douglas Marcel Gonçalves. AlGaIn films grown by reactive magnetron sputtering on glass substrates with different Al content. **Surfaces and Interfaces**, [*S. l.*], p. 103023, 2023. DOI: 10.1016/j.surfin.2023.103023. Available on: <https://linkinghub.elsevier.com/retrieve/pii/S2468023023003930>.

HWANG, Bing-Hwai; CHEN, Chi-Shan; LU, Hong-Yang; HSU, Tzu-Chien. Growth mechanism of reactively sputtered aluminum nitride thin films. **Materials Science and Engineering: A**, [*S. l.*], v. 325, n. 1–2, p. 380–388, 2002. DOI: 10.1016/S0921-5093(01)01477-0. Available on: <https://linkinghub.elsevier.com/retrieve/pii/S0921509301014770>.

IQBAL, Abid; MOHD-YASIN, Faisal. Reactive Sputtering of Aluminum Nitride (002) Thin Films for Piezoelectric Applications: A Review. **Sensors**, [S. l.], v. 18, n. 6, p. 1797, 2018. DOI: 10.3390/s18061797. Available on: <http://www.mdpi.com/1424-8220/18/6/1797>.

IRIARTE, G. F.; RODRÍGUEZ, J. G.; CALLE, F. Synthesis of c-axis oriented AlN thin films on different substrates: A review. **Materials Research Bulletin**, [S. l.], v. 45, n. 9, p. 1039–1045, 2010. DOI: 10.1016/j.materresbull.2010.05.035. Available on: <https://linkinghub.elsevier.com/retrieve/pii/S0025540810002023>.

JAGANNADHAM, K.; SHARMA, A. K.; WEI, Q.; KALYANRAMAN, R.; NARAYAN, J. Structural characteristics of AlN films deposited by pulsed laser deposition and reactive magnetron sputtering: A comparative study. **Journal of Vacuum Science & Technology A: Vacuum, Surfaces, and Films**, [S. l.], v. 16, n. 5, p. 2804–2815, 1998. DOI: 10.1116/1.581425. Available on: <https://pubs.aip.org/jva/article/16/5/2804/383406/Structural-characteristics-of-AlN-films-deposited>.

JAMES HOWARD EDGAR. **Properties, processing and applications of gallium nitride and related semiconductors**. [s.l: s.n.].

JANG, Gil Su; AHN, Seon Mi; HWANG, Nong-Moon. Effects of Sputtering Power, Working Pressure, and Electric Bias on the Deposition Behavior of Ag Films during DC Magnetron Sputtering Considering the Generation of Charged Flux. **Electronic Materials Letters**, [S. l.], v. 18, n. 1, p. 57–68, 2022. DOI: 10.1007/s13391-021-00314-8. Available on: <https://link.springer.com/10.1007/s13391-021-00314-8>.

JAYASAKTHI, M. et al. Effect of Al-mole fraction in Al_xGa_{1-x}N grown by MOCVD. In: 2014, **Anais** [...]. [s.l: s.n.] p. 1458–1460. DOI: 10.1063/1.4872995. Available on: <http://aip.scitation.org/doi/abs/10.1063/1.4872995>.

JIANG, H.; ZHAO, G. Y.; ISHIKAWA, H.; EGAWA, T.; JIMBO, T.; UMENO, M. Determination of exciton transition energy and bowing parameter of AlGa_N alloys in AlGa_N/Ga_N heterostructure by means of reflectance measurement. **Journal of Applied Physics**, [S. l.], v. 89, n. 2, p. 1046–1052, 2001. DOI: 10.1063/1.1334923. Available on: <http://aip.scitation.org/doi/10.1063/1.1334923>.

JIANG, Ying et al. SAW sensor for Influenza A virus detection enabled with efficient surface functionalization. **Sensors and Actuators, B: Chemical**, [S. l.], v. 209, p. 78–84, 2015. DOI: 10.1016/j.snb.2014.11.103. Available on: <http://dx.doi.org/10.1016/j.snb.2014.11.103>.

JUNAID, Muhammad; HSIAO, Ching Lien; CHEN, Yen Ting; LU, Jun; PALISAITIS, Justinas; PERSSON, Per Ola Åke; HULTMAN, Lars; BIRCH, Jens. Effects of N₂ partial pressure on growth, structure, and optical properties of GaN nanorods deposited by liquid-target reactive magnetron sputter epitaxy. **Nanomaterials**, [S. l.], v. 8, n. 4, 2018. DOI: 10.3390/nano8040223.

KE, Genshui; TAO, Yuan; LU, Yisheng; BIAN, Yingbin; ZHU, Tao; GUO, Haibo; CHEN, Yigang. Highly c-axis oriented AlN film grown by unbalanced magnetron reactive sputtering and its electrical properties. **Journal of Alloys and Compounds**, [S. l.], v. 646, p. 446–453, 2015. DOI: 10.1016/j.jallcom.2015.05.174. Available on: <https://linkinghub.elsevier.com/retrieve/pii/S0925838815300736>.

KELLY, P. ..; ARNELL, R. .. Magnetron sputtering: a review of recent developments and applications. **Vacuum**, [S. l.], v. 56, n. 3, p. 159–172, 2000. DOI: 10.1016/S0042-207X(99)00189-X. Available on: <https://linkinghub.elsevier.com/retrieve/pii/S0042207X9900189X>.

KOIDE, Y.; ITOH, H.; KHAN, M. R. H.; HIRAMATU, K.; SAWAKI, N.; AKASAKI, I. Energy band-gap bowing parameter in an Al_xGa_{1-x}N alloy. **Journal of Applied Physics**, [S. l.], v. 61, n. 9, p. 4540–4543, 1987. DOI: 10.1063/1.338387. Available on: <http://aip.scitation.org/doi/10.1063/1.338387>.

KORAKAKIS, D.; NG, H. M.; MISRA, M.; GRIESHABER, W.; MOUSTAKAS, T. D. Growth and Doping of AlGa_N Alloys by ECR-assisted MBE. **MRS Internet Journal of Nitride Semiconductor Research**, [S. l.], v. 1, p. e10, 1996. DOI: 10.1557/S1092578300001824. Available on: <https://linkinghub.elsevier.com/retrieve/pii/S0079672718300302>.

LEE, Sang-Min; JOO, Young-Hee; KIM, Chang-Il. Influences of film thickness and annealing temperature on properties of sol–gel derived ZnO–SnO₂ nanocomposite thin film. **Applied Surface Science**, [S. l.], v. 320, p. 494–501, 2014. DOI: 10.1016/j.apsusc.2014.09.099. Available on: <https://linkinghub.elsevier.com/retrieve/pii/S016943321402090X>.

LEITE, D. M. G.; LI, T.; DEVILLERS, T.; SCHIABER, Z. S.; LISBOA-FILHO, P. N.; BONANNI, A.; DIAS DA SILVA, J. H. Columnar microstructure of nanocrystalline Ga_{1-x}Mn_xN films deposited by reactive sputtering. **Journal of Crystal Growth**, [S. l.], v.

327, n. 1, p. 209–214, 2011. DOI: 10.1016/j.jcrysgro.2011.05.012. Available on: <https://linkinghub.elsevier.com/retrieve/pii/S0022024811004702>.

LESZCZYNSKI, M. et al. Lattice parameters of gallium nitride. **Applied Physics Letters**, [*S. l.*], v. 69, n. 1, p. 73–75, 1996. DOI: 10.1063/1.118123.

LI, Jie et al. Facilitating Complex Thin Film Deposition by Using Magnetron Sputtering: A Review. **JOM**, [*S. l.*], v. 74, n. 8, p. 3069–3081, 2022. DOI: 10.1007/s11837-022-05294-0. Available on: <https://link.springer.com/10.1007/s11837-022-05294-0>.

LI, Tao et al. Influence of pressure on the properties of AlN deposited by DC reactive magnetron sputtering on Si (100) substrate. **Micro & Nano Letters**, [*S. l.*], v. 14, n. 2, p. 146–149, 2019. DOI: 10.1049/mnl.2018.5293. Available on: <https://onlinelibrary.wiley.com/doi/10.1049/mnl.2018.5293>.

LI, Zhenhua et al. Plasma assisted molecular beam epitaxy growth mechanism of AlGa_N epilayers and strain relaxation on AlN templates. **Japanese Journal of Applied Physics**, [*S. l.*], v. 60, n. 7, p. 075504, 2021. DOI: 10.35848/1347-4065/ac0bed. Available on: <http://aip.scitation.org/doi/10.1063/1.123339>.

LIM, Ki Seong; KIM, Young Seok; HONG, Sung Hwan; SONG, Gian; KIM, Ki Buem. Influence of N₂ Gas Flow Ratio and Working Pressure on Amorphous Mo–Si–N Coating during Magnetron Sputtering. **Coatings**, [*S. l.*], v. 10, n. 1, p. 34, 2020. DOI: 10.3390/coatings10010034. Available on: <https://www.mdpi.com/2079-6412/10/1/34>.

LIU, L.; EDGAR, J. H. Substrates for gallium nitride epitaxy. **Materials Science and Engineering: R: Reports**, [*S. l.*], v. 37, n. 3, p. 61–127, 2002. DOI: 10.1016/S0927-796X(02)00008-6. Available on: <https://linkinghub.elsevier.com/retrieve/pii/S0927796X02000086>.

LU, Yuan; LIU, Xianglin; WANG, Xiaohui; LU, Da Cheng; LI, Dabing; HAN, Xiuxun; CONG, Guangwei; WANG, Zhanguo. Influence of the growth temperature of the high-temperature AlN buffer on the properties of GaN grown on Si(1 1 1) substrate. **Journal of Crystal Growth**, [*S. l.*], v. 263, n. 1–4, p. 4–11, 2004. DOI: 10.1016/j.jcrysgro.2003.11.001.

MANDAL, Debdyuti; BANERJEE, Sourav. Surface Acoustic Wave (SAW) Sensors: Physics, Materials, and Applications. **Sensors**, [*S. l.*], v. 22, n. 3, p. 820, 2022. DOI: 10.3390/s22030820. Available on: <https://www.mdpi.com/1424-8220/22/3/820>.

MANDAL, Pramod; SINGH, Udai P.; ROY, Sudesna. Co-sputtering of Lu₂O₃, Eu₂

O₃ and Ga₂O₃ for optoelectronics applications. **IOP Conference Series: Materials Science and Engineering**, [S. l.], v. 872, n. 1, p. 012062, 2020. DOI: 10.1088/1757-899X/872/1/012062. Available on: <https://iopscience.iop.org/article/10.1088/1757-899X/872/1/012062>.

MANDAL, Pramod; SINGH, Udai P.; ROY, Sudesna. A Review on the effects of PVD RF sputtering parameters on rare earth oxide thin films and their applications. **IOP Conference Series: Materials Science and Engineering**, [S. l.], v. 1166, n. 1, p. 012022, 2021. DOI: 10.1088/1757-899X/1166/1/012022. Available on: <https://iopscience.iop.org/article/10.1088/1757-899X/1166/1/012022>.

MEDJDOUB, Farid; INIEWSKI, Krzysztof. **Gallium Nitride (GaN)**. [s.l.] : CRC Press, 2017. DOI: 10.4324/b19387. Available on: <https://www.taylorfrancis.com/books/9781482220049>.

MIN, Ho Soon. Atomic Force Microscopy Characterization of Thin Films: A Review. *In: New Frontiers in Physical Science Research Vol. 5*. [s.l.] : B P International (a part of SCIENCEDOMAIN International), 2022. a. p. 165–177. DOI: 10.9734/bpi/nfpsr/v5/4574E. Available on: <https://stm.bookpi.org/NFPSR-V5/article/view/8971>.

MIN, Ho Soon. Scanning Electron Microscopy Analysis of Thin Films: A Review. *In: Research Aspects in Chemical and Materials Sciences Vol. 5*. [s.l.] : B P International (a part of SCIENCEDOMAIN International), 2022. b. p. 16–28. DOI: 10.9734/bpi/racms/v5/4419E. Available on: <https://stm.bookpi.org/RACMS-V5/article/view/8895>.

MODUTEK. **HOW PIRANHA ETCH IS USED IN SILICON WAFER CLEANING**. 2023. Available on: <https://www.modutek.com/how-piranha-etch-is-used-in-silicon-wafer-cleaning/>.

MORAM, M. A.; VICKERS, M. E. X-ray diffraction of III-nitrides. **Reports on Progress in Physics**, [S. l.], v. 72, n. 3, p. 036502, 2009. DOI: 10.1088/0034-4885/72/3/036502. Available on: <https://iopscience.iop.org/article/10.1088/0034-4885/72/3/036502>.

NGARUIYA, James Mbiyu. **Fundamental processes in growth of reactive DC magnetron sputtered thin films**. 2004. RWTH Aachen University, [S. l.], 2004. Available on: <http://publications.rwth-aachen.de/record/59384/files/59384.pdf>.

NI, Yiqiang et al. The influences of AlN/GaN superlattices buffer on the characteristics

of AlGa_N/Ga_N-on-Si (1 1 1) template. **Superlattices and Microstructures**, [*S. l.*], v. 83, n. 111, p. 811–818, 2015. DOI: 10.1016/j.spmi.2015.03.032. Available on: <http://dx.doi.org/10.1016/j.spmi.2015.03.032>.

NOVIKOV, S. V.; STADDON, C. R.; MARTIN, R. W.; KENT, A. J.; FOXON, C. T. Molecular beam epitaxy of free-standing wurtzite Al Ga_{1–N} layers. **Journal of Crystal Growth**, [*S. l.*], v. 425, p. 125–128, 2015. DOI: 10.1016/j.jcrysgro.2015.02.010. Available on: <https://linkinghub.elsevier.com/retrieve/pii/S0022024815000895>.

OLIVEIRA, R. S. De et al. Structural, Morphological, Vibrational and Optical Properties of GaN Films Grown by Reactive Sputtering: The Effect of RF Power at Low Working Pressure Limit. **Materials Research**, [*S. l.*], v. 25, 2022. DOI: 10.1590/1980-5373-mr-2021-0432. Available on: http://www.scielo.br/scielo.php?script=sci_arttext&pid=S1516-14392022000100240&tlng=en.

OLIVEIRA, R. S. De et al. Identification of Self-Buffer Layer on GaN/glass Films Grown by Reactive Sputtering. **Materials Research**, [*S. l.*], v. 26, 2023. DOI: 10.1590/1980-5373-mr-2023-0005. Available on: http://www.scielo.br/scielo.php?script=sci_arttext&pid=S1516-14392023000100282&tlng=en.

PANDEY, Akhilesh; DALAL, Sandeep; DUTTA, Shankar; DIXIT, Ambesh. Structural characterization of polycrystalline thin films by X-ray diffraction techniques. **Journal of Materials Science: Materials in Electronics**, [*S. l.*], v. 32, n. 2, p. 1341–1368, 2021. DOI: 10.1007/s10854-020-04998-w. Available on: <http://link.springer.com/10.1007/s10854-020-04998-w>.

PANDEY, Akhilesh; KAUSHIK, Janesh; DUTTA, Shankar; KAPOOR, Ashok Kumar; KAUR, Davinder. Electrical and structural characteristics of sputtered c-oriented AlN thin films on Si (100) and Si (110) substrates. **Thin Solid Films**, [*S. l.*], v. 666, p. 143–149, 2018. DOI: 10.1016/j.tsf.2018.09.016. Available on: <https://linkinghub.elsevier.com/retrieve/pii/S0040609018306072>.

PANTHA, B. N.; LIN, J. Y.; JIANG, H. X. High-Quality Al-Rich AlGa_N Alloys. *In*: [s.l.: s.n.]. p. 29–81. DOI: 10.1007/978-3-642-23521-4_2. Available on: http://link.springer.com/10.1007/978-3-642-23521-4_2.

PRABASWARA, Aditya; BIRCH, Jens; JUNAID, Muhammad; SERBAN, Elena

Alexandra; HULTMAN, Lars; HSIAO, Ching-Lien. Review of GaN Thin Film and Nanorod Growth Using Magnetron Sputter Epitaxy. **Applied Sciences**, [S. l.], v. 10, n. 9, p. 3050, 2020. DOI: 10.3390/app10093050. Available on: <https://www.mdpi.com/2076-3417/10/9/3050>.

RAMADAN, A. A.; ABD EL-MONGY, A. A.; EL-SHABINY, A. M.; MATER, A. T.; MOSTAFA, S. H.; EL-SHEHEEDY, E. A.; HASHEM, H. M. Addressing difficulties in using XRD intensity for structural study of thin films. **Crystal Research and Technology**, [S. l.], v. 44, n. 1, p. 111–116, 2009. DOI: 10.1002/crat.200800201. Available on: <https://onlinelibrary.wiley.com/doi/10.1002/crat.200800201>.

RODRÍGUEZ-MADRID, J. G.; IRIARTE, G. F.; ARAUJO, D.; VILLAR, M. P.; WILLIAMS, O. A.; MÜLLER-SEBERT, W.; CALLE, F. Optimization of AlN thin layers on diamond substrates for high frequency SAW resonators. **Materials Letters**, [S. l.], v. 66, n. 1, p. 339–342, 2012. DOI: 10.1016/j.matlet.2011.09.003. Available on: <http://dx.doi.org/10.1016/j.matlet.2011.09.003>.

ROSSNAGEL, S. M. Sputter deposition for semiconductor manufacturing. **IBM Journal of Research and Development**, [S. l.], v. 43, n. 1.2, p. 163–179, 1999. DOI: 10.1147/rd.431.0163. Available on: <http://ieeexplore.ieee.org/document/5389264/>.

SAFI, I. Recent aspects concerning DC reactive magnetron sputtering of thin films: a review. **Surface and Coatings Technology**, [S. l.], v. 127, n. 2–3, p. 203–218, 2000. DOI: 10.1016/S0257-8972(00)00566-1. Available on: <https://linkinghub.elsevier.com/retrieve/pii/S0257897200005661>.

SCHIABER, Ziani S.; LEITE, Douglas M. G.; BORTOLETO, José R. R.; LISBOA-FILHO, Paulo N.; DA SILVA, José H. D. Effects of substrate temperature, substrate orientation, and energetic atomic collisions on the structure of GaN films grown by reactive sputtering. **Journal of Applied Physics**, [S. l.], v. 114, n. 18, 2013. DOI: 10.1063/1.4828873.

SCHILLER, S.; BEISTER, G.; SIEBER, W. Reactive high rate D.C. sputtering: Deposition rate, stoichiometry and features of TiO_x and TiN_x films with respect to the target mode. **Thin Solid Films**, [S. l.], v. 111, n. 3, p. 259–268, 1984. DOI: 10.1016/0040-6090(84)90147-0. Available on: <https://linkinghub.elsevier.com/retrieve/pii/0040609084901470>.

SCHMIDT, Hugo Gerald. Safe Piranhas: A Review of Methods and Protocols. **ACS Chemical Health & Safety**, [S. l.], v. 29, n. 1, p. 54–61, 2022. DOI: 10.1021/acs.chas.1c00094.

Available on: <https://pubs.acs.org/doi/10.1021/acs.chas.1c00094>.

SCHUBERT, E. Fred. **Light-Emitting Diodes**. [s.l.] : Cambridge University Press, 2006. DOI: 10.1017/CBO9780511790546. Available on: <https://www.cambridge.org/core/product/identifier/9780511790546/type/book>.

SCHULZ, Heinz; THIEMANN, K. H. Crystal structure refinement of AlN and GaN. **Solid State Communications**, [S. l.], v. 23, n. 11, p. 815–819, 1977. DOI: 10.1016/0038-1098(77)90959-0. Available on: <https://linkinghub.elsevier.com/retrieve/pii/0038109877909590>.

SEON, M.; PROKOFYEVA, T.; HOLTZ, M.; NIKISHIN, S. A.; FALEEV, N. N.; TEMKIN, H. Selective growth of high quality GaN on Si(111) substrates. **Applied Physics Letters**, [S. l.], v. 76, n. 14, p. 1842–1844, 2000. DOI: 10.1063/1.126186. Available on: <http://aip.scitation.org/doi/10.1063/1.126186>.

SHIGEKAWA, Naoteru; NISHIMURA, Kazumi; SUEMITSU, T.; YOKOYAMA, H.; HOHKAWA, K. SAW Filters Composed of Interdigital Schottky and Ohmic Contacts on AlGaIn/GaN Heterostructures. **Electron Device Letters, IEEE**, [S. l.], v. 28, n. 2, p. 90–92, 2007. DOI: 10.1109/LED.2006.889043.

SIGNORE, M. A.; BELLINI, E.; TAURINO, A.; CATALANO, M.; MARTUCCI, M. C.; CRETÌ, P.; VASANELLI, L.; SICILIANO, P.; QUARANTA, F. Structural and morphological evolution of aluminum nitride thin films: Influence of additional energy to the sputtering process. **Journal of Physics and Chemistry of Solids**, [S. l.], v. 74, n. 10, p. 1444–1451, 2013. DOI: 10.1016/j.jpcs.2013.05.003. Available on: <http://dx.doi.org/10.1016/j.jpcs.2013.05.003>.

SON, Seung-Ik; SHIN, Donghyeok; SON, Young Guk; SON, Chang Sik; KIM, Dong Ryeol; PARK, Joo Hyung; KIM, Seohan; HWANG, Donghyun; SONG, Pungkeun. Effect of working pressure on the properties of RF sputtered SnS thin films and photovoltaic performance of SnS-based solar cells. **Journal of Alloys and Compounds**, [S. l.], v. 831, p. 154626, 2020. DOI: 10.1016/j.jallcom.2020.154626. Available on: <https://linkinghub.elsevier.com/retrieve/pii/S0925838820309890>.

SPROUL, W. D.; CHRISTIE, D. J.; CARTER, D. C. Control of reactive sputtering processes. **Thin Solid Films**, [S. l.], v. 491, n. 1–2, p. 1–17, 2005. DOI: 10.1016/j.tsf.2005.05.022. Available on:

<https://linkinghub.elsevier.com/retrieve/pii/S0040609005005389>.

STRIJCKMANS, K.; SCHELFHOUT, R.; DEPLA, D. Tutorial: Hysteresis during the reactive magnetron sputtering process. **Journal of Applied Physics**, [*S. l.*], v. 124, n. 24, 2018. DOI: 10.1063/1.5042084. Available on: <https://pubs.aip.org/jap/article/124/24/241101/975743/Tutorial-Hysteresis-during-the-reactive-magnetron>.

SUN, M. S.; ZHANG, J. C.; HUANG, J.; WANG, J. F.; XU, K. AlN thin film grown on different substrates by hydride vapor phase epitaxy. **Journal of Crystal Growth**, [*S. l.*], v. 436, p. 62–67, 2016. DOI: 10.1016/j.jcrysgro.2015.11.040. Available on: <https://linkinghub.elsevier.com/retrieve/pii/S0022024815007083>.

TAKEUCHI, Hiroto; OHTSUKA, Makoto; FUKUYAMA, Hiroyuki. Effect of sputtering power on surface characteristics and crystal quality of AlN films deposited by pulsed DC reactive sputtering. **physica status solidi (b)**, [*S. l.*], v. 252, n. 5, p. 1163–1171, 2015. DOI: 10.1002/pssb.201451599. Available on: <https://onlinelibrary.wiley.com/doi/10.1002/pssb.201451599>.

TAKEUCHI, Tetsuya; TAKEUCHI, Hideo; SOTA, Shigetoshi; SAKAI, Hiromitsu; AMANO, Hiroshi; AKASAKI, Isamu. Optical Properties of Strained AlGaIn and GaInN on GaN. **Japanese Journal of Applied Physics**, [*S. l.*], v. 36, n. Part 2, No. 2B, p. L177–L179, 1997. DOI: 10.1143/JJAP.36.L177. Available on: <https://iopscience.iop.org/article/10.1143/JJAP.36.L177>.

TIAN, Xing-Hua; ZHANG, Jian-Min; WEI, Xiu-Mei; HUANG, Yu-Hong. Effects of intrinsic point defects on the structural, electronic, magnetic, and optical properties of marcasite FeS₂. **Solid State Communications**, [*S. l.*], v. 307, p. 113808, 2020. DOI: 10.1016/j.ssc.2019.113808. Available on: <https://linkinghub.elsevier.com/retrieve/pii/S0038109819309305>.

TIGLI, O.; ZAGHLOUL, M. E. Surface acoustic wave (SAW) biosensors. *In*: 2010 53RD IEEE INTERNATIONAL MIDWEST SYMPOSIUM ON CIRCUITS AND SYSTEMS 2010, **Anais [...]**. [s.l: s.n.] p. 77–80. DOI: 10.1109/MWSCAS.2010.5548565.

TISCH, U.; MEYLER, B.; KATZ, O.; FINKMAN, E.; SALZMAN, J. Dependence of the refractive index of Al_xGa_{1-x}N on temperature and composition at elevated temperatures. **Journal of Applied Physics**, [*S. l.*], v. 89, n. 5, p. 2676–2685, 2001. DOI: 10.1063/1.1341212.

UDABE, Ander; BARAIA-ETXABURU, Igor; DIEZ, David Garrido. Gallium Nitride Power Devices: A State of the Art Review. **IEEE Access**, [S. l.], v. 11, p. 48628–48650, 2023. DOI: 10.1109/ACCESS.2023.3277200. Available on: <https://ieeexplore.ieee.org/document/10128694/>.

VAN DER DRIFT, A. No TitleEVOLUTIONARY SELECTION, A PRINCIPLE GOVERNING GROWTH ORIENTATION IN VAPOUR-DEPOSITED LAYERS. **Philips research reports**, [S. l.], v. 22, p. 267–288, 1967.

WANG, Cheng-Liang; GONG, Jyh-Rong; LIAO, Wei-Tsai; WANG, Wei-Lin; LIN, Tai-Yuan; LIN, Chung-Kwei. On the characteristics of AlGaN films grown on (111) and (001) Si substrates. **Solid State Communications**, [S. l.], v. 137, n. 1–2, p. 63–66, 2006. DOI: 10.1016/j.ssc.2005.10.008. Available on: <https://linkinghub.elsevier.com/retrieve/pii/S0038109805008525>.

WANG, Shuchang; ZHANG, Xiong; DAI, Qian; FENG, Zhe Chuan; CUI, Yiping. An X-ray diffraction and Raman spectroscopy investigation of AlGaN epi-layers with high Al composition. **Optik**, [S. l.], v. 131, p. 201–206, 2017. DOI: 10.1016/j.ijleo.2016.11.079. Available on: <https://linkinghub.elsevier.com/retrieve/pii/S003040261631405X>.

WU, Nengtao; XING, Zhiheng; LI, Shanjie; LUO, Ling; ZENG, Fanyi; LI, Guoqiang. GaN-based power high-electron-mobility transistors on Si substrates: from materials to devices. **Semiconductor Science and Technology**, [S. l.], v. 38, n. 6, p. 063002, 2023. DOI: 10.1088/1361-6641/acca9d. Available on: <https://iopscience.iop.org/article/10.1088/1361-6641/acca9d>.

XU, Jian-Kai; JIANG, Li-Juan; WANG, Qian; WANG, Quan; XIAO, Hong-Ling; FENG, Chun; LI, Wei; WANG, Xiao-Liang. Effect of nitrogen gas flow and growth temperature on extension of GaN layer on Si*. **Chinese Physics B**, [S. l.], v. 30, n. 11, p. 118101, 2021. DOI: 10.1088/1674-1056/abff30. Available on: <https://iopscience.iop.org/article/10.1088/1674-1056/abff30>.

XU, Zongwei; HE, Zhongdu; SONG, Ying; FU, Xiu; ROMMEL, Mathias; LUO, Xichun; HARTMAIER, Alexander; ZHANG, Junjie; FANG, Fengzhou. Topic Review: Application of Raman Spectroscopy Characterization in Micro/Nano-Machining. **Micromachines**, [S. l.], v. 9, n. 7, p. 361, 2018. DOI: 10.3390/mi9070361. Available on: <http://www.mdpi.com/2072-666X/9/7/361>.

YANG, Weijia; WANG, Wenliang; LIU, Zuolian; LI, Guoqiang. Effect of AlN buffer layer thickness on the properties of GaN films grown by pulsed laser deposition. **Materials Science in Semiconductor Processing**, [S. l.], v. 39, p. 499–505, 2015. DOI: 10.1016/j.mssp.2015.05.046. Available on: <https://linkinghub.elsevier.com/retrieve/pii/S1369800115003741>.

YUN, Feng; RESHCHIKOV, Michael A.; HE, Lei; KING, Thomas; MORKOÇ, Hadis; NOVAK, Steve W.; WEI, Luncun. Energy band bowing parameter in Al_xGa_{1-x}N alloys. **Journal of Applied Physics**, [S. l.], v. 92, n. 8, p. 4837–4839, 2002. DOI: 10.1063/1.1508420.

ZHANG, J. X.; CHENG, H.; CHEN, Y. Z.; UDDIN, A.; YUAN, Shu; GENG, S. J.; ZHANG, S. Growth of AlN films on Si (100) and Si (111) substrates by reactive magnetron sputtering. **Surface and Coatings Technology**, [S. l.], v. 198, n. 1–3, p. 68–73, 2005. DOI: 10.1016/j.surfcoat.2004.10.075. Available on: <https://linkinghub.elsevier.com/retrieve/pii/S0257897204010795>.

ZHAO, Chao et al. III-nitride nanowires on unconventional substrates: From materials to optoelectronic device applications. **Progress in Quantum Electronics**, [S. l.], v. 61, p. 1–31, 2018. DOI: 10.1016/j.pquantelec.2018.07.001. Available on: <https://linkinghub.elsevier.com/retrieve/pii/S0079672718300302>.

APPENDIX A – XRD OF THE GAN/ALGAN HETEROSTRUCTURES ON GLASS SUBSTRATES

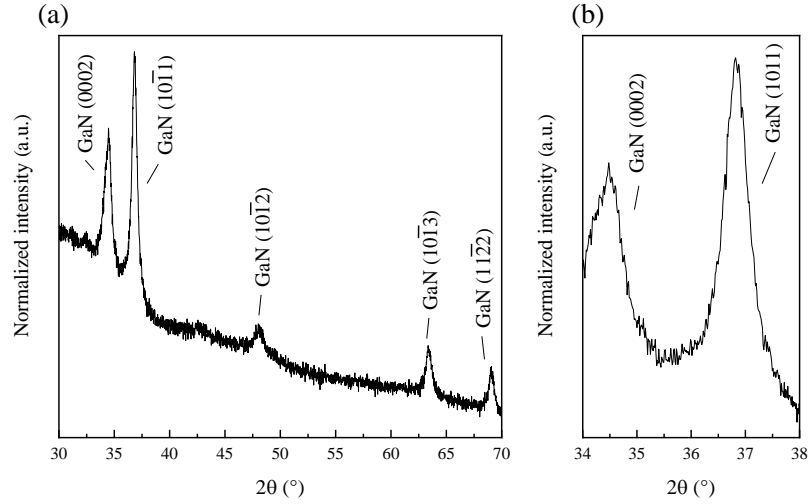


Figure 65: (a) X-Ray diffractogram of the GaN/Si(100) film without buffer layer and (b) zoom-in on the (0002) peak region

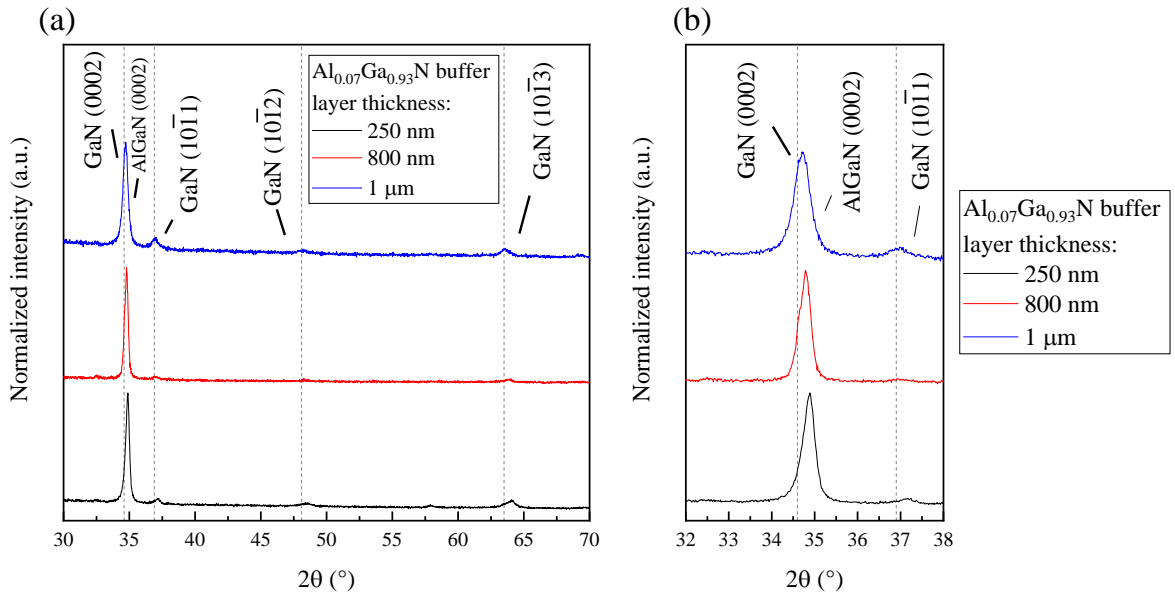


Figure 66: (a) Diffractogram of different buffer layer thicknesses of three GaN/Al_{0.07}Ga_{0.93}N heterostructures and (b) zoom in on the region with the (0002) peak

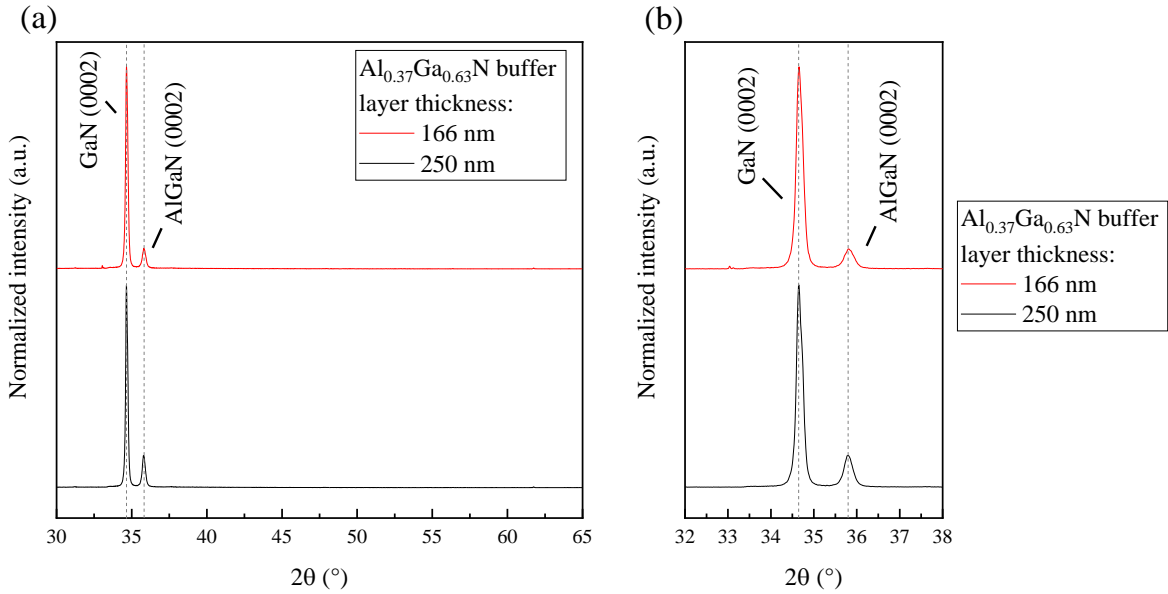


Figure 67: (a) Diffractogram of different buffer layer thicknesses of three GaN/Al_{0.37}Ga_{0.63}N heterostructures and (b) zoom in on the region with the (0002) peak.

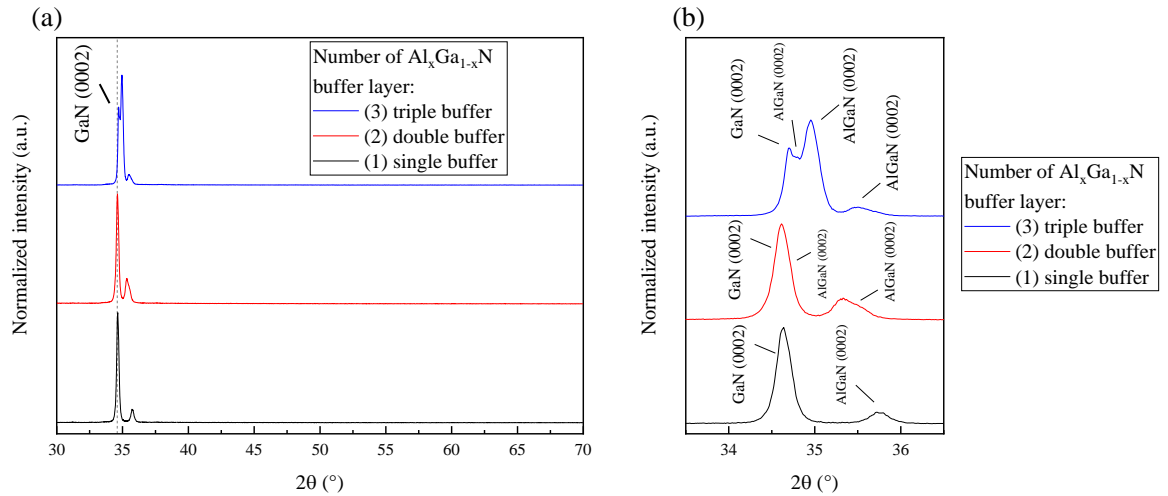


Figure 68: (a) Diffractogram of different buffer layer number of three heterostructures and (b) zoom in on the region with the (0002) peak.

**APPENDIX B – UV-VIS TRANSMITTANCE SPECTRA OF THE GAN/ALGAN
HETEROSTRUCTURES**

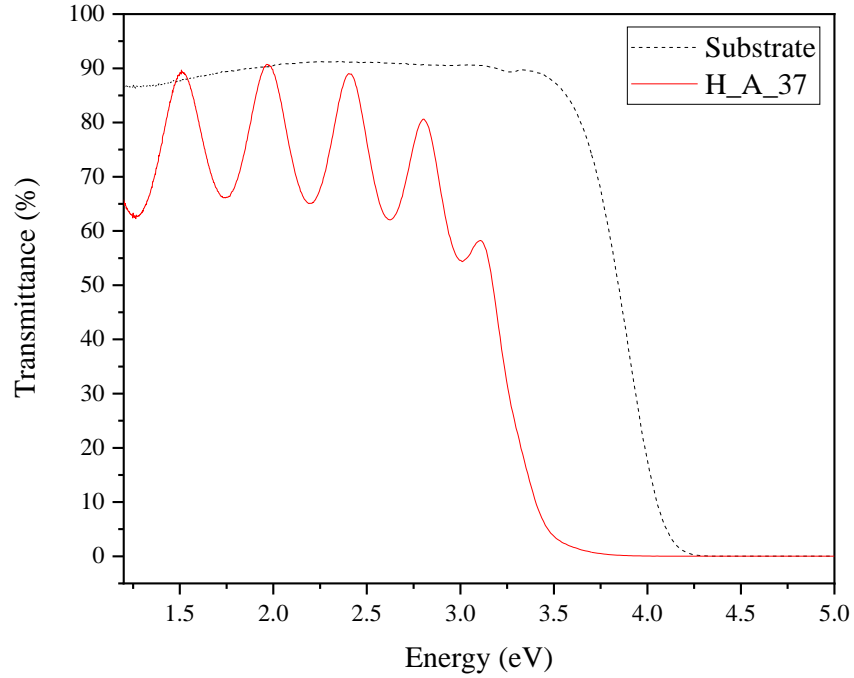


Figure 69: Transmittance spectrum of the GaN/Al_{0.07}Ga_{0.93}N heterostructure with a 250 nm AlGa_N buffer layer thickness (sample H_A_37).

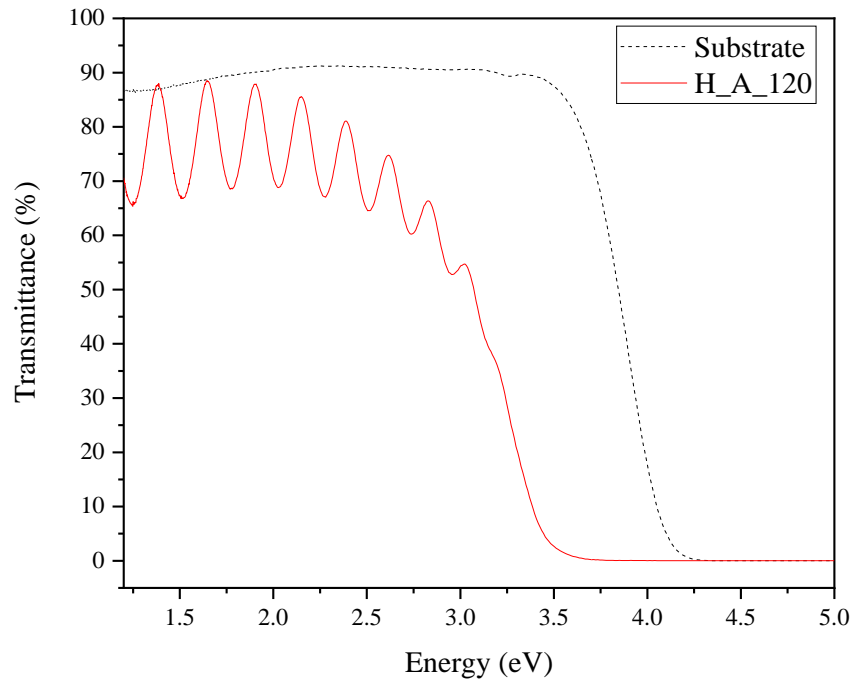


Figure 70: Transmittance spectrum of the GaN/Al_{0.07}Ga_{0.93}N heterostructure with an 800 nm AlGaN buffer layer thickness (sample H_A_120).

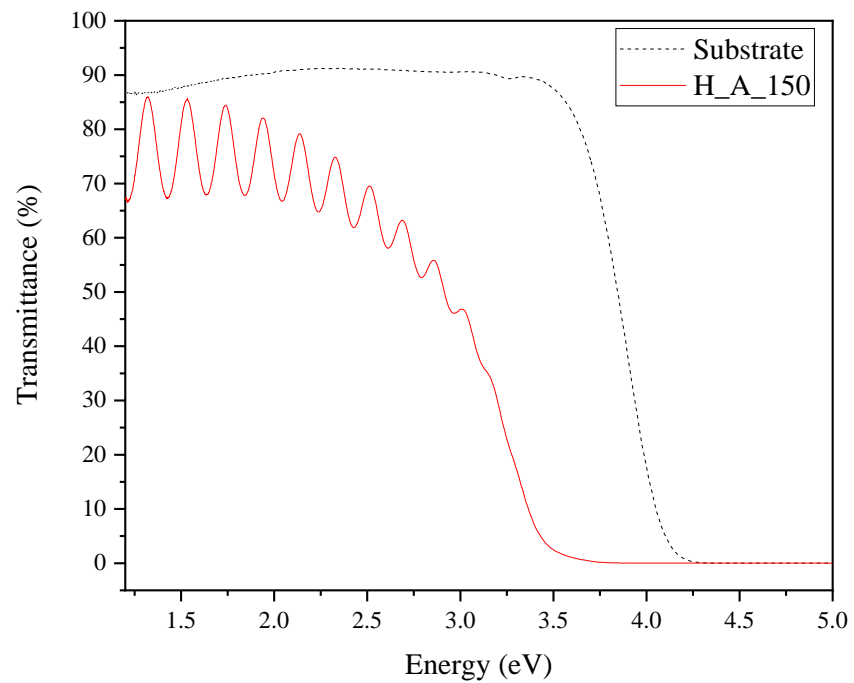


Figure 71: Transmittance spectrum of the GaN/Al_{0.07}Ga_{0.93}N heterostructure with a 1 μ m AlGaN buffer layer thickness (sample H_A_150).

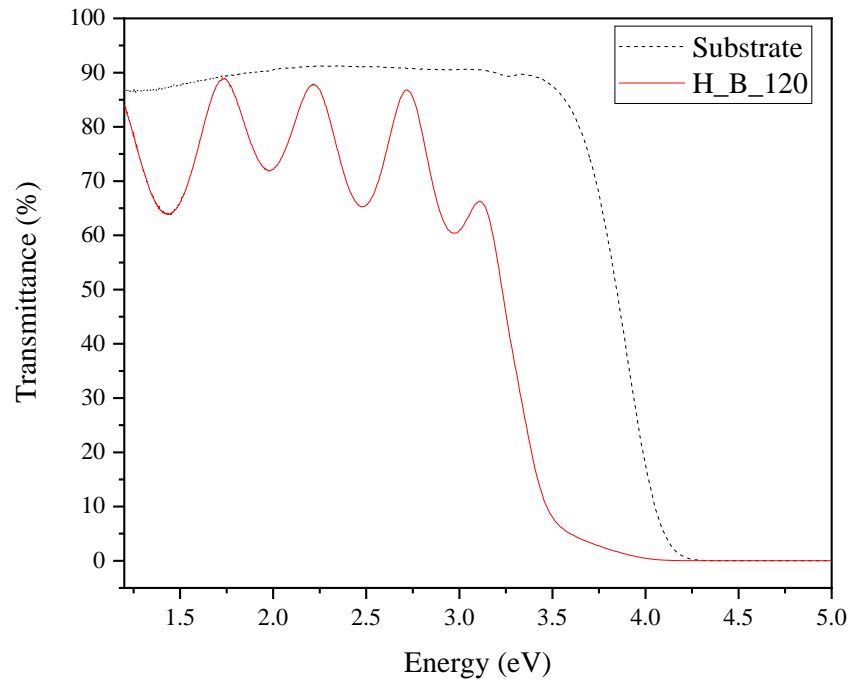


Figure 72: Transmittance spectrum of the GaN/Al_{0.37}Ga_{0.63}N heterostructure with a 166 nm AlGaN buffer layer thickness (sample H_B_120).

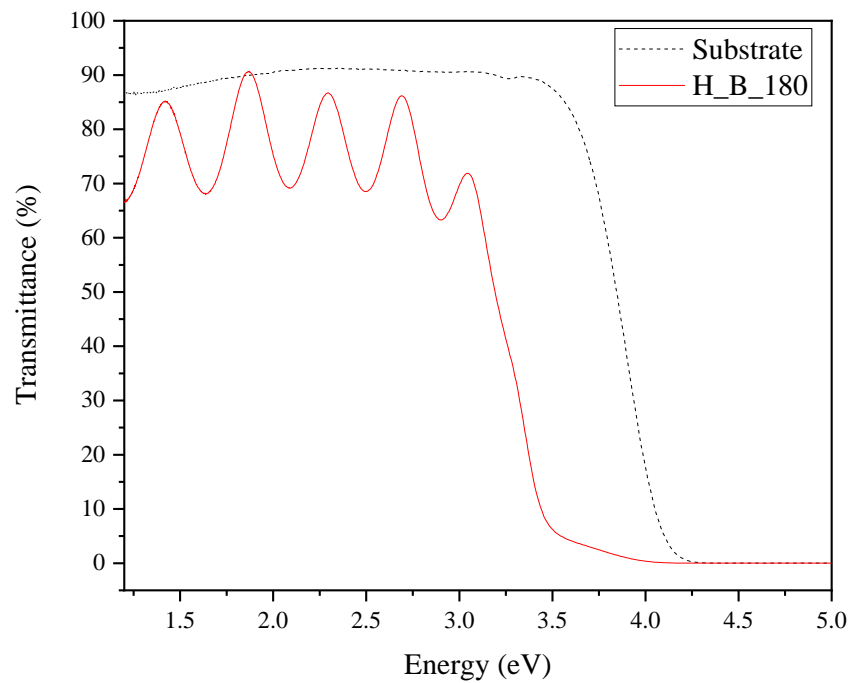


Figure 73: Transmittance spectrum of the GaN/Al_{0.37}Ga_{0.63}N heterostructure with a 250 nm AlGaN buffer layer thickness (sample H_B_180).

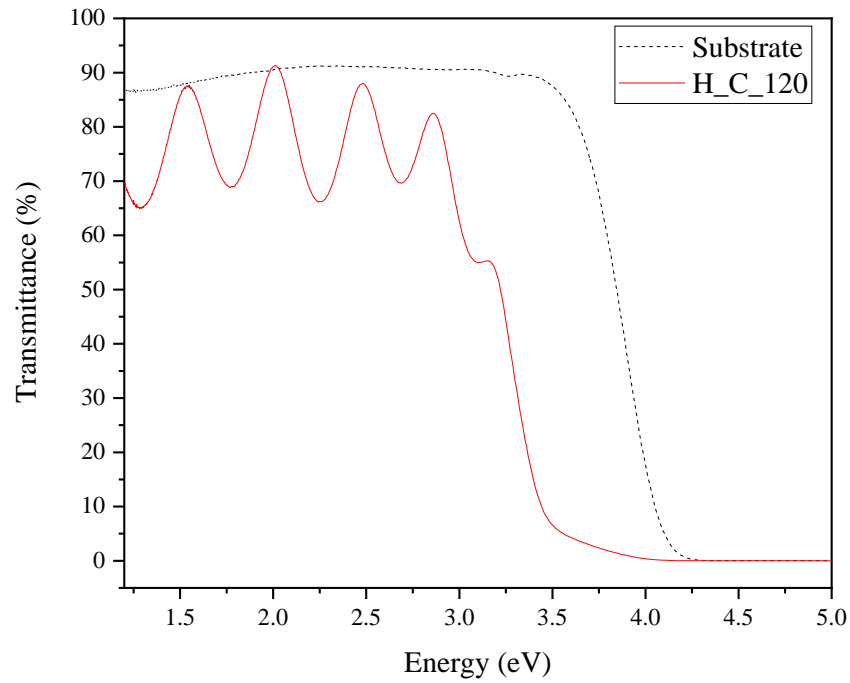


Figure 74: Transmittance spectrum of the GaN/Al_{0.24}Ga_{0.76}N/Al_{0.37}Ga_{0.63}N heterostructure (sample H_C_120).

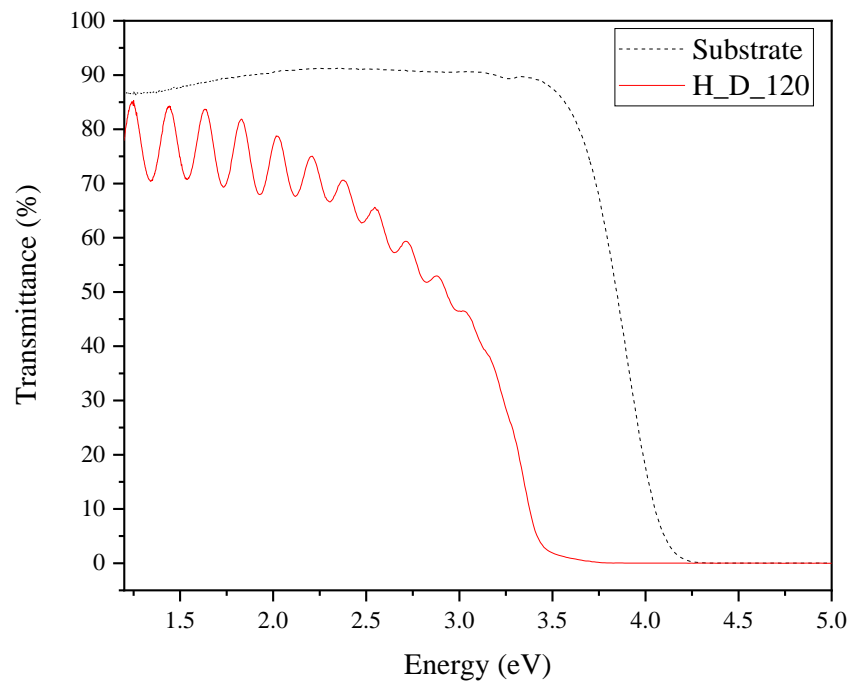


Figure 75: Transmittance spectrum of the GaN/Al_{0.07}Ga_{0.93}N/Al_{0.24}Ga_{0.76}N/Al_{0.37}Ga_{0.63}N heterostructure (sample H_D_120).

**APPENDIX C – FEG-SEM IMAGES SHOWCASING THE SURFACE OF THE
GAN/ALGAN HETEROSTRUCTURES**

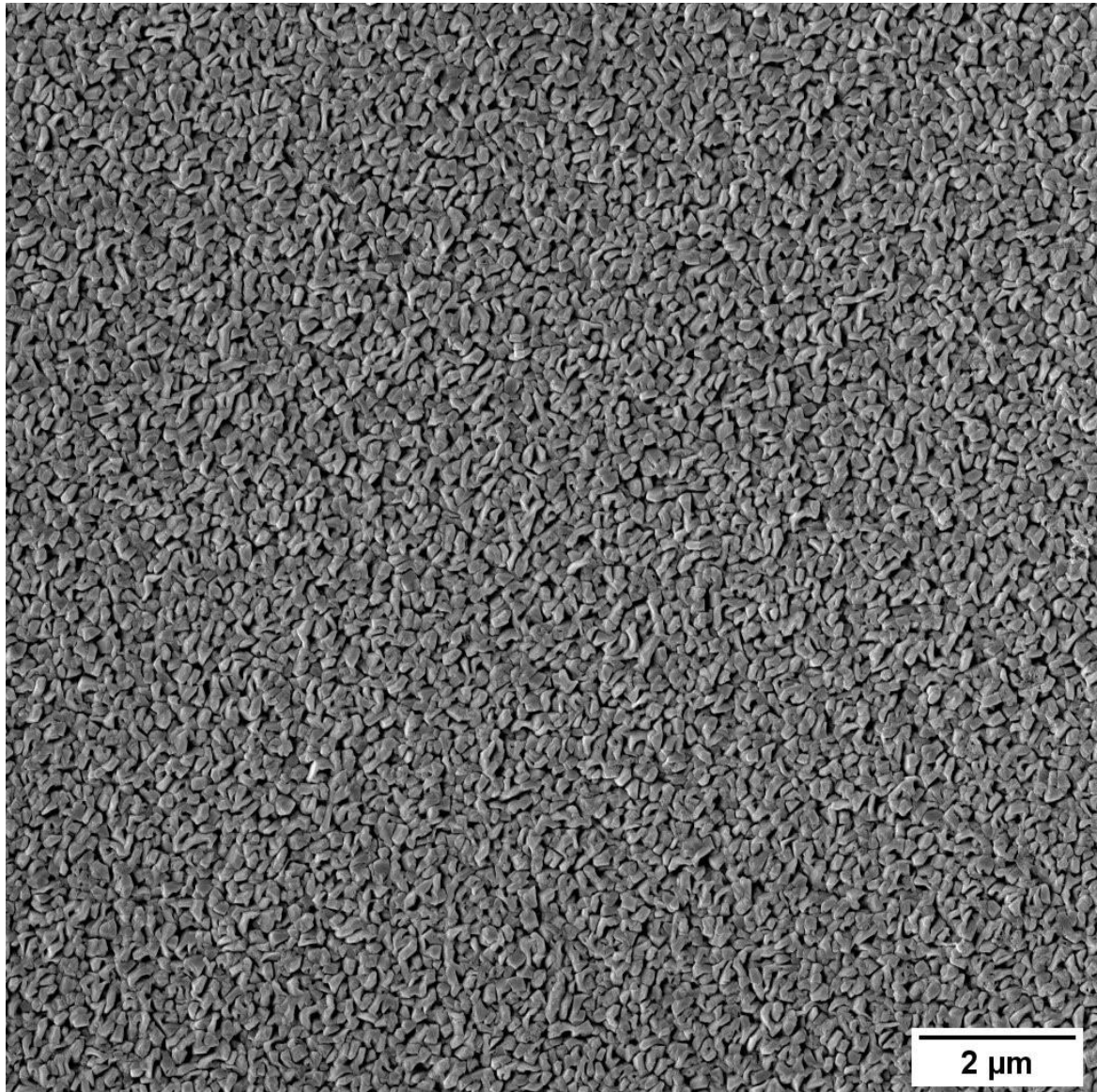


Figure 76: Surface of the GaN/Al_{0.07}Ga_{0.93}N heterostructure with a 1 μm AlGaN buffer layer thickness (sample H_A_150).err

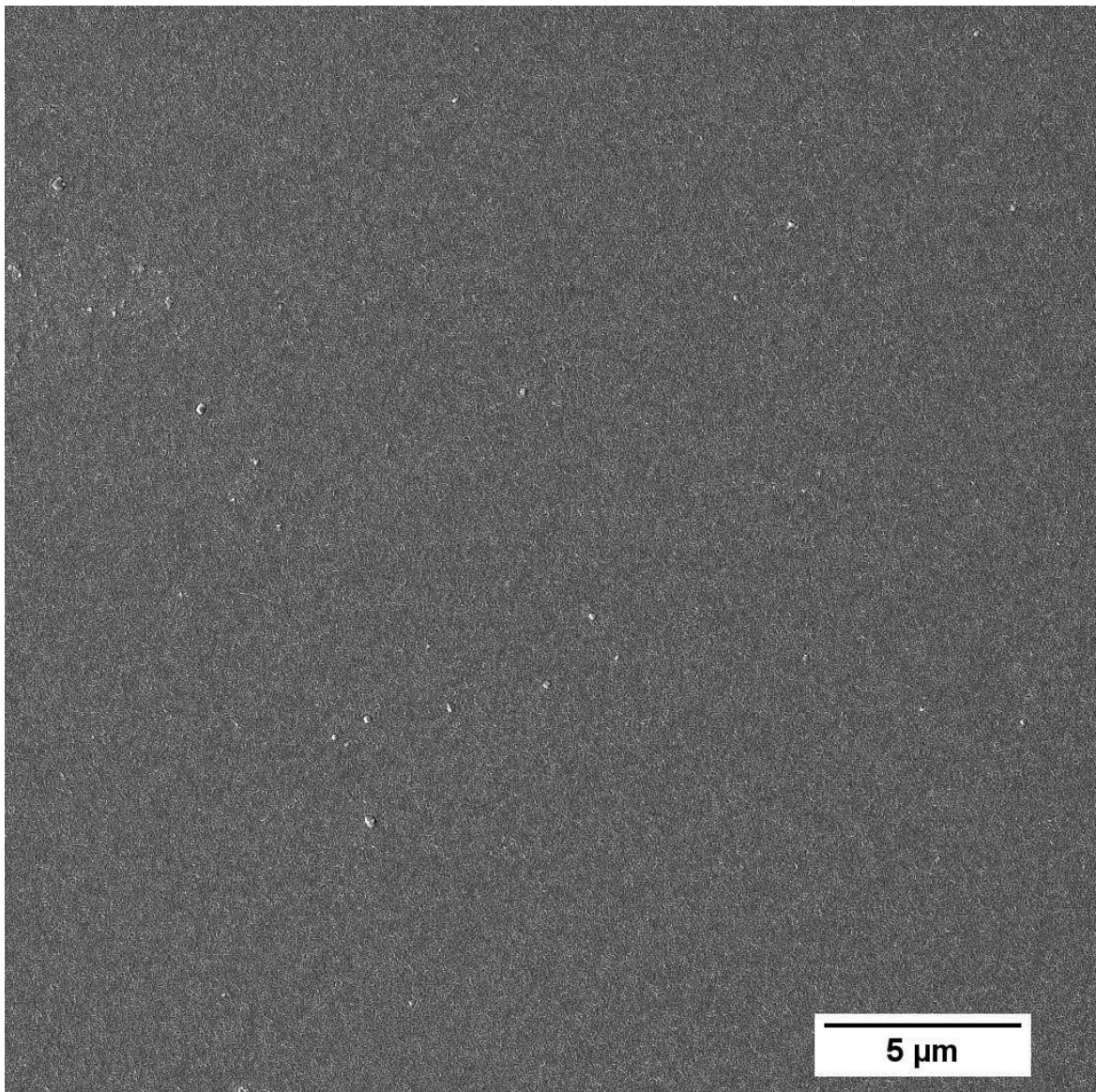


Figure 77: Surface of the GaN/Al_{0.37}Ga_{0.63}N heterostructure with a 166 nm AlGaIn buffer layer thickness (sample H_B_120).

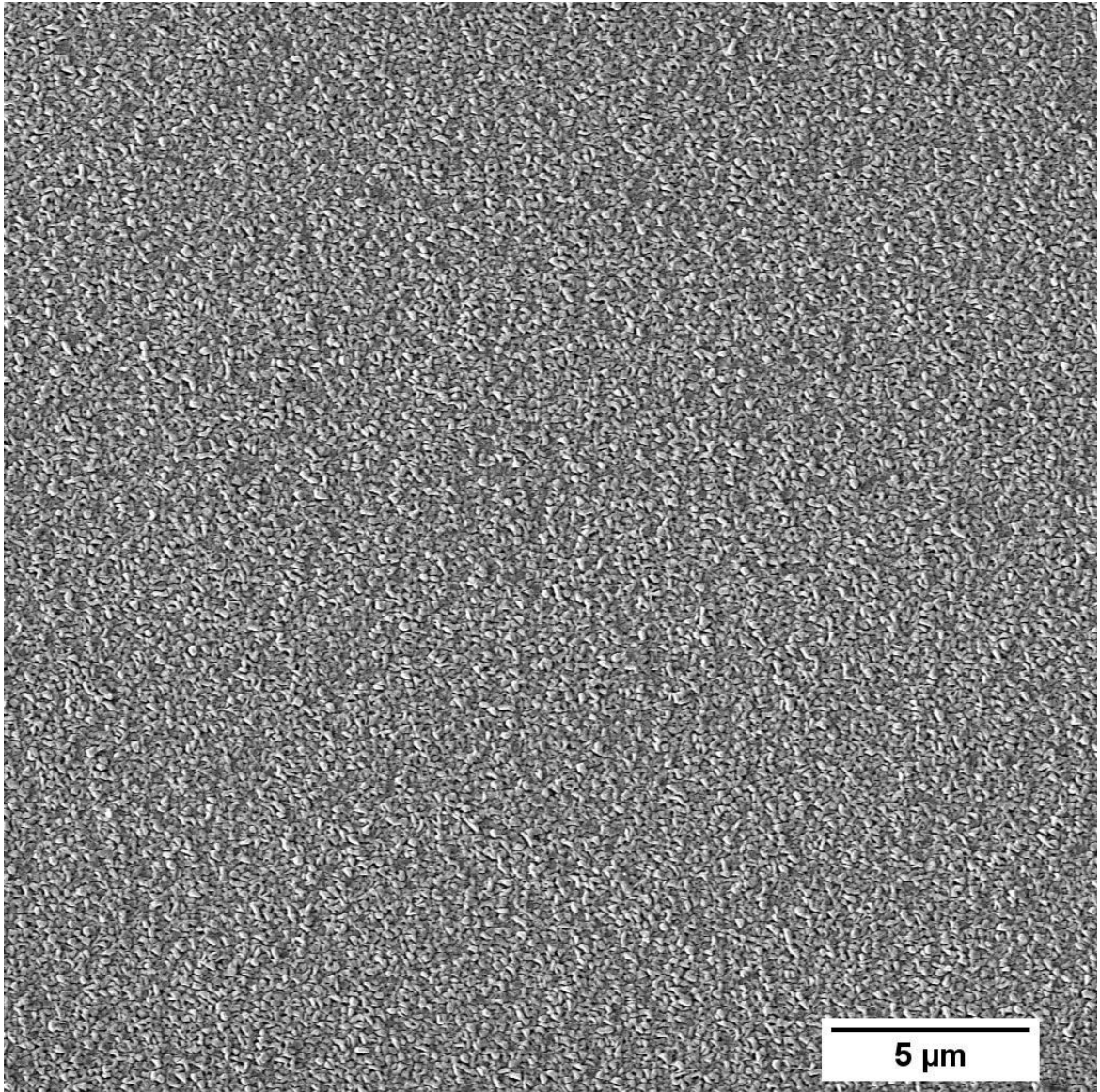


Figure 78: Surface of the GaN/Al_{0.07}Ga_{0.93}N heterostructure with an 800 nm AlGaIn buffer layer thickness (sample H_A_120).

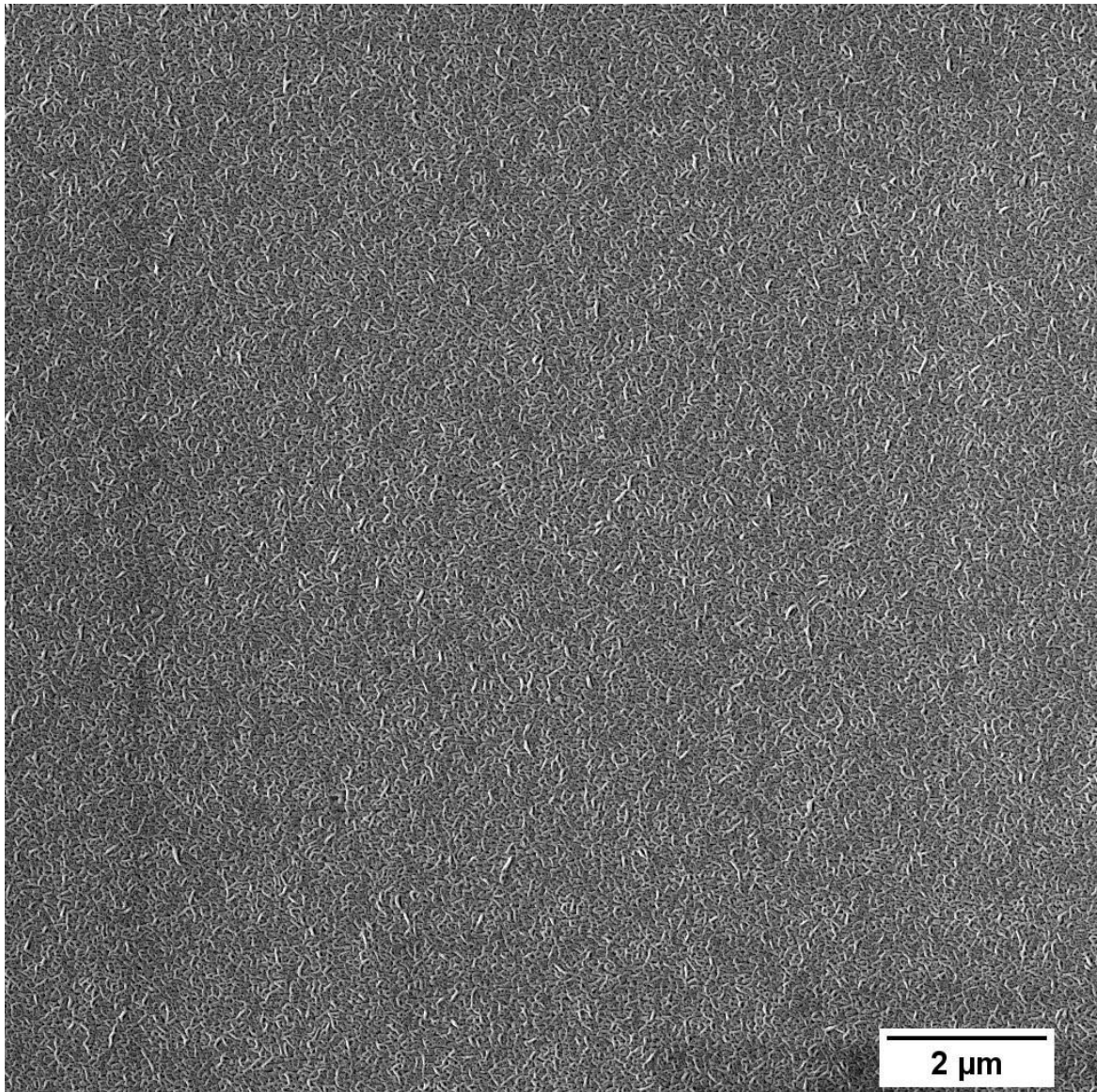


Figure 79: Surface of the GaN/Al_{0.24}Ga_{0.76}N/Al_{0.37}Ga_{0.63}N heterostructure with a total of 280 nm AlGaIn buffer layer thickness (sample H_C_120).

FOLHA DE REGISTRO DO DOCUMENTO

1. CLASSIFICAÇÃO/TIPO <p style="text-align: center;">TD</p>	2. DATA 23 de novembro de 2023	3. REGISTRO N° DCTA/ITA/TD-057/2023	4. N° DE PÁGINAS 157
5. TÍTULO E SUBTÍTULO: Deposition and characterization of thin films and heterostructures of GaN and Al _x Ga _{1-x} N using reactive magnetron sputtering deposition.			
6. AUTOR(ES): Isabela Machado Horta			
7. INSTITUIÇÃO(ÕES)/ÓRGÃO(S) INTERNO(S)/DIVISÃO(ÕES): Instituto Tecnológico de Aeronáutica – ITA			
8. PALAVRAS-CHAVE SUGERIDAS PELO AUTOR: 1. Thin Film. 2. Reactive Magnetron Sputtering. 3. Semicondutor.			
9. PALAVRAS-CHAVE RESULTANTES DE INDEXAÇÃO: Filmes finos; Magnetrons; Semicondutores; Pulverização catódica; Espectros Raman; Difração de raios x; Espectrofotometria; Física de plasmas; Física.			
10. APRESENTAÇÃO: <input checked="" type="checkbox"/> Nacional <input type="checkbox"/> Internacional ITA, São José dos Campos. Curso de Doutorado. Programa de Pós-Graduação em Engenharia Aeronáutica e Mecânica. Área de Materiais, Manufatura e Automação. Orientador: Prof. Dr. Douglas Marcel Gonçalves Leite; coorientador: Prof. Dr. André Luis de Jesus Pereira. Defesa em 16/10/2023. Publicada em 2023.			
11. RESUMO: This work reports on the deposition and characterization of different Al-content Al _x Ga _{1-x} N thin films and subsequent GaN/Al _x Ga _{1-x} N heterostructures using reactive magnetron sputtering deposition. Since achieving high-quality sputtered GaN still relies on the use of expensive substrates, high temperatures and intricate buffer layers, the use of AlGa _N buffer has shown to enhance the quality of these films in a continuous process. Therefore, the main objective is to study the effect of the composition on the quality of the Al _x Ga _{1-x} N films to determine the most suitable composition for the production of heterostructures using AlGa _N as a buffer layer for GaN, in terms of c-axis orientation and crystalline structure, to make this material suitable for application in SAW devices. The Al _x Ga _{1-x} N films were produced using different applied powers to the Al and Ga targets to vary the composition, with the Al content ranging from $0 \leq x \leq 0.47$. Additionally, different substrates were used for the films, including glass and different Si orientations. The other deposition parameters were fixed for all processes, such as pressure (5 mTorr), temperature (550 °C), argon and nitrogen flow (7 and 14 sccm, respectively), and substrate position (90 mm above the Ga target). From the Al _x Ga _{1-x} N films, a set of different compositions and Al _x Ga _{1-x} N layer numbers were selected to produce the heterostructures on glass and Si(100) substrates. This approach allowed for the creation of highly c-oriented GaN films with minimized strains, defects, and surface roughness. The samples were characterized using energy dispersive spectroscopy, optical profilometry, X-ray diffraction, UV-Vis spectrophotometry, Raman spectroscopy, and scanning electron microscopy. The results showed a strong correlation between the properties of the Al _x Ga _{1-x} N films and the composition, as well as an influence of the thickness of the samples. All samples displayed a wurtzite structure with a c-axis preferred orientation, which is desirable as a buffer layer, and this orientation increased with higher Al content. The quality of the films, in general, was evaluated using a combination of results from the different techniques, demonstrating that the Al content plays different roles in terms of strains, crystalline quality, bandgap, refractive index, and Raman phonon modes. For the heterostructures, the presence of an Al-rich buffer layer led to a more strongly c oriented GaN film, with no clear relation to the number or thickness of the buffer layer. Therefore, a high-Al content thin buffer layer successfully increased the quality of the GaN film. However, the use of multiple buffer layers with a compositional gradient further improved the surface of the GaN films without a clear improvement in the structural properties, but it also significantly increased the deposition time and the complexity of the process.			
12. GRAU DE SIGILO: <input checked="" type="checkbox"/> OSTENSIVO <input type="checkbox"/> RESERVADO <input type="checkbox"/> SECRETO			